TOWARDS A COMPLIANCE-MATCHED BIOPOLYMER TISSUE ENGINEERED VASCULAR GRAFT

by

Ehab Akram Tamimi

B.S. Chemical Engineering, The University of Arizona

M.S. Agriculture and Biosystems Engineering, The University of Arizona

M.S. Biomedical Engineering, The University of Arizona

Submitted to the Graduate Faculty of

Swanson School of Engineering in partial fulfillment

of the requirements for the degree of

Doctor of Philosophy

University of Pittsburgh

2018

UNIVERSITY OF PITTSBURGH

SWANSON SCHOOL OF ENGINEERING

This dissertation was presented

by

Ehab Akram Tamimi

It was defended on

August 29, 2018

and approved by

David Vorp, Ph.D., Associate Dean for Research and Professor
Department of Bioengineering

Julie Phillippi, Ph.D., Assistant Professor in the
Department of Cardiothoracic Surgery

Spandan Maiti, Ph.D., Assistant Professor
Department of Bioengineering

Dissertation Director: Jonathan Vande Geest, Ph.D., Professor
Department of Bioengineering

TOWARDS A COMPLIANCE-MATCHED BIOPOLYMER TISSUE ENGINEERED VASCULAR GRAFT

Ehab Akram Tamimi, Ph.D.

University of Pittsburgh, 2018

Cardiovascular disease (CVD) continues to be the largest cause of death in the United States with the highest percentage of CVD-related deaths attributed to coronary artery disease (CAD). Coronary artery bypass grafts (CABG) used to treat CAD often fail due to compliance mismatch, which can lead to anastomotic intimal hyperplasia and thrombosis. While autologous grafts (i.e. saphenous vein) are considered the golden standard for CABG, they have been shown to have lower patency in smaller diameter vessels (<2 mm) and commonly fail due to poor graft quality, graft unavailability, and graft compliance mismatch with the native vessel. Tissue engineered vascular grafts (TEVGs) offer an alternative for CABG that be designed to be biocompatible, non-thrombogenic, compliance-matched, and produced with good durability and deliverability. Currently, small-diameter synthetic TEVGs have shown poor patency rates due to acute thrombogenicity, anastomotic intimal hyperplasia and compliance mismatch to native tissue. One strategy for improving TEVGs is the inclusion of elastic and compliant biological polymers native to the body. TEVGs fabricated from natural biopolymers may have the potential to be more biocompatible and biodegradable. Additionally, natural biopolymers are generally hydrophilic and may provide better physiological support for cell attachment by providing specific integrin interaction sites, which could enhance cell adhesion and proliferation.

Small-diameter acellular electrospun gelatin/fibrinogen cylindrical TEVGs were fabricated and mechanically characterized. Gelatin/fibrinogen constructs crosslinked with glutaraldehyde were found to compliance match porcine left anterior descending coronary artery. The results of this study demonstrate the feasibility of meeting mechanical specifications expected of native arteries by tuning compliance through manipulation of crosslinking time. I have also developed an experimental/computational approach to fabricate an acellular biomimetic hybrid tissue engineered vascular graft composed of alternating layers of electrospun porcine gelatin/polycaprolactone (PCL) and human tropoelastin/PCL blends with the goal of compliance-matching to rat abdominal aorta, while maintaining specific geometrical constraints. All constructs were mechanically characterized and modeled using a modified Fung-type strain energy equation. I have shown that we can tune the mechanical properties of our hybrid synthetic/protein grafts by varying the ratio of protein to synthetic polymer. Fabricated layered optimized grafts were successfully compliance matched and geometry matching to rat abdominal aorta.

Finally, this dissertation also discusses the results of an ocular biomechanics study where the biomechanical properties of the posterior sclera were determined as a function of racioethnicity. This was done to explain the disparity in glaucoma between racioethnic groups (African descent, European descent and Hispanic ethnicity). The mechanical theory of glaucoma rests on the assumption that mechanical damage forces acting on the optic nerve cause a loss of retinal ganglion cell function. Sequential digital image correlation was used to recreate the scleral geometry and determine surface deformations as a function of intraocular pressure. Statistical analysis revealed differences between the three racioethnic group in tensile and compressive principal strains. This may provide a unique opportunity for the development of novel diagnosis and treatment opportunities.

TABLE OF CONTENTS

LIST OF TABLES

LIST OF FIGURES

PREFACE

I would like to express my deepest gratitude and appreciation for the mentorship, support and patience of my adviser, Dr. Jonathan Vande Geest. Thank you to my committee members. Thank you to my fellow labmates whose continuous support and encouragement has been essential to my success, including Catalina Ardila, Reza Behkam, Kenny Furdella, Hirut G Kollech, Dr. Dominic Kyalo Muli, Jeff Pyne-Brucks, Scott Harrison, Dr. Darren Haskett and Stephen Howerton. I am thankful to my dear beloved parents, Dr. Akrum Tamimi and Hana Tamimi. I would like to acknowledge their lifelong struggle and work to provide all the resources and opportunities for me has been instrumental in forming the foundation that enabled to become who I am today. I love you very much, Mama and Baba. Thank you to my dear and beloved siblings Enas, Abdullah, Tesneem, Abdulrahman and Eman Tamimi. I would also like to thank my uncle Dr. Mohammed Tamimi and his family. Thank you to everybody in my family in Palestine and worldwide who has kept me in their prayers along the way.

Thank you to my supportive friends who have been there for me throughout my time in academia. A special acknowledgement to my friend and brother, Mohammad Abagi, for his love, support and acceptance and to his wonderful wife Vardha Khalil for hosting me and putting up with me during my many visits. I would also like to deeply thank Cameron Hood whose mentorship and guidance has been essential for my spiritual, mental and emotional wellbeing. I would also like to extend my deepest thanks to Taylor Thoenes and Doug Airulla whose brotherhood and guidance has been essential in my day to day. A special thanks to my "summer

mom" Susan McGinley and to pretty Helen Williamson Thoenes whose motherly guidance and compassion has been much appreciated. A special gratitude to Debra Cox-Howard for her kind guidance and counsel in some of my most difficult times. Additional acknowledgements and thanks go to Dr. Goli Bagheri, Ashley Toenjes, Mija Sanders, Rachel Beaty, Hilary Ferencak, Omar Mohammad Hussain, William Schlanger, Maryam Mir, Maryam Maleh, Crystal Pimentel, Dr. Maha Nassar, Dr. Scott Lucas, Shonagh McNally, Alison Coombs and Nour Kweider

Alhamdulilah. I thank God Almighty for everything that I have accomplished and for everything that I am today. I pray that God guide me, forgive me and bless me as I move forward through my life. Ameen. In the name of God, I start. Bismillah.

1.0 CHAPTER 1: INTRODUCTION

Cardiovascular disease (CVD) is the major cause of death in the United States [1]. According to the American Heart Association, as of 2014, 92.1 million American adults (more than 1 in 3) have one or more types of cardiovascular disease CVD, which is also listed as the leading underlying cause for 787,650 of all 2,468,435 deaths in the United States, approximately 1 out of every 3 Americans [1]. The highest percentage of CVD-related deaths were attributed to coronary artery disease. Approximately every 40 seconds, an American will have a myocardial infarction as part of CAD [1]. About 158,000 coronary artery bypass graft (CABG) procedures were performed in 2010 [1]. There is an increasing demand for affordable, biocompatible and more easily accessible coronary vascular grafts. Autologous grafts like the bilateral mammary artery, radial artery and the saphenous vein grafts have been considered to be the golden standard in obtaining total arterial myocardial revascularization [2]. However, autologous grafts like the saphenous grafts have shown to have 10-year patency chances of 55% in smaller diameter vessels (<2 mm) [3]. Autologous graft failure factors include poor graft quality [4], graft unavailability, lack of durability [5], shorter durability due to calcification [5] and graft compliance mismatch to the native vessel [6, 7]. Inherent compliance mismatch between the native vessel and graft has been shown to lead to graft failure via intimal hyperplasia [6, 7].

Tissue-engineered vascular grafts (TEVGs) offer an alternative source for grafts, which may be engineered to be non-thrombogenic, biocompatible, non-immunogenic, resistant to infection, mechanically stable, and compliance-matched to the native vessel with consistent good quality, durability and availability. Synthetic materials like Dacron and PTFE have been clinically used as TEVG materials in peripheral vascular surgery [8] and aortic root or ascending aorta replacement [9]. However, small-diameter synthetic grafts have shown poor patency rates due to acute thrombogenicity and anastomotic intimal hyperplasia [6, 10-12]. Some researchers have attempted to make synthetic TEVGs less thrombogenic by modifying the synthetic material [13, 14] or by adding growth factors intraluminally to encourage endothelialization *in situ* [15]. However, TEVGs created from non-biological synthetic materials tend to be stiffer and have shown compliance mismatch to native arteries [16, 17], which can lead to intimal hyperplasia [18].

Artery walls are comprised of three layers: the intima layer consisting of a monolayer of endothelial cells on an elastic basal lamina (primarily responsible for the anti-thrombogenicity of the vessel), the medial layer primarily composed of vascular smooth muscle cells (SMCs) and an adventitia layer made up of additional matrix and fibroblasts. A diagram illustrating the three layers of an artery is shown in Figure 1.The media layer, which is the main load-bearing layer primarily responsible for the mechanical performance of the vessel, has an extracellular matrix (ECM) largely composed of elastin and type III collagen with proteoglycans [19]. The media layer ECM is the primary determinant of biomechanical properties of the vessel and plays a critical role in biological functions, like their ability to bind multiple interacting partners such as growth factors and cell signal receptors[20]. ECM embedded proteins also provide instructional signals that induce, define and stabilize vascular cell phenotypes [21].

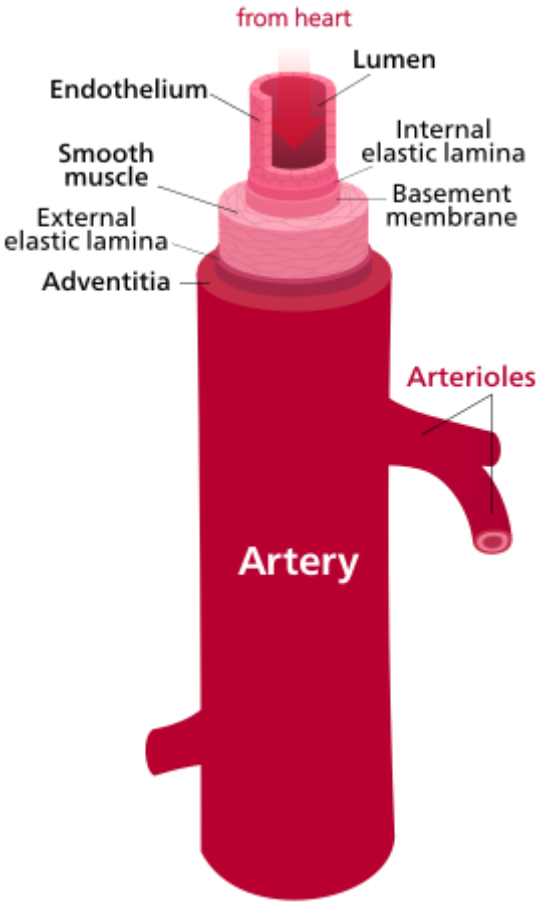

Figure 1. Diagram of an artery illustrating the three layers: intima (lumen), media (smooth muscle) and adventitia [22].

The vascular ECM largely consists of 3D nanofibrous structure made of collagen and other biopolymers. Researchers have attempted to mimic ECM microstructure using fabrication methods like thermally induced phase separation [23-25], and electrospinning [26-28]. Electrospinning is a fabrication method to produce non-woven nanofibers from polymeric solutions. The process is initiated by a high electric potential difference generated between a capillary dispensing a polymeric solution and a collecting target. The solution becomes charged, the electrostatic forces overcome the surface tension at a point known as the Taylor Cone and a

polymerizing jet is formed, which travels towards and deposits on the target [29, 30]. Electrospinning has been a popular method used by researchers to fabricate tubular constructs deposited onto cylindrical targets. The process of electrospinning is an attractive fabrication method, as it allows control over dimensions and alignment of fibers, porosity and overall microstructure of the scaffolds. This is done by modulating different electrospinning parameters including voltage, distance between the dispensing tip and target and volumetric dispensing rate. However, the process also has limitations. Some studies have shown that electrospinning certain natural biopolymer may cause denaturation [31] and instabilities that could result in an accumulation of biopolymer at the dispensing tip. Many electrospinning protocols involve volatile organic solvents, which limit the possibility of microintegration of cells during fabrication due to solvent cytotoxicity. In addition, there have been mild concerns on the repeatability and reproducibility of the fibers fabricated by electrospinning [32-34]. Nonetheless, researchers have used electrospinning to create structures similar to vascular extracellular matrix, which could allow the necessary capacity for cell proliferation and remodeling [35, 36]. It also offers the ability to modulate the mechanical properties of scaffolds by changing different electrospinning parameters [37].

Synthetic polymers have been used by many researchers to fabricate electrospun scaffolds [38-45] like PEUU[43, 44] and polyurethane [45]. Small-diameter synthetic polymer grafts, which introduce an exogenous non-biological material into the body, have been shown to be biocompatible and/or biodegradable in some small animal models [46-51] but may not be suitable for some large animal models [52, 53] and clinical patients [6, 10, 11]**,** due to acute thrombogenicity and anastomotic intimal hyperplasia. While some have attempted to address this issue by reducing the thrombogenetic nature of the synthetic polymer [41, 54], others have

considered non-synthetic biopolymers to fabricate their scaffolds [55-61]. Drawing from the composition of native tissue, one option to create TEVGs is to use biological non-synthetic polymers native to the body. These biopolymers may have the potential to be more biocompatible and biodegradable and to encourage *in situ* cell migration, proliferation and remodeling. Additionally, these biological polymers more closely resemble the microstructure of vasculature [62-66]. There are many studies that have investigated creating grafts by electrospinning biopolymers like collagen [58, 67, 68], collagen/elastin mixtures [69-72], gelatin [73-76], gelatin/fibrinogen mixtures [77-79] and tropoelastin [80-82].

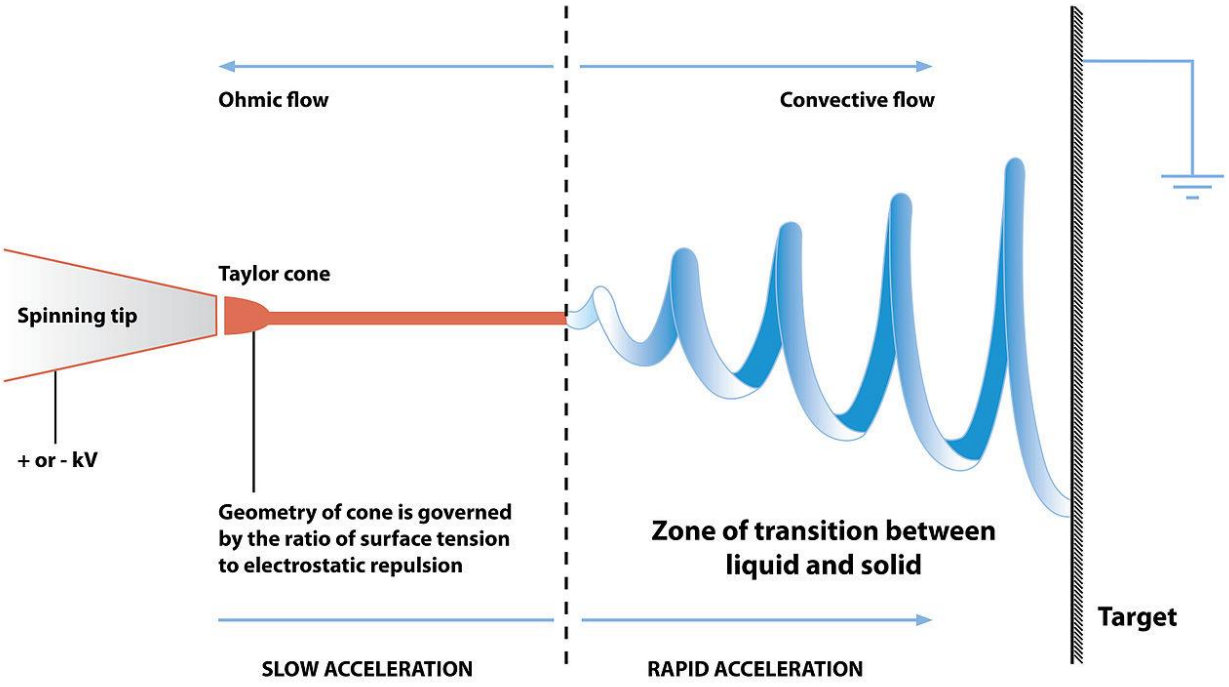

Figure 2. Diagram of the electrospinning process showing the a charged polymeric solution being dispensed and being collected on a grounded target [83].

As mentioned, the medial layer of coronary arteries is primarily composed of an extracellular matrix of collagen and elastin. Some studies have suggested developing electrospun scaffolds composed of collagen, elastin and other synthetic polymers to provide mechanical support, in an effort to match the structural, mechanical and geometric properties of native coronary arteries [72, 84, 85]. However, some researchers have questioned the efficacy of electrospinning collagen, arguing that electrospinning collagen out of solvents may effectively denature this biopolymer, resulting in the production of electrospun gelatin [31]. Gelatin is a structurally similar derivative of collagen acquired by denaturing the triple-helix structure of collagen. Gelatin has been found to be a cost-effective biodegradable biopolymer [86] with more availability of RGD sequence cell binding sites compared to collagen [87]. Additionally, relative to collagen, gelatin has been reported to reduce the potential of an antigenic response *in vivo* [88]. The non-antigenicity of gelatin has been attributed to absence of aromatic groups. Specifically, gelatin is deficient in both tyrosine and tryptophan, and contains only low levels of phenylalanine [88, 89]. Researchers have electrospun gelatin/fibrinogen sheets and successfully cultured human cardiomyocytes with brief mechanical characterization [77]. Along those lines, our research group investigated the feasibility of growing porcine vascular smooth muscle cells (SMCs) on electrospun gelatin/fibrinogen scaffolds [90]. Our results showed that SMCs proliferated and migrated within the scaffold. More specifically, a ratio of 80:20 (gelatin:fibrinogen) was determined to be the ratio that would result in the highest cell number as shown in Figure 3[90]. The study also determined that transforming growth factor beta 2 (TGFβ2) had a significant effect on the proliferation and collagen deposition of the SMCs. Specifically, lower concentration of exogenous TGFβ2 increased cell proliferation and migration with lower SMC collagen deposition. Conversely, increasing the concentration of exogenous TGFβ2 resulted in lower cell mitotic

function and migration, with an increase in collagen deposition. This suggested that one could use the biochemical environment (i.e. growth factors like TGFβ2) to serve as a switch to manipulate the proliferative and remolding behavior of SMCs seeded onto TEVGs [90].

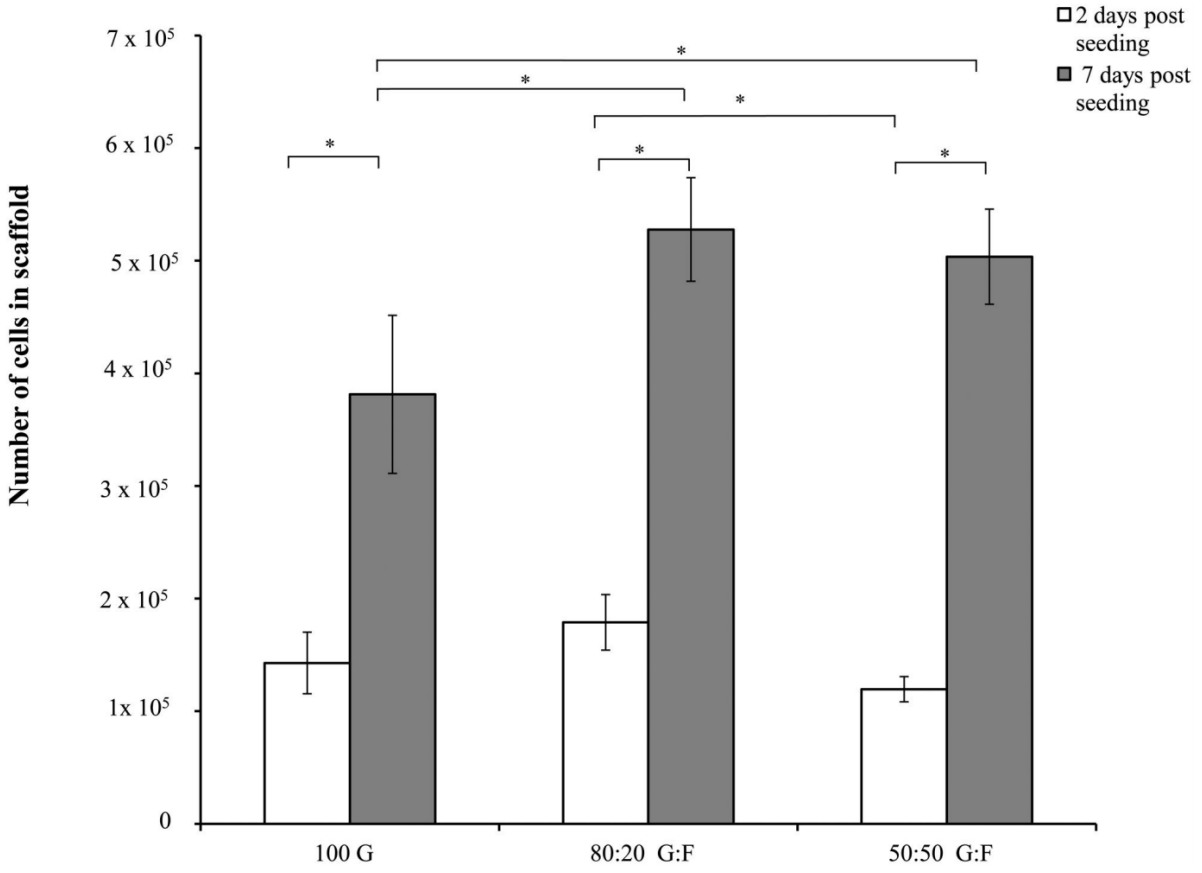

Figure 3. Cell proliferation results after 2 (white) and 7 (gray) days post seeding in 100% gelatin, 80% gelatin 20% fibrinogen, 50% and gelatin 50% fibrinogen scaffolds. Average cell number per scaffold is reported for the two time points. Error bars shown are standard deviation. Asterisk indicates p-value < 0.05, n=6. This study determined that 80:20 gelatin:fibrinogen constructs resulted in the highest cell proliferation [90].

Elastin is a component of elastic fibers, which provides strength and elasticity to vascular tissue. The soluble monomer of elastin is tropoelastin, which is composed of alternating hydrophobic and hydrophilic domain structures crucial for the process of crosslinking and overall

mechanical behavior [91]. Tropoelastin is also a main functional component in wound healing through chemotactic activity [92]. Obtaining the tropoelastin monomer from various tissues has historically been highly inefficient as it requires the perturbation of the fast natural crosslinking process of tropoelastin into elastin [93]. However, the availability of large quantities of highly purified human tropoelastin has only recently become available through recombinant bacterial system expression [94]. Researchers have successfully electrospun tropoelastin fibers [80-82], and some have demonstrated that crosslinked electrospun fibers retain the monomer's conformation, biological activity [95] and low thrombogenicity of elastin [91]. Tropoelastin and elastin have been described as one of the most elastic biosolid materials [91] and preliminary generated by our laboratory group has previously shown that adding tropoelastin to gelatin constructs crosslinked with glutaraldehyde resulted in an increased in elasticity and compliance (Figure 4).

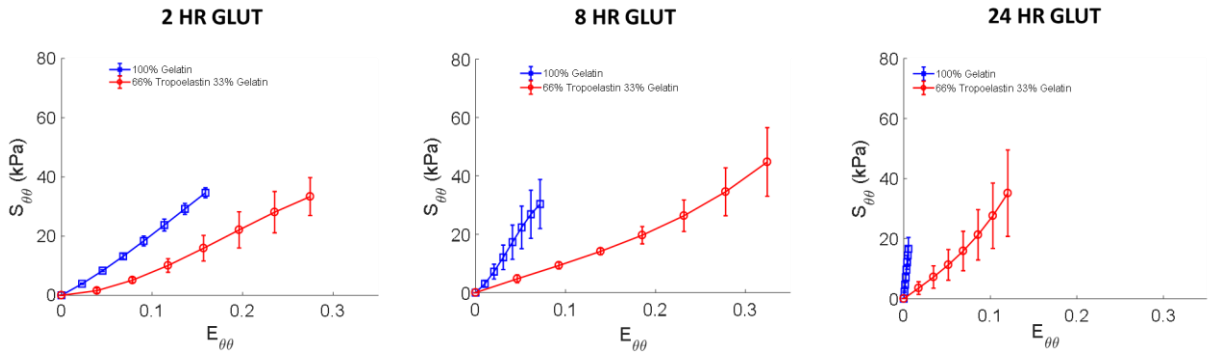

Figure 4. Preliminary results showing circumferential stress-strain graphs comparing constructs fabricated from 100% gelatin and 66% tropoelastin and 33% gelatin at different gluteraldehyde crosslinking times. The graphs show that adding tropoelastin to the composition of the graft decreases the stiffness of the graft.

It should be noted, however, that non-crosslinked electrospun natural polymers do not provide the necessary mechanical integrity for TEVG applications and that these materials are also not stable in aqueous solutions as they can dissolve easily [31, 96]. Some researchers have resorted to using crosslinking agents that strengthen these biopolymers and provide stability while retaining the elastic properties intrinsic to these materials [72, 97-99]. Chemical crosslinking agents like glutaraldehyde have been widely used to crosslink electrospun biopolymers [70, 100]. However, glutaraldehyde-crosslinked biomaterials have been shown to promote cytotoxicity [101]and *in vivo* calcification [102-104]. While one study has investigated different methods of detoxifying glutaraldehyde-crosslinked materials [105], others have searched for alternative crosslinking agents. One such agent is genipin, a natural crosslinking agent that has been used to crosslink different biomaterials [106-109], while exhibiting less cytotoxicity [110] and less calcification *in vivo* [105].

Even with crosslinking, TEVGs composed of crosslinked biopolymers have still shown a lack of mechanical strength necessary to function properly. Studies investigating the mechanical properties of biopolymers have shown that crosslinked natural materials lack the necessary mechanical integrity when compared to native tissue [56, 77, 100]. One solution to overcoming this mechanical limitation of biopolymer TEVGs is to add synthetic polymer to the composition of the construct. For example, some researchers have created hybrid constructs by mixing collagen with different synthetic polymers [111-113]. Polycaprolactone (PCL) is a common biocompatible biodegradable synthetic polymer which has been mixed with collagen [114, 115], elastin[116], collagen\elastin mixtures,[117] gelatin [118] and tropoelastin [119]. These hybrid scaffolds demonstrated additional mechanical strength and stability, while retaining some of the elastic and biochemical properties of the biopolymers that they contain.

There are many factors that may lead to vascular graft failure including biological factors, vascular injury, hemodynamic factors, compliance mismatch and other differences in mechanical properties between graft and native vessel [120]. Many studies have acknowledged the importance of evaluating graft compliance, burst pressure and suture retention in the development of TEVGs [51, 121-125]. Compliance mismatch is one of the major causes of restenosis and graft failure due to perturbations in local hemodynamics [126], which have been shown to be detrimental to graft performance and patency [127]. Therefore, it is crucial that the mechanical properties of the TEVG be comparable to that of native vessels, as a relationship has been found between compliance mismatch and the development of anastomotic intimal hyperplasia[128], possibly due to flow disturbances in and disruption of chemical transport in the fluid at the distal anastomosis [129, 130]. Some researchers have utilized finite element methods to analyze arterial anastomoses to study the effects of graft compliance mismatch [131], while others have used computational fluid dynamics analysis to understand the effect of graft diameter mismatch [130, 132]. Computational methods can be effective tools in determining the appropriate geometry and material properties for compliance matching grafts while saving time and resources.

In this dissertation, I demonstrate work that utilized the process of electrospinning biopolymers (gelatin/fibrinogen) chemically-crosslinked to fabricate TEVGs that can be compliance-matched to native tissue (porcine coronary artery). Additionally, I use an experimental/computational method to determine the geometric and compositional parameters necessary to fabricate a PCL-enforced layered gelatin/tropoelastin crosslinked with genipin. This biomimetic TEVG was successfully compliance matched to that of abdominal rat aorta.

2.0 CHAPTER 2: SPECIFIC AIM 1

Specific Aim 1: *Determine how glutaraldehyde-crosslinking duration modulates the biaxial mechanical properties and compliance of acellular gelatin/fibrinogen TEVGs in an effort to compliance match to porcine LADC and rat abdominal aorta*.

In this aim, I sought to develop an acellular graft whose mechanical properties can be modulated to be compliance matched to native tissue. My hypothesis was that there is a glutaraldehyde crosslinking duration that would yield electrospun gelatin/fibrinogen tubular constructs with mechanical properties similar to native vessels. The rationale behind this hypothesis is that increasing glutaraldehyde-crosslinking duration has been shown to have a stiffening effect on electrospun gelatin/fibrinogen constructs.

As such, in this study I investigated the feasibility of developing an acellular gelatin/fibrinogen TEVG that could compliance-match with porcine left anterior descending coronary (LADC) artery via examination of the effects of crosslinking time, axial load and intraluminal pressure on the mechanical properties and by performing a comprehensive tubular biaxial mechanical analysis of the constructs under normal physiological conditions.

This work was adapted from published work with the following reference [100]:

Tamimi EA, Ardila DC, Haskett DG, et al. *Biomechanical Comparison of Glutaraldehyde-Crosslinked Gelatin Fibrinogen Electrospun Scaffolds to Porcine Coronary Arteries.* ASME. J Biomech Eng. 2015;138(1):011001-011001-12. doi:10.1115/1.4031847.

2.1 MATERIALS

2.1.1 Porcine Coronary Arteries Tissue Acquisition

All porcine tissue acquisition was done according to the approved protocols with the University of Arizona Institutional Animal Care and Use Committee. Our research group has previously collected mechanical data from porcine coronary arteries [133] extracted from hearts (n=5) obtained from the University of Arizona Meat Sciences Laboratory 30 min post mortem. The left anterior descending coronary (LADC) artery was excised from each heart. The extraneous fat, myocardium and most of the adventitia was removed from each LADC. Biaxial stress-strain mechanical data was determined for the proximal, middle and distal sections of the coronary arteries. Datasets also included artery outer diameter and thickness. For this study, the LADC distal section dataset (n=3) was arbitrarily chosen as the dataset to compare to our TEVGs.

2.1.2 Fabricating Electrospun Constructs

A custom-made electrospinning apparatus was used to fabricate the tubular constructs. Gelatin extracted from porcine skin (Sigma-Aldrich, USA) and fraction I bovine fibrinogen (Sigma-Aldrich, USA) was dissolved in 1,1,1,3,3,3-Hexafluoro-2-propanol (HFP) (Sigma-Aldrich, USA) at a 80:20 ratio to create a 10% (w/v) solution. Constructs with this composition have been shown by our group to promote cell adherence and proliferation compared to alternative ratios [90]. In a ventilation hood, the solution was loaded into a 5ml BD syringe with a 23 gauge stainless steel dispensing needle and attached to a NE-100 single syringe pump (New era pump systems Inc., USA). A voltage difference of 15 kV was generated between the dispensing tip and a grounded rotating translating stainless steel mandrel (1.4 mm OD). Preliminary optimization experiments

determined that the effect of both mandrel translation and rotational speeds were minimal on fiber orientation and mechanical properties. Therefore, a low rotational speed of 25 RPM and a low translational speed of 10 mm/sec was selected to minimize uncontrollable rod vibrations and promote electrospinning jet stability. The syringe tip and the rotating translating rod were enclosed in an acrylic housing for additional insulation and control. The internal environment temperature and relative humidity remained constant at about 25 ± 2°C and 38 ± 3%, respectively. The complete electrospinning setup and fabricated non-crosslinked electrospun constructs are shown in Figure 5.

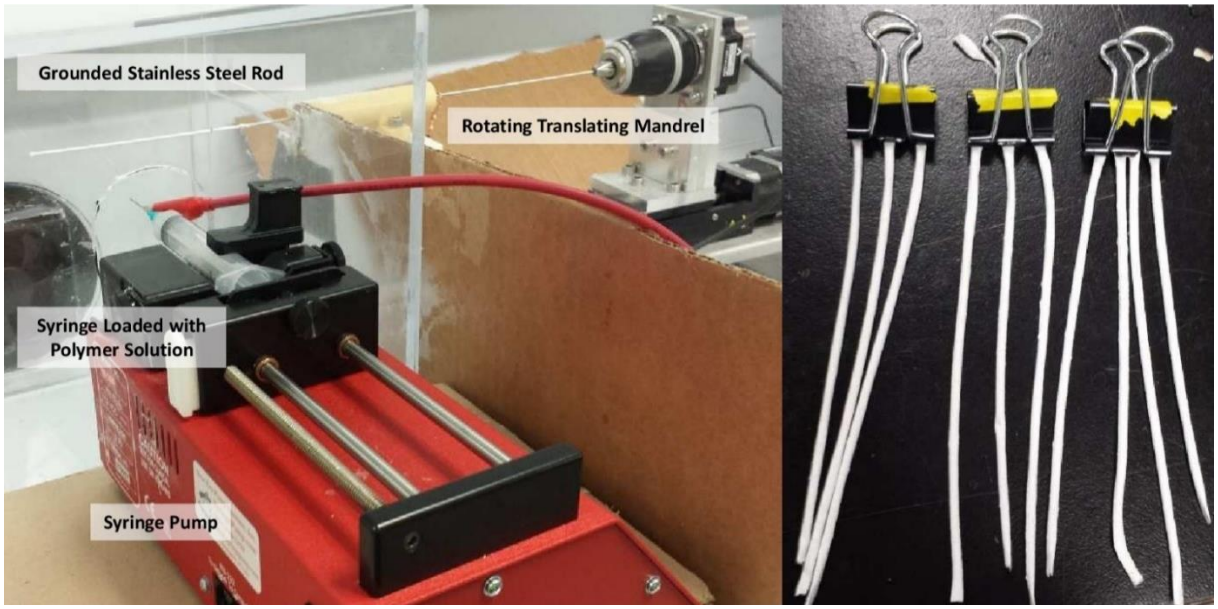

Figure 5. (Left) Electrospinning setup which includes a syringe pump set up with a syringe loaded with the gelatin/fibrinogen solution. The rotating translating mandrel is enclosed in an acrylic housing. (Right) Electrospun constructs after being removed from mandrel before being placed in the cross-linking chamber.

For each construct, the loaded syringe dispensed 350 μL of the biopolymer solution at a rate of 30 μL/min. The high voltage difference created a driving force that pulled the polymer from the solution forming fibers, which were deposited onto the grounded rotating translating mandrel. After electrospinning, the newly created fibrous constructs were removed carefully from the mandrel. The constructs were then placed into a desiccant chamber containing 25% (v/v) liquid glutaraldehyde (GLUT) at the bottom of the chamber for crosslinking. The constructs were suspended inside the chamber and exposed to the GLUT vapor phase for 2, 8 and 24 hours. After crosslinking, the constructs were suspended in a convection oven at 42°C for 24 hours before they were placed in DI water for another 24 hours to maximize the GLUT removal from the constructs. Before mechanical testing, the constructs were placed in Nerl blood bank saline (Thermo Scientific, USA) for conditioning. Representative cross sectional and *en face* views of constructs from each cross-linking time experimental group were captured using a dissecting microscope and are shown in Figure 6.

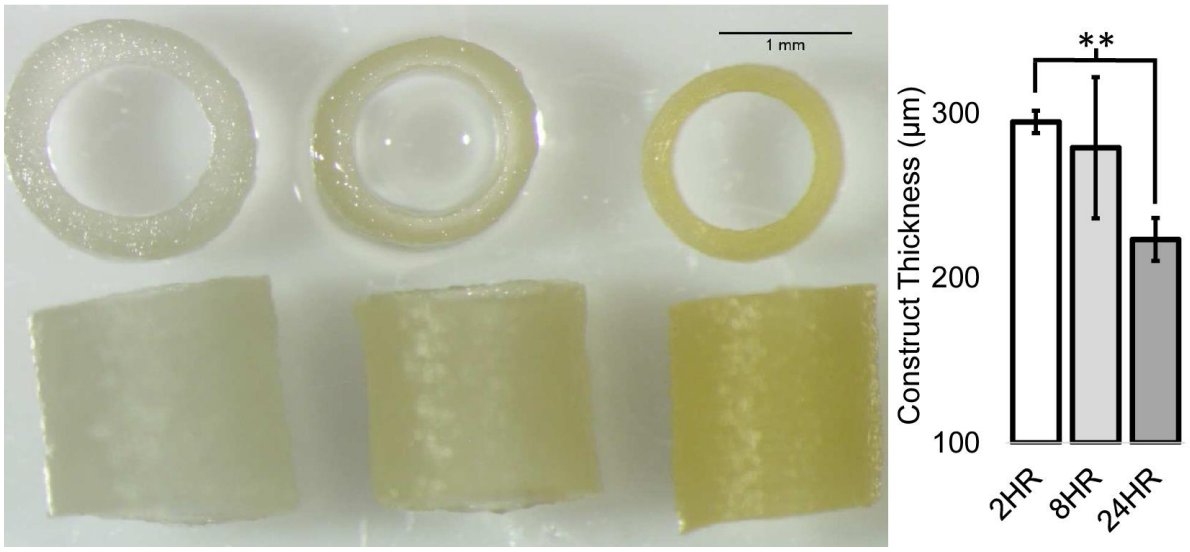

Figure 6. (Left) Representative cross-sectional and *en face* images of construct images (Right) Average thickness of (left to right) 2, 8 and 24 hour crosslinked constructs with error bars indicating standard deviation. Double asterisks indicate p-value < 0.01 (n=3).

2.2 METHODS

2.2.1 Microbiaxial Optomechanical Device

A custom-made microbiaxial optomechanical device (MOD), shown in Figure 7, has been used by our research group to conduct extensive studies on the mechanical behavior of porcine and mouse arteries [133-138]. This device has the capability of stretching the tubular samples axially, while recording axial load, pressure and circumferential/axial strain information simultaneously. Similar to the methods that have been described in the literature published by our research group [133], the mechanical properties of the tubular constructs were assessed both circumferentially and axially. Briefly, each construct and LADC was cannulated on both ends with glass capillary tubes and attached to the MOD system to be intraluminally pressurized in a bath, filled with Nerl blood

bank saline (Thermo Scientific, USA) kept at 37°C. Each construct was preconditioned axially to at least 20% strain at 0.01 mm/sec several times. The constructs were also preconditioned circumferentially by applying an intraluminal pressure from 0 to 120 mmHg at a rate of approximately 1 mmHg/sec seven times. After preconditioning, an axial preload of 3.5 ± 0.4 grams was applied to the construct to allow it to be taut before testing.

According to previous studies by our laboratory group, the *in situ* axial loads for LADCs were found to be around 30g at an axial strain of 34 ± 6% [133]. Therefore, for circumferential testing, each construct and LADC was axially stretched at a rate of 0.01 mm/sec to axial loads of 0g, 10g and 30 g (above the axial preload) at 0 mmHg, which correspond to 0%, 33% and 100% of LADC *in situ* axial loads, respectively. At each axial load, the constructs were pressurized from 0 to 120 mmHg and then back down to 0 mmHg at a rate of approximately 1 mmHg/sec. For axial testing, the pressure was kept constant at 0, 70 and 120 mmHg and the constructs were stretched axially to about 20% axial strain at a rate of 0.01 mm/sec. For all tests, the axial load and the intraluminal pressure were monitored and recorded. Furthermore, the outer radius and axial strain were tracked using image processing software integrated into the MOD. This software tracked the outer radius and the local axial Green strain during biaxial mechanical testing, based off real-time marker tracking of two small cyanoacrylate/ceramic powder markers placed on the constructs.

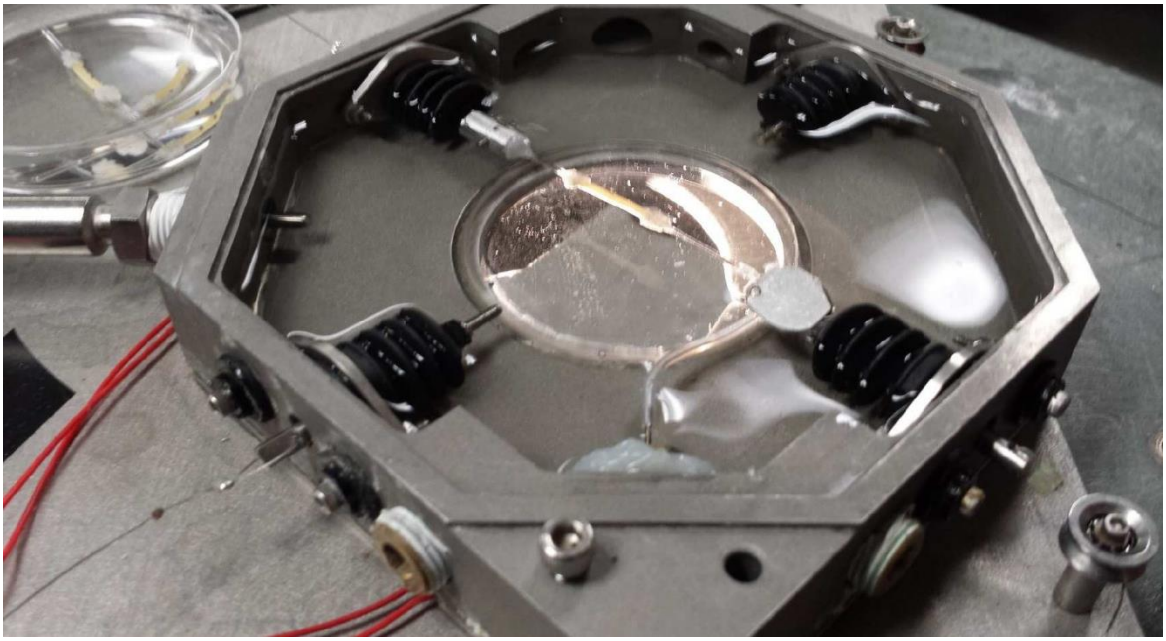

Figure 7. Gelatin/fibrinogen tubular construct loaded into the bath of the microbiaxial optomechanical device.

2.2.2 Constitutive Modeling

Equation (2-1) was used to calculate the circumferential Green strain, which assumes no shear in the sample:

$$E_{\theta\theta} = \frac{1}{2}(\lambda_\theta{}^2 - 1) \tag{2-1}$$

where $E_{\theta\theta}$ and λ_θ are the circumferential Green strain and the circumferential stretch ratio (unitless), respectively. λ_θ is defined as r_o/R_o, where r_o is the deformed outer radius (m) and R_o is the undeformed outer radius (m). Similarly, axial Green strain was determined by using Equation (2-2):

$$E_{zz} = \frac{1}{2}(\lambda_z{}^2 - 1) \tag{2-2}$$

where E_{zz} is the axial Green strain, and λ_z is the axial stretch ratio (unitless). λ_z is defined as l/L, where l and L are the deformed distance (m) and the undeformed distance (m) between the markers parallel to the construct longitudinal axis, respectively. The axial Cauchy stress was determined using Equation (2-3):

$$\sigma_{zz} = \frac{f}{a} \tag{2-3}$$

where σ_{zz}, f and a are the Cauchy stress (Pa), the axial force (N) and the deformed cross-sectional area (m^2), respectively. Assuming incompressibility (constant volume), the deformed and undeformed cross-sectional areas were related using Equation (2-4):

$$a = \frac{AL}{l} = \frac{A}{\lambda_{zz}} \tag{2-4}$$

where A is the construct undeformed cross-sectional area. The hoop stress at the midpoint of the construct/LADC thickness was calculated using a thick-wall assumption by using Equation (2-5) [139]:

$$\sigma_{\theta\theta}|_{r=\frac{r_i+r_o}{2}} = P\left[\frac{(\frac{2*r_o}{r_i+r_o})^2+1}{r_o/r_i{}^2-1}\right] \tag{2-5}$$

where $\sigma_{\theta\theta}$ is the hoop stress (Pa), P is the intraluminal pressure (Pa), r_o is the outer radius of the construct (m), and r_i is the inner radius (m). Equation (2-5) determines hoop stress at the midpoint between r_o and r_i, which was assumed to be the representative hoop stress of the construct throughout the construct thickness. The circumferential and axial 2nd Piola Kirchhoff stresses, $S_{\theta\theta}$ and S_{zz}, respectively, were calculated using Equation (2-6) and Equation (2-7), respectively, assuming no shear stresses:

$$S_{\theta\theta} = \frac{\sigma_{\theta\theta}}{(1 + 2E_{\theta\theta})} \tag{2-6}$$

$$S_{zz} = \frac{\sigma_{zz}}{(1 + 2E_{zz})} \tag{2-7}$$

The stress-strain data were fit to the following modified Fung stain-energy constitutive equation [133]:

$$W = \frac{c}{2}(e^{Q} - 1) \tag{2-8}$$

where $Q = \mathcal{A}_1 {E_{\theta\theta}}^2 + \mathcal{A}_2 {E_{zz}}^2 + 2\mathcal{A}_3 E_{\theta\theta} E_{zz}$, W is the strain energy density, and c (kPa), $\mathcal{A}_1$, $\mathcal{A}_2$, and $\mathcal{A}_3$ are material constants. Coefficients of determination (R^2) and qualitative visual assessment were used to evaluate the accuracy of the fit.

2.2.3 Generation of Averaged Stress-Strain plots

For each construct replicate from each experimental group, the axial and circumferential 2nd Piola Kirchhoff stresses were plotted against the circumferential and axial Green strain, respectively. In order to average the mechanical data for all the replicates for each experimental group, the data from each replicate was fit to a third order single variable polynomial equation. R^2 values and visual assessment were used to evaluate the accuracy of the fit. The resulting fitted polynomial curve for each replicate was averaged within the same experimental group in strain ranges that overlapped between the replicates. These plots were generated for all experimental groups, including the LADC.

2.2.4 Generation of Averaged Stress-Strain Plots

The circumferential tangential moduli (CTM) and the axial tangential moduli (ATM) were extracted from each stress-strain curve by calculating the derivatives of the fitted polynomial curve for each test replicate ($\frac{\partial S_{\theta\theta}}{\partial E_{\theta\theta}}$ and $\frac{\partial S_{zz}}{\partial E_{zz}}$ for CTM and ATM, respectively). All ATM and CTM values were averaged for the same experimental group. The CTM were determined at pressures of 0, 70 and 120 mmHg for the circumferential stress-strain curves at axial loads of 0, 10 and 30 g. The ATM were determined at axial Green strains of 0, 0.05, 0.1 and 0.15 for the axial stress-strain plots at 0, 70 and 120 mmHg. These values were plotted against the equivalent values for the LADC comparison. To determine statistical significance, a two-factor ANOVA was performed to determine the effect(s), if any, of axial load and cross-linking time on the CTM. In addition, a two-factor ANOVA was performed to determine the effect(s), if any, of intraluminal pressure and cross-linking time on the ATM. To determine the statistically significant factors, individual two-

sample two-tailed t-tests were conducted *post hoc* comparing the circumferential and axial tangential moduli of each experimental group to that of the LADC. For all statistical tests, a critical *p*-value value of 0.05 was used to define significance.

2.2.5 Compliance and Statistics

To calculate the compliance of each experimental group at each axial load, Equation (2-9) was used [42]:

$$Compliance\ (mmHg^{-1}) = \frac{(D_{120} - D_{70})/D_{70}}{50\ mmHg} \tag{2-9}$$

where D_{120} is the diameter of the vessel at 120 mmHg (m) and D_{70} is the diameter of the vessel at 70 mmHg (m). Each construct and LADC was preconditioned circumferentially until the compliance value no longer changed (reached steady state). At that point, the compliance value was measured and recorded. A two-way ANOVA was performed to determine the significance of the effect of axial load and crosslinking time on compliance.

2.2.6 Mechanical Response Surfaces

For further construct mechanical characterization and visualization, the axial and circumferential 2nd Piola Kirchhoff stresses of each biaxial mechanical test were plotted against the axial Green strains and the circumferential Green strains in a 3D scatter plot. A surface plot was generated for each replicate by fitting the data generated by the axial and circumferential tests to a multivariable exponential equation. R^2 values and visual assessment were used to evaluate the accuracy of the

fit. The individual surface plots for each test of the same experimental group were averaged to generate an averaged surface plot. Furthermore, adding and subtracting one standard deviation to and from the averaged plot was performed to generate upper limit and lower limit surface plots for each experimental group, respectively.

2.2.7 Construct Fiber Orientation: Multiphoton Imaging

To further characterize the gelatin/fibrinogen constructs and to investigate possible explanations for any mechanical anisotropy, the constructs were imaged using the Advanced Intravital Microscope (AIM) for multiphoton imaging at the University of Arizona's BIO5 institute [137] at 0 mmHg intraluminal pressure with no axial stretch. The AIM is a Zeiss LSM 510 NLO upright laser-scanning microscope (Carl Zeiss) coupled to a Mira 900 150-fs pulsed Ti-Sapphire laser (Coherent). An Olympus XLUMPLFL 20x water immersion objective with a numerical aperture of 0.9 was used to collect the backscattered signal over a 2505 x 2505 μm field of view at 2 μm z-steps, resulting in multiple 2-photon images of the fiber autofluorescence imaged to a depth of about 120 μm. This autofluorescent signal was split with a 580 nm dichroic mirror and collected through a 550/88 bandpass filter. All slice images were combined into a maximum intensity projection. This imaging process was performed for the constructs crosslinked for 2, 8 and 24 hours. An in-house Matlab image processing software Image Analysis Graphical User Interface (IAGUA) was used to determine intensity values for each fiber orientation angle based on the maximum intensity projection image for each experimental group [134, 135]. This generated in fiber angle histograms that display the fiber orientation distribution, which were used to qualitatively determine the effect of crosslinking on fiber orientation.

2.3 RESULTS

2.3.1 Stress-Strain Curves

The maximum average circumferential stresses for all axial loads for the 2, 8 and 24 hour constructs at 120 mmHg were 37.9 ± 2.8 kPa, 33.0 ± 9.0 kPa and 39.3 ± 9.6 kPa, respectively, compared to that of the LADC at 64.7 ± 8.4 kPa, nearly double the maximum circumferential stresses of the construct at the same axial loads. The circumferential stress-strain curves, shown in Figure 8, qualitatively demonstrate that crosslinking time changed the material properties of the constructs, specifically increasing the material stiffness in the circumferential direction. The LADC was the only experimental group that exhibited circumferential strain-stiffening. Please note that the negative circumferential strain values resulted from the Poisson effect due to axial stretch. The undeformed diameter for each of these tests were the diameter at zero axial stretch at zero intraluminal pressure.

Due to deformability limitations, some 2-hour constructs snapped at an axial Green strain of about 0.17. Therefore, all experimental groups were plotted up to an axial Green strain of 0.17 for proper comparison. The maximum average axial stresses for the 2, 8 and 24 hour constructs were 189.4 ± 43.0 kPa, 217.6 ± 52.9 kPa and 562.2 ± 74.0 kPa, respectively, at 0.17 Green strain. The LADC exhibited a maximum average axial stress of 156.7 ± 18.2 kPa, which was a value comparable to the maximum axial stresses of the constructs. The axial stress-strain averaged curves, shown in Figure 9, qualitatively suggests that crosslinking time has a strain-stiffening effect for all levels of crosslinking in the axial direction. Strain-stiffening behavior was also noticeable for the LADC, although to a lesser extent (Figure 9).

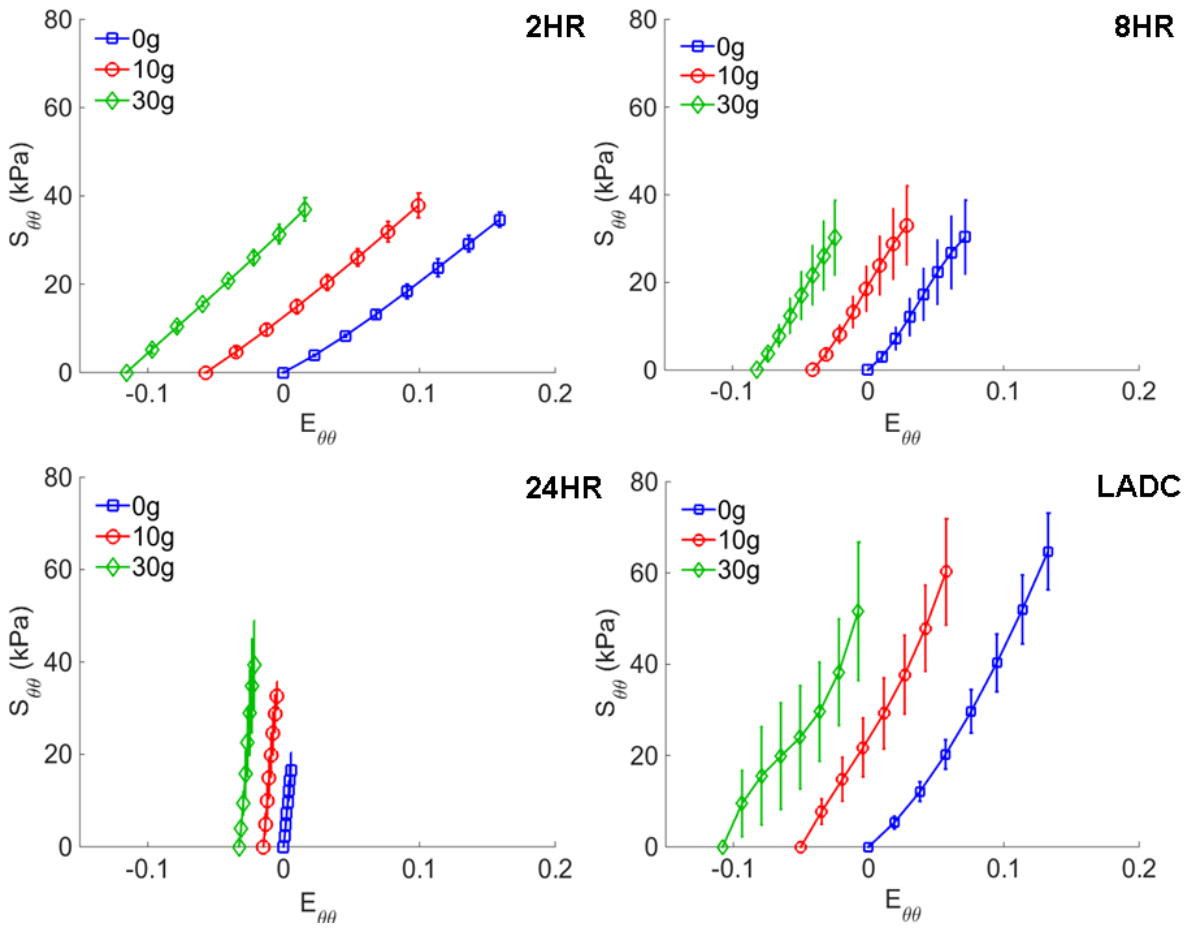

Figure 8. Averaged circumferential stress-strain curves for gelatin/fibrinogen constructs at 0, 10 and 30 g of axial load for constructs crosslinked for 2, 8 and 24 hours and for the distal section of the porcine LADC. This figure illustrates the circumferential stiffening effect of crosslinking time as evident by the increase in curve slope. Error bars represent one standard deviation. Please note that the negative circumferential strain values resulted from the Poisson effect due to axial stretch.

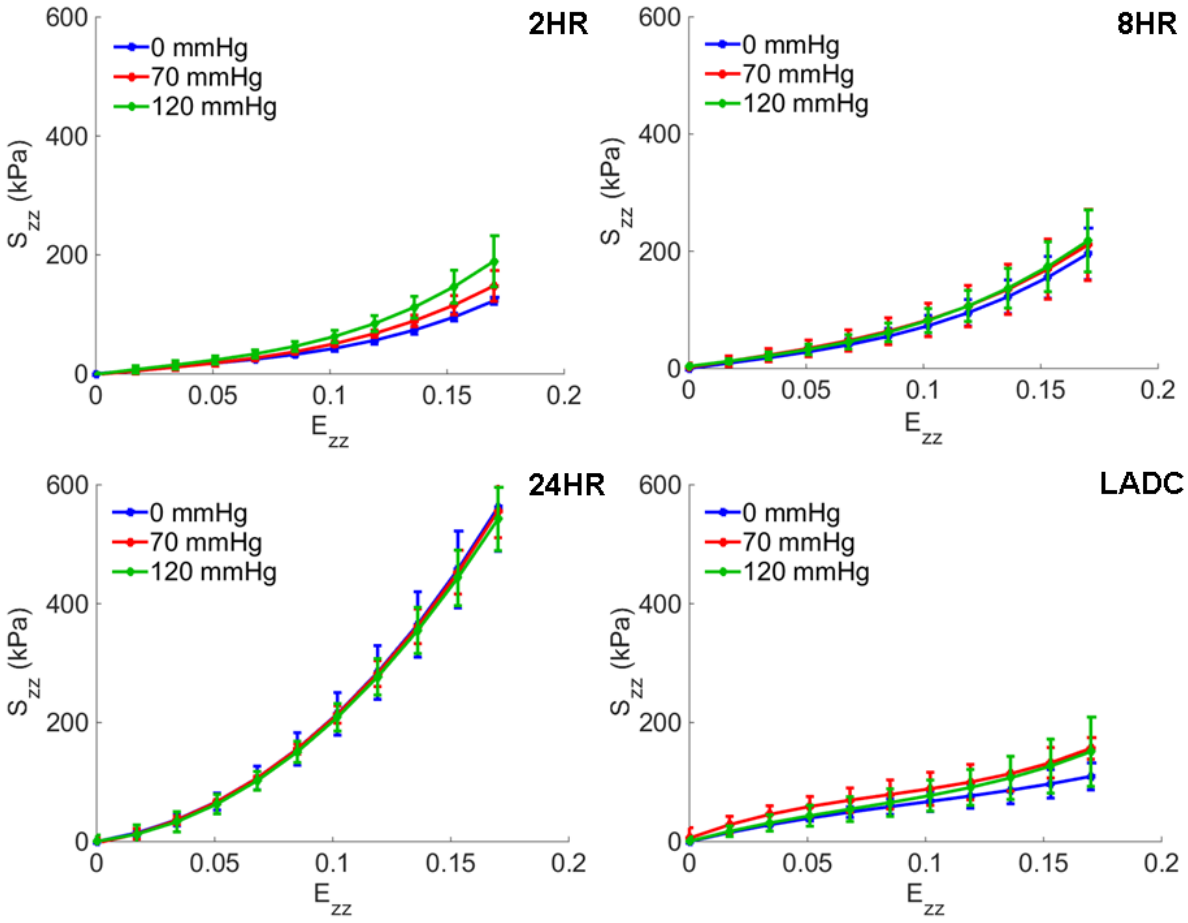

Figure 9. Averaged axial stress-strain curves at 0, 70 and 120 mmHg for gelatin/fibrinogen constructs crosslinked for 2, 8 and 24 hours and for the distal section of the porcine LADCs. This figure illustrates the axial stiffening effect of crosslinking time as evident by the increase in curve slope. Error bars represent one standard deviation.

2.3.2 Tangential Moduli Statistical Results

CTM values were determined at 0, 70 and 120 mmHg for each replicate for all experimental groups at 0g, 10g and 30g axial load. Two-way ANOVA tests were performed to determine the effect of axial load and crosslinking time. Individual two-factor two-tailed t-tests were performed comparing the CTM for each construct experimental group at 0, 70 and 120 mmHg to that of the LADC at 0, 70 and 120 mmHg, respectively. The comparison of CTM values between construct

experimental groups and the LADC is shown in Figure 10. The CTM of the 2-hour constructs were not statistically different compared to the LADC at 0 mmHg with a *p*-value of 0.051. The 8-hour constructs had CTM values not statistically different compared to the LADC at 0 and 70 mmHg with *p*-values of 0.14 and 0.06, respectively. All other CTM comparisons between the constructs and the LADC at different pressures showed statistical significance with *p*-values < 0.01, with some *p*-values < 0.001. The constructs crosslinked for 24 hours showed statistically significant higher values compared to the LADC for all three pressures. Consistent with Figure 8 , Figure 10 shows in more detail the qualitative strain-stiffening behavior of the LADC compared to the constructs, while showing that all three construct experimental groups do not show a strain-stiffening behavior in the circumferential direction.

For the axial tests, the ATM values were determined at axial Green strain values of 0, 0.05, 0.1 and 0.15 for each replicate for all experimental groups for pressures of 0, 70 and 120 mmHg. The comparison of ATM between construct experimental groups and the LADC is shown in Figure 11. The ATM of the 8-hour constructs at 0.05 axial Green strain were not statistically different compared to the LADC at 0.05 axial Green strain with a p-value of 0.88, while the ATM of the 24-hour construct at zero Green strain were not statistically different compared to the LADC at zero Green strain. All other ATM comparisons between the constructs and the LADC at different pressures showed statistical significance with *p*-values < 0.05. As shown in Figure 9, all three crosslinking times displayed an axial strain-stiffening behavior in the axial direction. The LADC did not exhibit the same strain-stiffening for the considered axial Green strain range.

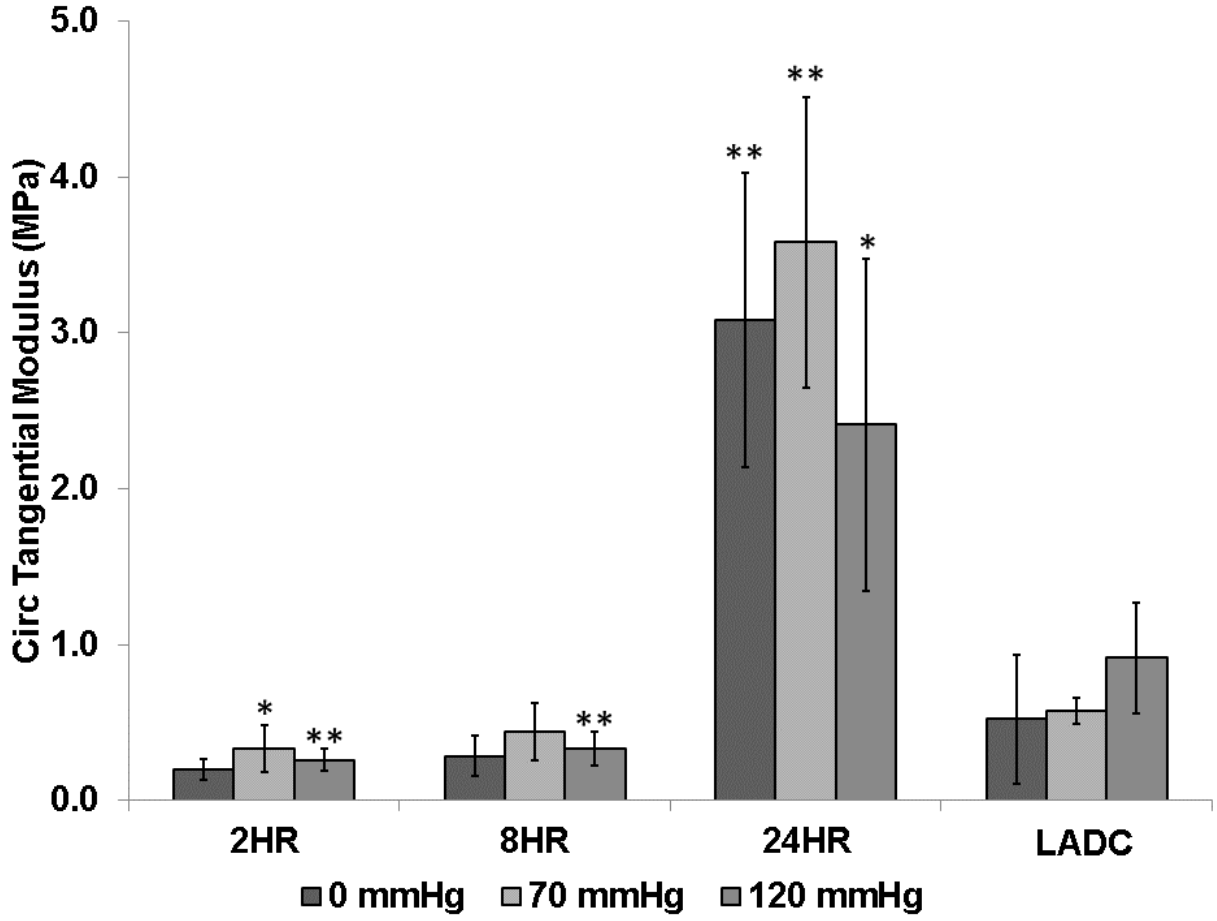

Figure 10. Circumferential tangential moduli comparison between experimental groups and the LADC at 0, 70 and 120 mmHg. The asterisks indicate statistical significance of the difference between each constructs experimental group and the porcine LADC at the respective pressures, with a single asterisk indicating a p-value < 0.01 and double asterisks indicating a p-value < 0.001. In terms of circumferential tangential modulus, the graphs shows that the 2 hour and 8 hour constructs have the most similarity to the LADC.

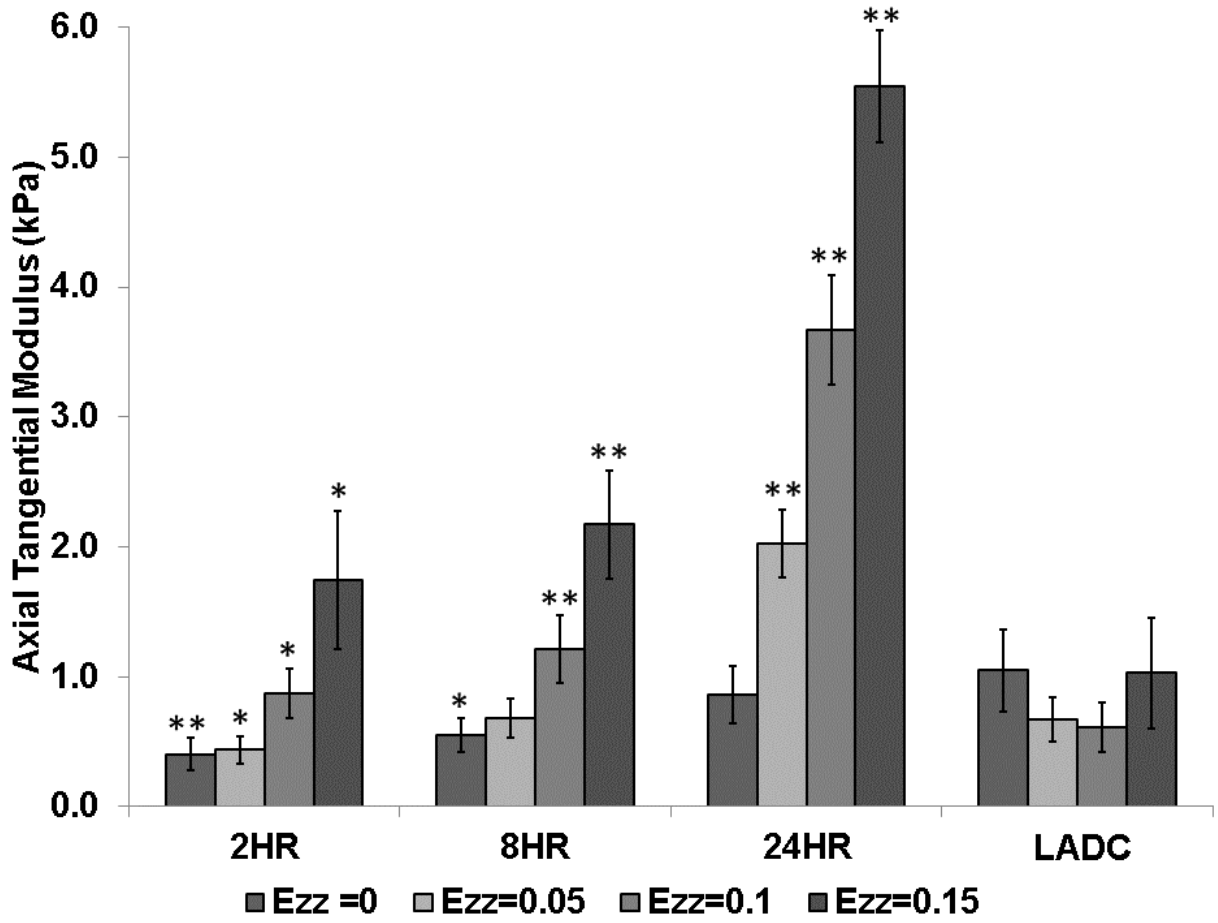

Figure 11. Axial tangential modulus comparison between experimental groups and the LADC at axial Green strain values of 0, 0.05, 0.1 and 0.15. The asterisks indicate statistical significance of the difference between each constructs experimental group and the porcine LADC at the respective axial Green strains, with a single asterisk indicating a p-value < 0.05 and double asterisks indicating a p-value < 0.001. The graph shows that the all constructs were strain stiffening while the LADC was not. In terms of axial tangential modulus, there were a few similarities between the 8 and 24 hour constructs and the LADC.

2.3.3 Compliance

Similar to the CTM, the two-way ANOVA test revealed that the effect of crosslinking time on compliance was significant with a *p*-value < 0.0001. The effect of axial load was not significant with a *p*-value of 0.54, with no significant interaction between these two factors with a *p*-value of 0.35. So the compliance values of the same experimental group were grouped together and a two-tailed two-factor t-test was performed to compare the compliance values of each experimental group to the LADC. The 8-hour constructs compliance values (0.00060 ± 0.00018 $mmHg^{-1}$) were not significantly different from the LADC (0.00071 ± 0.00027 $mmHg^{-1}$) with a *p*-values of 0.36. The 2-hour and 24-hour constructs showed compliance values of 0.0012 ± 0.00013 $mmHg^{-1}$ and 0.00007 ± 0.00003 $mmHg^{-1}$, respectively. Both compliance values were statistically different than that the LADC and rat aorta with *p*-values < 0.01 for all comparisons. The comparison of compliance between experimental groups and the LADC is shown in Figure 12. The only experimental group that exhibited compliance matching was the 8-hour experimental group (*p*-values = 0.36). The construct compliance decreases with crosslinking time, which is consistent with trends shown by the circumferential stress-strain curves and CTM graphs (Figure 12).

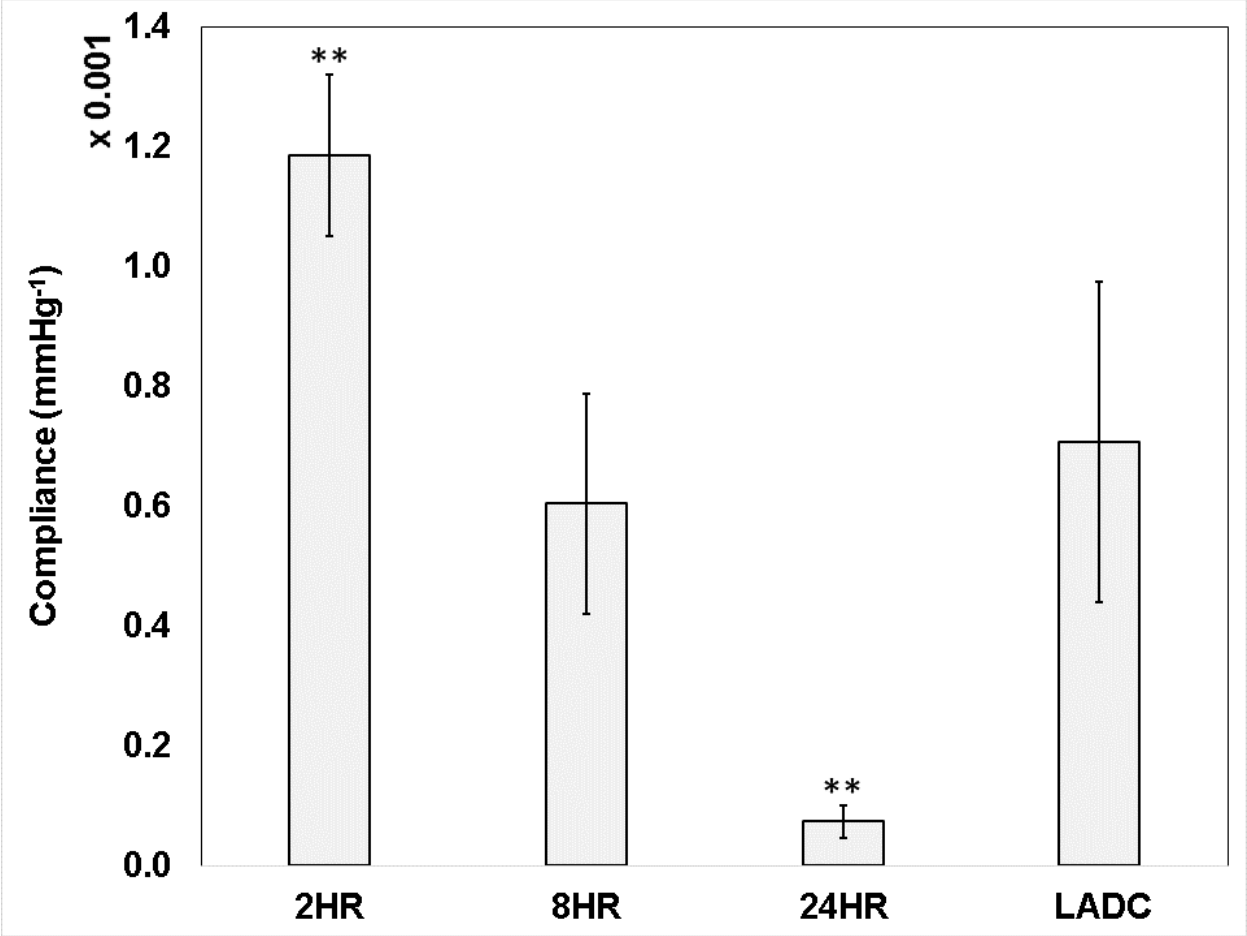

Figure 12. Compliance comparison between experimental groups and the LADC. The asterisks indicate statistical significance of the difference between each constructs experimental group and the LADC at the respective axial Green strains, with double asterisks indicating a p-value < 0.001. The only experimental group that exhibited compliance matching to the porcine LADC was the 8-hour experimental group (p-values = 0.36)

2.3.4 Stress-Strain Surface Plotting

The circumferential and axial stress-strain Fung fit surfaces for all the experimental groups are shown in Figure 13 and Figure 14, respectively, which display data for strain ranges in which all three replicates overlap. The strain ranges were restricted by deformability limitations exhibited by the crosslinked material. This is especially noticeable in Figure 14 where crosslinking time reduces the circumferential strain range. In addition, both Figure 13 and Figure 14 show that the range of data collected for the LADC were larger compared to the constructs. This is due to the LADC having the capacity to endure higher stresses and strains compared to the gelatin/fibrinogen constructs. The Fung equation constants, R^2 values and the strain energy density values, W, at 30g axial load for 70 and 120 mmHg intraluminal pressure for each experimental group are shown in Table 1, which displays the fitted constants for the average, upper limit and lower limit Fung equation surface plots. Overall, the Fung strain energy equation accurately captures the behaviors of the material with the highest and lowest R^2 values for the 24-hour constructs and LADC at 0.94 ± 0.02 and 0.79 ± 0.04, respectively. Table 1 also displays $\mathcal{A}_2/\mathcal{A}_1$ as a measure of anisotropy for the constructs.

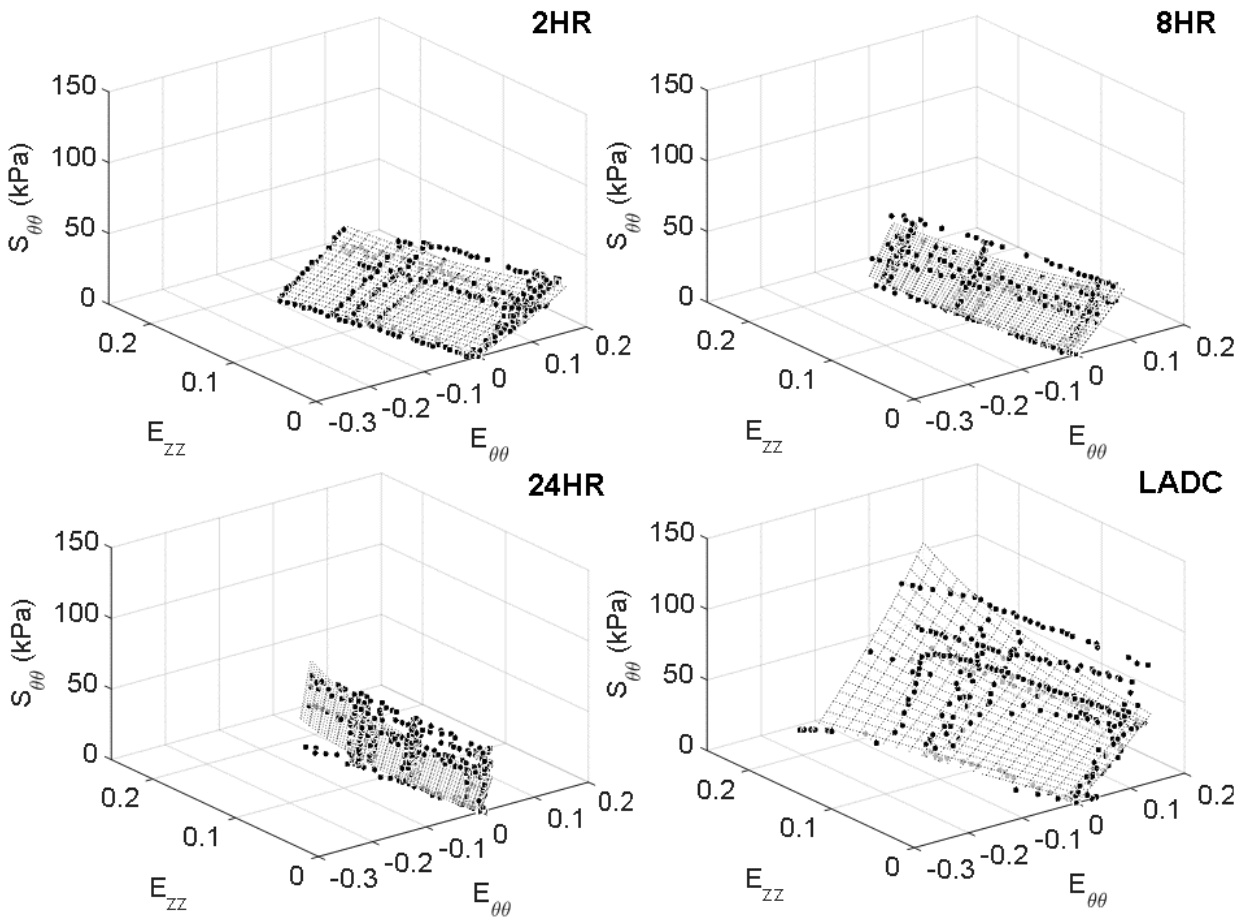

Figure 13. Circumferential stress-strain fitted Fung equation surface plots for each experimental group plotted against data points from all three replicates displayed for fit evaluation and visualization. The surface plots and data points are shown only for strain ranges that overlap between all three replicates.

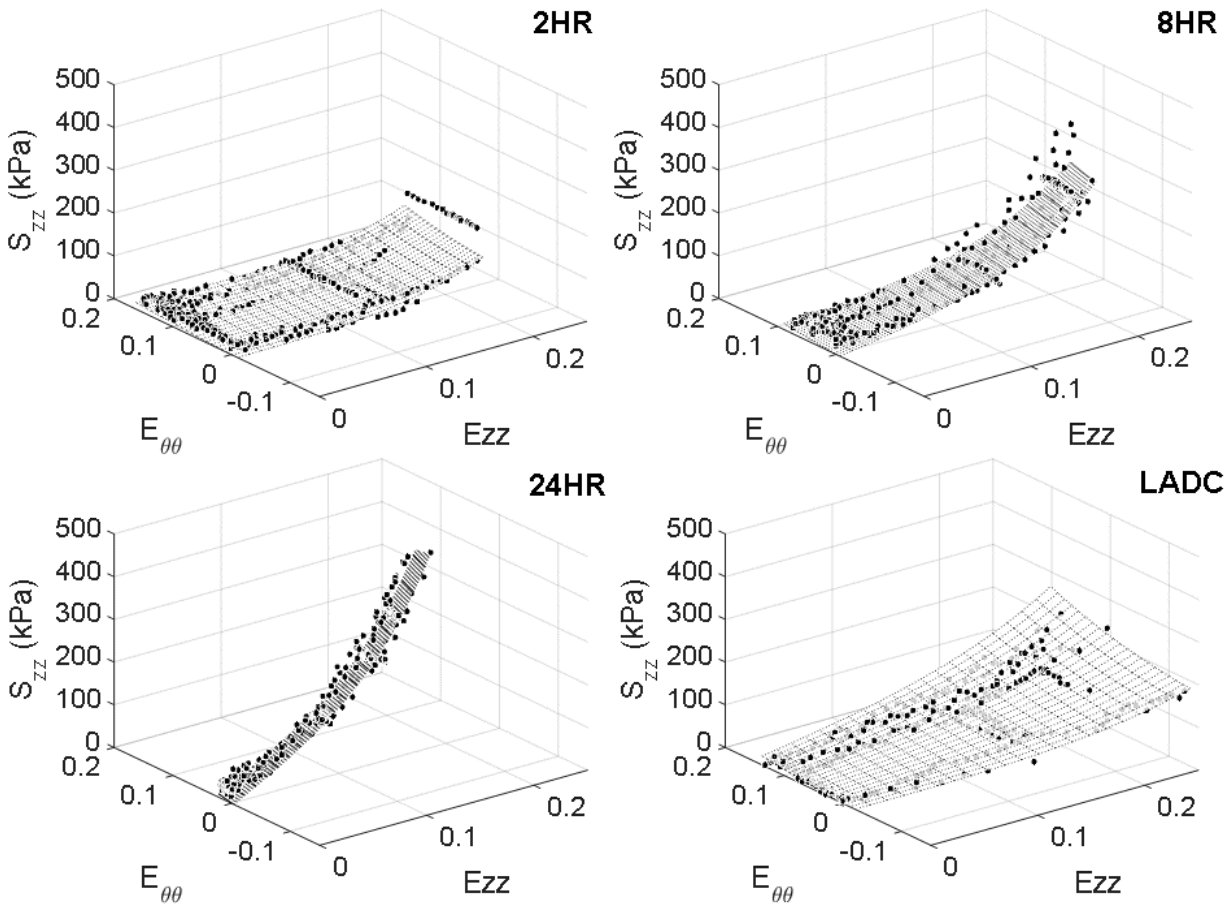

Figure 14. Axial stress-strain fitted Fung equation surface plots for each experimental group plotted against data points from all three replicates displayed for fit evaluation and visualization. The surface plots and data points are shown only for strain ranges that overlap between all three replicates.

Table 1. Fung strain energy equation constants, $\mathcal{A}_2/\mathcal{A}_1$ values, R^2 values for the average, upper and lower limit Fung equation surfaces. One standard deviation was added to and subtracted from the averaged plot surface to generate upper limit and lower limit surface plots for each experimental group, respectively. R^2 values compare the Fung equation surface plots to the combined data points of all three replicates for the respective experimental group.

Group	Dataset	c (kPa)	$\mathcal{A}_1$	$\mathcal{A}_2$	$\mathcal{A}_3$	$\mathcal{A}_2/\mathcal{A}_1$	R^2
2HR	Upper Limit	23.7	7.3	24.0	3.3	3.3	0.71
	Average	31.0	5.6	18.4	2.6	3.3	0.90
	Lower Limit	50.5	3.4	11.4	1.7	3.3	0.91
8HR	Upper Limit	54.4	9.2	17.7	3.5	1.9	0.77
	Average	49.1	7.9	16.7	3.0	2.1	0.88
	Lower Limit	44.6	6.3	15.1	2.3	2.4	0.76
24HR	Upper Limit	87.3	13.1	23.7	4.5	1.8	0.94
	Average	83.6	12.1	22.6	4.1	1.9	0.96
	Lower Limit	80.6	10.9	21.3	3.6	2.0	0.92
LADC	Upper Limit	73.5	4.8	9.0	2.2	1.9	0.79
	Average	87.4	3.8	7.1	1.6	1.9	0.82
	Lower Limit	126.5	2.4	4.7	0.9	1.9	0.75

2.3.5 Multiphoton Imaging and Fiber Orientation

Qualitatively, the fiber orientation analysis showed the constructs becoming less fibrous and denser with crosslinking time. There was a slight change in fiber orientation as crosslinking time increased with most of the fibers qualitatively oriented in the circumferential direction for all three crosslinking times. These maximum intensity projection images and the fiber orientation distributions are shown in Figure 15, in which 90° angles corresponds to fibers oriented in the circumferential direction, 0° and 180° angles correspond to fibers oriented in the axial direction.

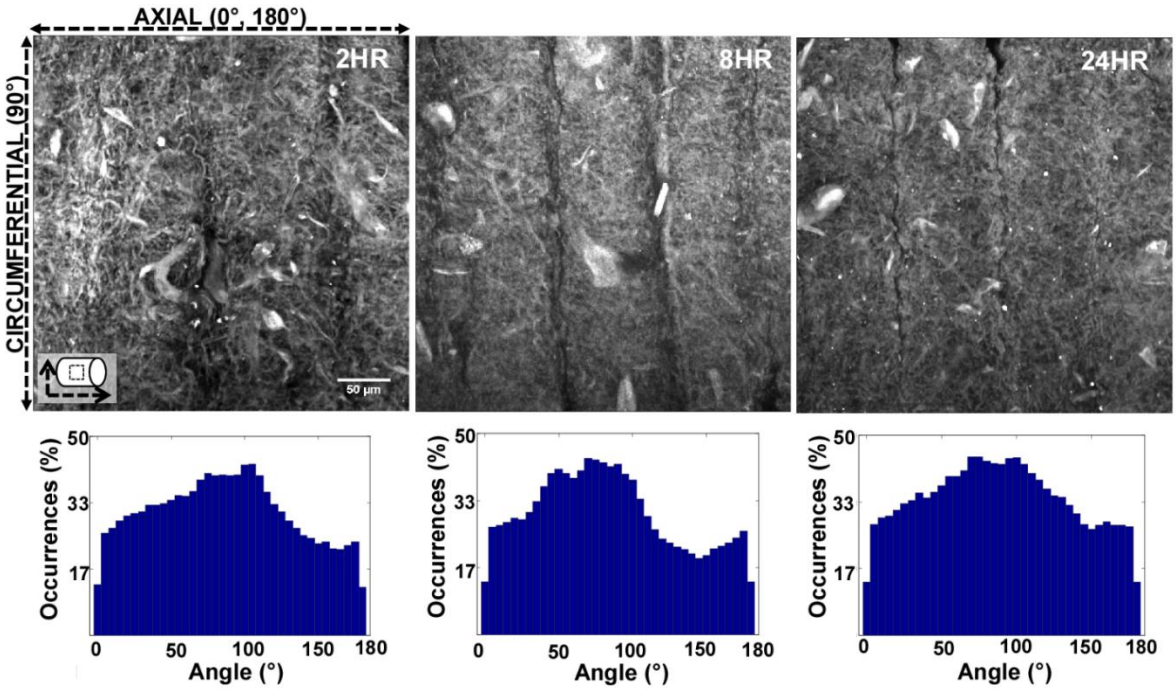

Figure 15. Representative maximum intensity projection images obtained from multiphoton imaging (Top), and fiber orientation distribution histograms (Bottom) of the constructs crosslinked for 2, 8 and 24 hours. 90° angles corresponds to fibers oriented in the circumferential direction, 0° and 180° angles correspond to fibers oriented in the axial direction. Please note that the gelatin/fibrinogen constructs become less fibrous and more dense as crosslinking duration increases.

2.4 DISCUSSION

Electrospun cylindrical constructs were fabricated from gelatin/fibrinogen and crosslinked in a GLUT vapor chamber for 2, 8 and 24 hours. The constructs were then mechanically characterized in a tubular biaxial mechanical configuration and compared to porcine LADC and rat aorta. The axial stress-strain response surfaces for constructs crosslinked for 8 hours were most qualitatively similar to the LADC in the circumferential direction, while both circumferential stress-strain response surfaces of the 2 and 8 hour constructs were qualitatively similar to the LADC. The 24-

hour constructs were stiffer in both directions compared to the LADC for most of the studied pressures and axial strains. All constructs exhibited anisotropic mechanical behavior, which is consistent with the LADC and most soft tissues. It should be noted that the $\mathcal{A}_2/\mathcal{A}_1$ values (measure of anisotropy) qualitatively increased as a function of crosslinking duration. The $\mathcal{A}_2/\mathcal{A}_1$ values of 8-hour and 24-hour constructs were comparable to that of the LADC. The Fung strain energy function was shown to be a suitable constitutive model to simulate the behavior of all three construct experimental groups and the LADC. The surface plots shown in Figure 13 and Figure 14 allow a comprehensive comparison between the different experimental groups over different circumferential and axial strain ranges. It should be mentioned that we additionally considered the Holzapfel constitutive model [140] as a possible strain energy model to fit to the construct experimental data. However, when evaluated, it was found that the R^2 values of the Fung model fit were qualitatively higher than that of Holzapfel model for all experimental groups. Furthermore, the Fung model was found to be visually more representative of the experimental data. Based on these findings, the Fung equations were used as the only constitutive model to represent the biomechanical data of the constructs in this study.

Fiber orientation realignment is one important factor to evaluate when considering explanations to the crosslinking effect on mechanical properties. Since the stiffening effect is noticeable in both directions, it would be unlikely that fibers realigned in one direction versus the other, as realigning in one direction would stiffen that specific direction and not the other. The absence of fiber realignment is confirmed in the fiber angle orientation analysis, where the representative multiphoton images from each crosslinking time qualitatively show no change in fiber angle distribution due to crosslinking. Therefore, it is more likely that crosslinking alters the mechanical properties of the material by changing the molecular structure of the actual

gelatin/fibrinogen fibers, which resulted in the overall change in mechanical properties of the constructs. Furthermore, most of the fibers seemed to be oriented in the circumferential direction for all three crosslinking times, which may explain the anisotropic behavior of theses constructs. The effect of crosslinking can also be further determined by analyzing $\mathcal{A}_3$ values, which can be seen as a coupling term between fiber in the axial and circumferential direction, as shown in Equation (2-8). It ca be noted that as crosslinking increased, biaxial fiber coupling also increased (as indicated by the increase in $\mathcal{A}_3$). This could further explain the mechanism of GLUT crosslinking of gelatin/fibrinogen fibers.

Many researchers have mechanically evaluated vascular grafts [42, 56, 62, 77, 84, 99, 141]. Some authors fabricated their grafts from synthetic polymers. Tai et al. fabricated and calculated compliance values of three types of isotropic vascular grafts composed of synthetic polymers using a patented chemical method, which involves low-temperature cast coagulation onto a rotation and translating steel mandrel [42]. Compliance values of the synthetic grafts were compared to that of human muscular artery. The results showed that only the graft made of poly(carbonate)polyurethane compliance-matched the artery with average compliance values of 0.00081 ± 0.00004 $mmHg^{-1}$ and 0.00080 ± 0.00059 $mmHg^{-1}$, respectively. These compliance values were in the same order of magnitude of the compliance values of our 8-hour constructs, the porcine LADC and rat aorta, which showed compliance values of 0.00060 ± 0.00018 $mmHg^{-1}$, 0.00071 ± 0.00027 $mmHg^{-1}$ and 0.00057 ± 0.00031 $mmHg^{-1}$, respectively. In our study, electrospinning was used as the fabricating method to create fibrous constructs which, similar to arteries, exhibited anisotropic mechanical behavior. In contrast to Tai et al. [42], our study focused on using non-synthetic endogenous biopolymers to fabricate vascular grafts.

Other groups have electrospun biopolymers but provided little information on mechanical performance [60, 61, 142]. However, several reports mechanically characterized of vascular grafts assumed they are linear, isotropic, and undergo infinitesimal deformations. Kumar et al. [56] fabricated acellular vascular grafts composed of collagen and elastin, and evaluated their strength using planar tensile testing to quantify compliance, burst pressure, and Young's modulus. Likewise, Mitra et al. [141] evaluated the mechanical effect of crosslinking on collagen scaffold tensile strength alone. McClure et al. [84] subjected TEVGs composed of polydioxanone, elastin and collagen to cyclic uniaxial loading and determined tangential moduli, peak stress and strain at break. In the case of gelatin, Zhang et al. [99] created electrospun crosslinked and non-crosslinked gelatin flat sheets and briefly mechanically evaluated them by measuring stress and strain and calculating Young's modulus. Balasubramanian et al [77] electrospun fibrous flat sheets composed of gelatin and fibrinogen crosslinked with GLUT at different ratios including an 80:20 ratio, which is consistent with the ratio used in our study. Their study found the Young's modulus values for their gelatin/fibrinogen scaffolds using uniaxial tests to be 0.46 MPa. This is comparable to the CTM values of our 2-hour constructs at low pressures (0.20 MPa), but not comparable to the ATM values at low axial strains for the same 2-hour constructs (0.40 kPa). This may be explained by a higher number of fibers aligned in the circumferential direction as previously shown in Figure 15. The difference between CTM and ATM values for all our experimental groups highlights the importance of considering the inherent anisotropy of electrospun scaffolds. Our research team is currently investigating the source of mechanical anisotropy by using the MOD and nonlinear optical microscopy to investigate the load dependent changes in construct microstructural organization.

Published works in the literature fit experimental biomechanical data of native vasculature to constitutive models [143, 144] and supports work from our own group [134, 135, 145]. Some studies have used constitutive modeling to fit biomechanical data of developed synthetic TEVGs [146, 147]. However, few researchers have used constitutive modeling as a means of comparing TEVGs to native tissue. Mandru et al. [148] characterized porcine carotid and thoracic arteries by fitting experimental data to a power law model and a polynomial equation for hyperelastic material. They also compared the longitudinal Young's moduli value of the native artery to that of TEVGs fabricated from PTFE and Dacron. However, this study does not use constitutive modelling. Our modeling approach compares non-synthetic TEVGs and native LADC data using the same models, including anisotropy, as is shown in Table 1.

The current study evaluates the mechanical behavior of gelatin/fibrinogen cylindrical constructs crosslinked with GLUT for three different periods of time. The constructs are compared to native porcine LADC and rat aorta and the collected data suggested that some of the construct groups behaved very similarly to the LADC and rat aorta. The results of this study suggest that it is possible to modify the mechanical properties to meet specifications required by vascular graft transplantation through manipulating the crosslinking time. Complete mechanical biaxial characterization of tubular biopolymer constructs is currently lacking in the literature. This study offers a comprehensive method of evaluating electrospun crosslinked biopolymer cylindrical constructs in the circumferential and axial direction at physiological conditions. However, the effect of crosslinking on biocompatibility and biodegradability remains unknown. Our laboratory has already shown that SMCs can grow with excellent viability on the gelatin/fibrinogen fibers used to fabricate the constructs discussed in this paper after being crosslinked with GLUT [90].

Preliminary qualitative studies in our laboratory suggested that seeded SMCs mechanically modulate gelatin/fibrinogen constructs. Future studies will further investigate this effect and will be focused on the mechanism in which SMCs remodel the fibrous constructs, which would shed light on methods of reducing manufacturing time for TEVGs while maintaining mechanical integrity. Blood compatibility and thrombogenicity remain important factors for these constructs and should be evaluated. To accommodate this concern, possible modifications to the constructs could include surface modification to the lumen of the construct by making it more hydrophilic, which would inhibit protein absorption. Our laboratory is also currently focused on endothelializing the construct lumen of our constructs. The immunogenicity and inflammation due to the presence of the gelatin/fibrinogen construct is another concern. While gelatin has been shown to have a reduced antigenic response in animal models, Telemeco et al. [149] reported that grafts made of electrospun gelatin produced a foreign body giant cell response and fibrosis. It should be noted that *in vivo* physiological responses depend on the material chemistry of the graft. Gelatin can have different exposed functional groups, depending on the extraction process and source [88]. The gelatin grafts developed by Telemeco et al. were not placed in their animal model in a functional position as they were implanted subcutaneously and not as vascular conduits. Furthermore, preliminary results from our recent *ex vivo* experiments have shown our gelatin/fibrinogen constructs to be biodegradable, and therefore, any signs of inflammation and immunogenicity could be reduced as the gelatin becomes degraded and replaced with native ECM.

For full clinical translational use of this approach one must consider issues related to potential toxicities of the crosslinking agent used in this study. While GLUT is utilized for preservation of implant biologic materials such as valves, cartilage and tendons [54, 150-152], there have been many studies that reported information regarding cytotoxicity and immunogenicity

of using GLUT as a crosslinking agent in the literature [101, 153-155]. Most of these studies do not discuss the *in vivo* responses due to the presence of biopolymer grafts crosslinked with GLUT vapor. Tillman et al. [156] investigated the patency and structural integrity of PCL/collagen constructs crosslinked with GLUT and found that their constructs do not elicit abnormal inflammatory responses. All these different factors are important considerations in developing suitable clinical tissue-engineered constructs for use in the benefit of CVD patients.

The current study has a number of limitations. The gelatin/fibrinogen constructs showed little to no strain-stiffening in the circumferential direction compared to the LADC, which showed clear strain-stiffening behavior as shown in Figure 8. However, none of the constructs reached the circumferential stresses reached by the LADC due to limited construct deformability. It is possible that these constructs could be strain-stiffening in the circumferential direction if allowed to experience similar circumferential stress by increasing the pressure, increasing the undeformed radius and/or decreasing the undeformed thickness. Furthermore, the LADC may display strain-stiffening behavior in the axial direction at higher axial strains not shown in Figure 9. However, the comparison was limited by low allowable axial strains of the 2-hour construct experimental group, which were stretched to failure around an axial Green strain of 0.18. These strain limitations are more clearly shown in the Fung strain energy surface plots displayed in Figure 13 and Figure 14, where the LADC surface plot does extend over a larger axial strain compared to the constructs in both directions. The addition of other biopolymers, such as collagen and tropoelastin, will be investigated as means to provide higher deformability, which could allow these constructs to reach the necessary stresses and strains exhibited by the LADC. Suture retention and burst pressure of the gelatin/fibrinogen constructs were not evaluated in this study. These properties are important indicators to the suitability of constructs to be transplanted and will be further investigated by our

research group. Only non-cellularized electrospun constructs were evaluated in this study. However, ongoing experiments seek to determine the effects of SMC mediated gelatin/fibrinogen remodeling and ECM deposition on construct mechanical properties. Finally, our previous work demonstrated that our gelatin/fibrinogen materials promote cell division, migration, and collagen deposition *ex vivo* [90]. We anticipate that acellular constructs implanted *in vivo* would result in native cell infiltration and remodeling. The degree to which this will lead to function or dysfunction of our construct post-implantation is currently unknown and will require *in vivo* studies that are ongoing by Kenneth Furdella and Dr. Shinichi Higuchi.

2.5 ACKNOWLEDGMENTS

This research was funded by the NIH, grant NHLBI-1R21HL111990-01A1 to JPVG. Imaging was performed on an NIH sponsored shared device NIH/NCRRS10RR023737. We would also like to acknowledge Jamie Hernandez, Corina MacIsaac and Joshua Uhlorn for their assistance and support.

3.0 CHAPTER 3: SPECIFIC AIM 2

Specific Aim 2: *Fabricate TEVGs composed of alternating layers of genipin-crosslinked porcine gelatin and human tropoelastin with varying polycaprolactone (PCL) percentages to compliance-match to rat aorta using an experimental/computational optimization approach.*

In this aim, I sought to use a previously validated computational/experimental scheme to predict the individual thicknesses and protein:PCL ratios of alternating gelatin/tropoelastin layers to create a hybrid (synthetic and non-synthetic) biomimetic TEVG that is compliance matched to rat abdominal aorta. My hypothesis for this chapter is that electrospun TEVGs composed of alternating layers of PCL-enforced genipin-crosslinked gelatin and tropoelastin can be compliance matched to rat aorta by varying the percentage of PCL in each layer. The rationale for this is that electrospun gelatin TEVGs have shown limited deformability compared to rat native artery. Adding layers of PCL and crosslinked tropoelastin is expected to increase deformability and mechanical integrity, while changing the protein percentage of each layer is expected to change material compliance. Computational optimization can be used to determine the correct number of layers, thicknesses of layers and material properties for rat aortic compliance matching.

In Specific Aim1, the constructs were compliance matched to porcine coronary artery due to the availability of that particular data from a previous study [133]. However, a porcine animal model wasn't intended, nor is it suitable, to be the initial animal model for graft implantation.

Therefore, for Specific Aim2, the more appropriate animal model was determined to be rat and the optimized grafts were designed to compliance match to rat aorta.

In the previous aim, there was a limitation on axial strain in which the 2 hour crosslinked snapped around a Green strain of 0.17. Preliminary *in vivo* experiments conducted by my colleague Corina McIsaac demonstrated that gelatin/fibrinogen constructs crosslinked for 24 hours lacked the necessary suture retention during implantation in to Sprague Dawley rats. These experiments concluded that by adding PCL at a percentage of 50%, it was possible to implant these constructs successfully. This was the rationale to adding PCL to the composition of the optimized grafts discussed in this chapter.

However, adding a relatively stiff synthetic polymer like PCL to the composition of the optimized grafts would reduce the elasticity of the grafts. To offset the effect of PCL, tropoelastin was added the composition of these grafts as well. Our laboratory group had previously demonstrated in preliminary experiments that electrospinning cylindrical constructs composed of a blend of tropoelastin and gelatin (66% tropoelastin 33% gelatin) allowed for greater elasticity, deformability, and compliance compared to construct made of exclusively gelatin (100% gelatin). The circumferential stress-strain curves which compare both types of constructs crosslinked with GLUT for 2, 8 and 24 hours are shown in Figure 4.Therefore, by adding tropoelastin to the graft compositions I expected that an increase in the elasticity of our biomimetic TEVGs for better mechanical optimization and deliverability.

As previously mentioned, our research group has previously developed a computational/experimental optimization scheme for compliance matching native tissue by predicting the thickness and glutaraldehyde crosslinking duration time of electrospun gelatin/fibrinogen cylindrical constructs [157]. This program performed finite element simulations

using predicted mechanical properties by interpolating between characterized properties of three crosslinking time points for single layered construct. Native arteries have concentrically arranged matrix of alternating layers of elastin and collagen. In an effort to match this geometry, this chapter aims to create biomimetic multilayered TEVGs with alternating electrospun layers of porcine gelatin and human tropoelastin, which are meant to be analogous to collagen and elastin, respectively

Another primary modification for this chapter is the method of tuning the mechanical properties of the material. If crosslinking duration was to be used as the primary mechanical tuning mechanism (like in the case of Specific Aim 1), all layers of a multilayered construct would receive the same crosslinking duration and each type of layer would not be able to be tuned individually. Therefore, crosslinking duration was not used as the primary parameter of mechanical tunability in this chapter. Instead, I used the ratio of protein to PCL as the primary method of tuning individual layers in the optimization scheme all crosslinked with one crosslinking duration, which was optimized through preliminary trial and error. Due to concerns regarding the toxicity of the previously used glutaraldehyde, I opted to use an alternative crosslinking agent (genipin), which has been shown to exhibit less cytotoxicity and cause less calcification, as previously mentioned in the introduction section (Chapter 1).

Finally, in this study fibrinogen was excluded from the composition of the optimized grafts. Based on the results from the previous aim, fibrinogen was deemed problematic to electrospin as it resulted in large diameter blots in the construct microstructure (Figure 15). Also, cell proliferation numbers on constructs made from 80:20 gelatin:fibrinogen was not noticeably different than constructs made from 100% gelatin (Figure 3) [90].

3.1 MATERIALS AND METHODS

3.1.1 Rat Abdominal Aorta Tissue Acquisition and Preparation

All tissue acquisitions were performed in accordance with approved protocols with the University of Pittsburgh Institutional Animal Care and Use Committee. Male Sprague-Dawley rats (n=13, 175-235 grams) were ordered and sacrificed. Within one hour post-mortem, each rat was dissected and the infrarenal abdominal aorta was extracted. All connective tissues were removed and the sample was placed in 1X phosphate buffered saline (PBS) pH 7.4 (Thermo Fisher Scientific, USA) with 1% (v/v) Gibco Penicillin-Streptomycin 10,000 U/mL (Thermo Fisher, USA) and 1% (v/v) Gibco Amphotericin B (Thermo Fisher, USA) for 24-48 hours post-mortem at 4° C before mechanical testing.

3.1.2 Electrospun Materials

Gelatin extracted from porcine skin (Sigma-Aldrich, USA) and polycaprolactone (PCL) with a molecular weight (MW) ~80,000 (Sigma-Aldrich) were dissolved in 1,1,1,3,3,3-hexafluoro-2-propanol (HFP) (Sigma-Aldrich) at ratios of 80:20, 50:50 and 20:80 (referred to henceforth as 80G:20PCL, 50G:50PCL and 20G:80PCL, respectively) to create 10% (w/v) solutions. Human recombinant tropoelastin was acquired from Protein Genomic (USA), which was produced by fermentation of recombinant E. coli containing pET21a and expression induced by the addition of Isopropyl β-D-1-thiogalactopyranoside. Tropoelastin was solubilized from the lysed cells and purified resulting in approximately 95% purity determined by SDS PAGE electrophoresis. The final product was tropoelastin lyophilized with polyethylene glycol (PEG) into a cake with an end concentration of 0.48 mg tropoelastin/1 mg of cake (referred to henceforth as tropoelastin).

Tropoelastin and PCL with a MW ~80,000 (Sigma-Aldrich) were dissolved in HFP at ratios of 80:20, 50:50 and 20:80 (referred to henceforth as 80T:20PCL, 50T:50PCL and 20T:80PCL, respectively) to create 10% (w/v) solutions.

3.1.3 Fabricating Electrospun Constructs for Material Characterization

A commercial electrospinning device (IME Technologies, Netherlands) was used to create all electrospun constructs in this study. All solutions were loaded into 5 ml BD syringes, which were attached to computer controlled syringe pumps. The syringes were connected to transparent polytetrafluoroethylene (PTFE) tubing (1mm ID x 2mm OD), which fed the solutions into the ventilated insulated electrospinning chamber. For the gelatin:PCL (G:PCL) solutions and tropoelastin:PCL (T:PCL) solutions, the feeding PTFE tubes were fed through a positively-charged translating stage on the same horizontal level as the target and above the target, respectively. All feeding PTFE tubes were connected to a 0.6 mm ID hollow stainless steel dispensing tips, which were all at a distance of 10 cm away from the target. The two dispensing tips alternatingly translated back and forth at a speed of 300 mm/sec along a total axial distance of 10 cm. The G:PCL and T:PCL solutions were dispensed at a rate of 100 and 30 µL/min, respectively. The electrospinning system included an EM-GSM gas shield module (IME Technologies, Netherlands), which was utilized to prevent the accumulation of biopolymer at both nozzles and stabilize the electrospinning streams for increased reproducibility. Additionally, an EM-ASM anti-static module (IME Technologies, Netherlands) was used to electrically neutralize any electric charge accumulated inside the electrospinning chamber, which played a role in minimizing non-specific fiber binding and increasing throughput yield and quality. A voltage difference of 15 kV was generated between both dispensing tips and a grounded rotating stainless

steel rod (1.55 mm OD) rotating at a speed of 300 RPM. The electrospinning chamber's temperature and relative humidity was controlled to be 25 ± 3 °C and 30 ± 2%, respectively. Polymeric solutions were dispensed to create electrospun cylindrical constructs for each protein:PCL ratio for both gelatin and tropoelastin (n=3 for each ratio, 18 total). All constructs were removed and placed in 0.5% (m/v) concentration of genipin (Wako Chemicals USA Inc, USA) in 200 proof ethanol for 24 hours at 37 °C for crosslinking. The constructs were rinsed with ethanol to remove the crosslinking agent and hydrated in 1X PBS. The electrospinning setup is shown in Figure 16.

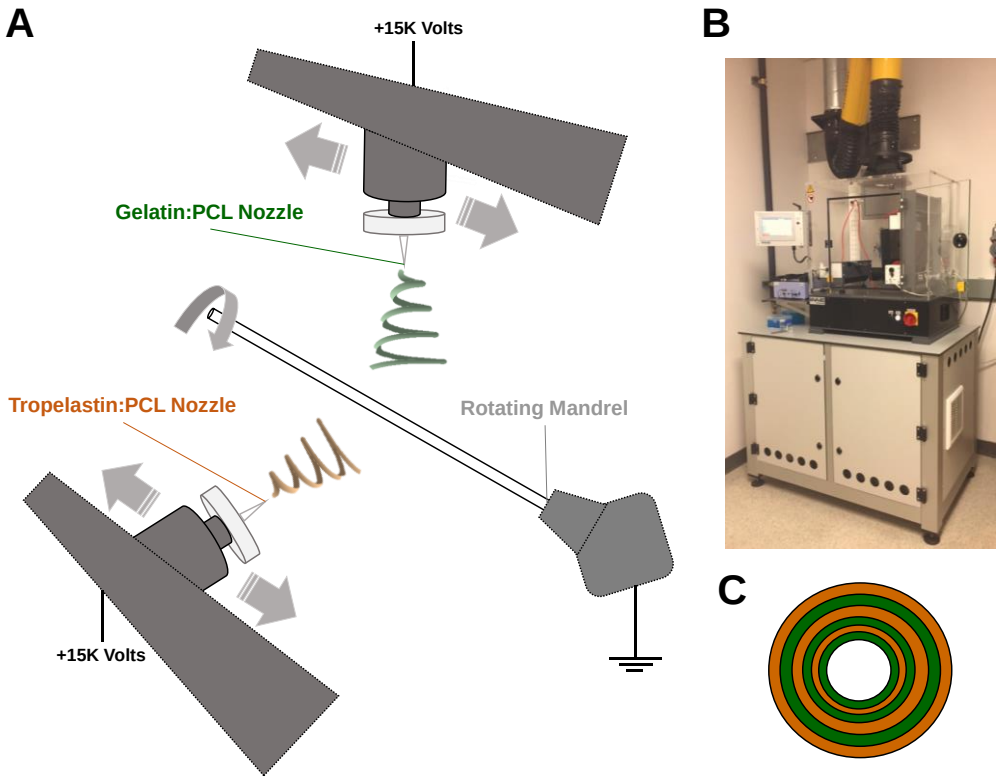

Figure 16. (A) Representation of the electrospinning setup with two translating positively charged dispensing nozzles and a rotating grounded mandrel (B) IME Technologies commercial electrospinning chamber (C) Graphical representation of construct cross-section showing the alternating G:PCL and T:PCL layers.

3.1.4 Sample Imaging and Thickness Measurements

Representative 0.5-cm samples were taken from each of the fabricated constructs and rat aorta samples and placed in plastic molds filled with Fisher Healthcare Tissue-Plus O.C.T. Compound (Thermo Fisher Scientific, USA). The molds were kept in a freezer at -20°C until frozen. Each sample was mounted in a Microm HM550 cryostat microtom (Thermo Fisher Scientific, USA), cryosectioned at a thickness of 40 μm and mounted onto glass slides. The glass slides were imaged using a Nikon 90i Eclipse fluorescence microscope (Nikon USA, USA). The autofluorescence signal of the fabricated constructs was collected through a Cy3 filter cube (excitation at 545 nm; emission at 610 nm), while the autofluorescence signal of the rat aorta media layer was collected using a FITC filter cube (excitation at 494 nm; emission at 518 nm). All samples were imaged using both a Nikon Plan APO 4x/0.2 [infinity]/- WD 12.7 objective (Nikon USA, USA) and a Nikon Plan Apo 20x/0.75 DIC N2 WD 1.0 objective (Nikon USA, USA). The NIS-Elements imaging software (Nikon USA, USA) was used to determine an average thickness measurement for each sample.

3.1.5 Tubular Biaxial Mechanical Testing

Mechanical testing of the fabricated characterization constructs and the rat aorta samples were performed using the in-house custom-made optomechanical biaxial tensile testing device (MOD), which has been previously described in section 2.2.1. For mechanical testing, the constructs were axially stretched to 1.2 at 0.05 mm/sec in 0.05 increments. At each axial stretch increment, the intraluminal pressure was slowly increased from 0 to 120 mmHg at an approximate rate of 4 mmHg/sec using the hydrostatic pressure from a refillable fluid saline bag filled with 1X PBS.

3.1.6 Constitutive Modeling and Stress-Strain Surface Averaging

The raw data generated by the MOD system and thickness data measured by fluorescence imaging was used to calculate strain and stress values for each sample in both axial and circumferential directions. Equations (2-1) through (2-7), previously mentioned in section 2.2.2, were used to calculate the axial and circumferential 2nd Piola Kirchhoff stresses and Green strains. Using the Fung strain energy Equation (2-8), the axial and circumferential 2nd Piola Kirchhoff stresses can be derived from the strain energy density using the differentiations shown by Equation (3-1)(3-1) and Equation (3-2), respectively[158]:

$$S_{zz}(E_{\theta\theta}, E_{zz}) = \frac{\partial W}{\partial E_{zz}} = c\ (\mathcal{A}_2 E_{zz} + 2\mathcal{A}_3 E_{\theta\theta})\ e^{Q} \tag{3-1}$$

$$S_{\theta\theta}(E_{\theta\theta}, E_{zz}) = \frac{\partial W}{\partial E_{\theta\theta}} = c\ (\mathcal{A}_1 E_{\theta\theta} + 2\mathcal{A}_3 E_{zz})\ e^{Q} \tag{3-2}$$

3.1.7 Stress-Strain Predictive Model

To develop an optimization scheme that would determine suitable fabrication parameters to produce a construct with desired mechanical properties, it was necessary to develop a predictive model that could produce stress-strain data for any protein:PCL ratio for both gelatin and tropoelastin between the ratios already mechanically characterized. The averaged axial and circumferential response surface data for all previously mentioned protein:PCL ratios (80:20, 50:50 and 20:80) for both gelatin and tropoelastin was used as part of a weighted sum interpolation method. Specifically, Lagrange interpolating polynomials [159] were used to interpolate between

stress-strain response data such that the actual characterized experimental data is recovered if protein percentage equals 20, 50, or 80 for both gelatin and tropoelastin. The interpolating second order polynomials expressions for the three datasets are shown in Equation (3-3) and Equation (3-4)(3-4):

$$S_{\theta\theta}(E_{\theta\theta}, E_{zz}, P) = N_1(P)S_{\theta\theta}^{(20)}(E_{\theta\theta}, E_{zz}) + N_2(P)S_{\theta\theta}^{(50)}(E_{\theta\theta}, E_{zz}) + N_3(P)S_{\theta\theta}^{(80)}(E_{\theta\theta}, E_{zz}) \quad (3\text{-}3)$$

$$S_{zz}(E_{\theta\theta}, E_{zz}, P) = N_1(P)S_{zz}^{(20)}(E_{\theta\theta}, E_{zz}) + N_2(P)S_{zz}^{(50)}(E_{\theta\theta}, E_{zz}) + N_3(P)S_{zz}^{(80)}(E_{\theta\theta}, E_{zz}) \quad (3\text{-}4)$$

where P is the protein percentage between 20 and 80, $S_{\theta\theta}(E_{\theta\theta}, E_{zz}, P)$, and $S_{zz}(E_{\theta\theta}, E_{zz}, P)$ are the circumferential and axial predicted stress-strain surface data for any protein percentage between 20 and 80%, respectively, $S_{\theta\theta}^{(20)}(E_{\theta\theta}, E_{zz})$, $S_{\theta\theta}^{(50)}(E_{\theta\theta}, E_{zz})$ and $S_{\theta\theta}^{(80)}(E_{\theta\theta}, E_{zz})$ are the circumferential stress-strain surface data for the 80:20, 50:50 and 20:80 protein:PCL ratios, respectively, $S_{zz}^{(20)}(E_{\theta\theta}, E_{zz})$, $S_{zz}^{(50)}(E_{\theta\theta}, E_{zz})$ and $S_{zz}^{(80)}(E_{\theta\theta}, E_{zz})$ are the axial stress-strain surface data for the 80:20, 50:50 and 20:80 protein:PCL, respectively, and $N_1(P)$, $N_2(P)$ and $N_3(P)$ are Lagrangian interpolating polynomial defined by Equation (3-5)(3-5), Equation (3-6) and Equation (3-7), respectively.

$$N_1(P) = \frac{(P-50)(P-80)}{(20-50)(20-80)} \quad (3\text{-}5)$$

$$N_2(P) = \frac{(P-20)(P-80)}{(50-20)(50-80)} \quad (3\text{-}6)$$

$$N_3(P) = \frac{(P-20)(P-50)}{(80-20)(80-50)} \tag{3-7}$$

For any value of P between 20 and 80, the Lagrangian interpolating polynomial calculate the appropriate weighted contribution of stress-strain data at 80:20, 50:50 and 20:80 for either protein. These equations were applied to both the G:PCL and T:PCL datasets to calculate axial and circumferential stress-strain datasets for each protein:PCL material separately. These predicted datasets were fit simultaneously to Equations (3-1) and Equation (3-2) to produce one set of Fung constitutive model constants for G:PCL and T:PCL at a specific biopolymer percentage for each that were used in the optimization scheme. The predictive model code is shown in Appendix A.

3.1.8 Optimization Routine

Our research group previously developed a finite element optimization scheme that predicted the thickness and crosslinking time of glutaraldehyde electrospun single layered gelatin/fibrinogen constructs that were compliance-matched to porcine coronary arteries [157]. This optimization routine was adapted (Appendix B) to predict the thickness and protein:PCL ratios of alternating layered constructs to match the geometry and compliance of rat aorta. Briefly, Matlab (MathWorks Inc, USA) code was used to generate Abaqus FEA (Dassault Systemes Simulia, France) input files for a four-noded, reduced-integration, axisymmetric element model using a hybrid formulation (Appendix C). The mesh geometry consisted of a user-defined number of alternating G:PCL and T:PCL layers. The element regions associated with the G:PCL layers and the T:PCL layers were assigned appropriate material constants generated by the previously mentioned predictive model. ABAQUS then simulated the intraluminal pressurization from 0 to 120 mmHg and the outer

diameter measurement was extracted at 70 and 120 mmHg, which was used to calculate the simulated compliance value per Equation (2-9). The open fit design parameters in the optimization scheme included the thicknesses and the protein:PCL ratios for each of the G:PCL and T:PCL layers. The fixed parameters included the total number of layers, construct inner diameter, and total thickness. The rat aorta inner diameter and media layer thickness values were averaged and used as the target inner diameter and thickness values for the optimized grafts, respectively. Additionally, the average observed number of layers of elastin in rat aorta was chosen as the fixed number of alternating layers for all optimized compliance values. A construct total thickness computational tolerance of 20% was deemed acceptable to allow for flexibility in the optimization scheme. The MATLAB bounded optimization function (fminsearchbnd) iterated while changing the open design parameters until the difference between the predicted compliance value from the Abaqus FEA simulation and the target compliance value fell within less than 1% of the target compliance. A summary of the optimization scheme is shown in Figure 17.

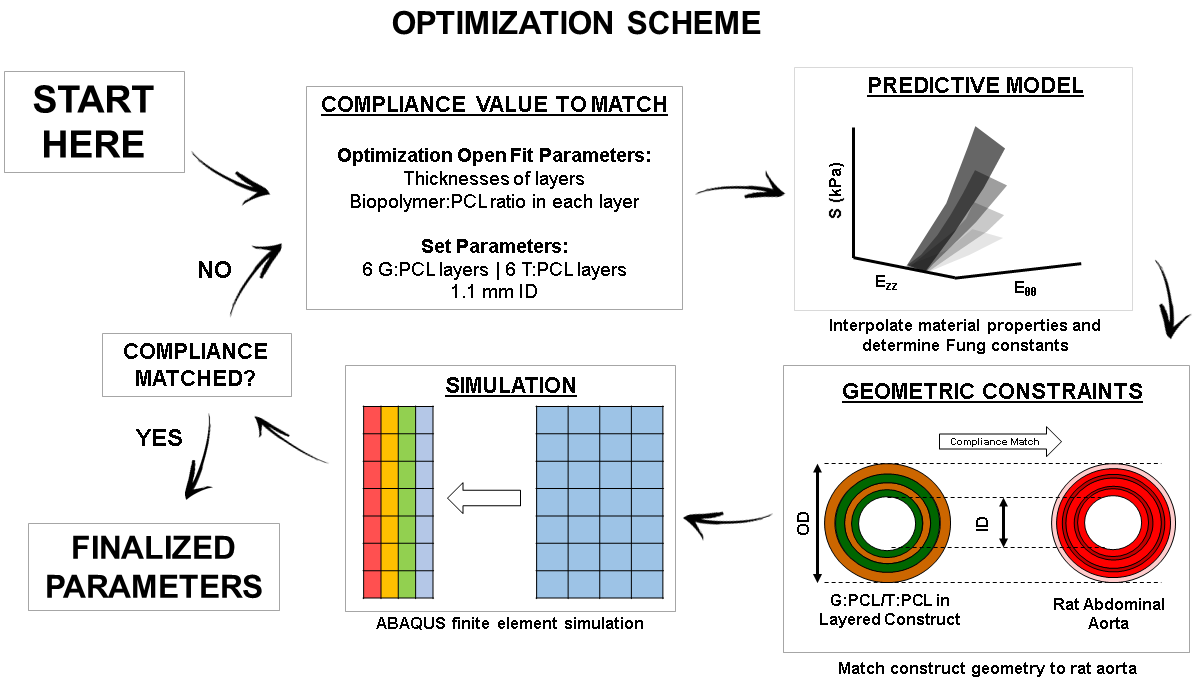

Figure 17. A diagram illustrating the scheme used in this study.

3.1.9 Compliance Matching and Optimization Model Validation

Multiple compliance targets were chosen to demonstrate the flexibility of our model to compliance match to a wide range of values. The measured rat aorta compliances were averaged and the optimized grafts with this compliance were referred to as isocompliant. The optimized grafts targeted to compliance match the average, the upper limit (one standard deviation added to the average), and lower limit (one standard deviation subtracted from the average) compliance values were referred to as isocompliant, hypercompliant, and hypocompliant optimized grafts, respectively. The optimization scheme was run to determine the design parameters necessary to create multilayered constructs that compliance matched all three targets. The optimization results were used to fabricate optimized grafts for all experimental groups. To match the target layer

thicknesses, the thickness data from the characterization constructs was used to estimate the appropriate volumetric flow rate that would result in the appropriate G:PCL and T:PCL layer thicknesses. To evaluate the accuracy of experimental individual layer thicknesses, cross-sections of the fabricated grafts were imaged to determine the individual thickness of each G:PCL and T:PCL layer. The relative error of individual layer thicknesses according to the Equation (3-8)

$$\%\, relative\ error = \left| \frac{target\ thickness - actual\ thickness}{target\ thickness} \right| \tag{3-8}$$

The individual rat aorta thicknesses were subtracted from the outer diameter values extracted from the MOD experiments. Compliance values and Fung constitutive model constants were determined for all optimized grafts, for which stress-strain response surfaces were generated.

3.1.10 Statistical Analysis

All values are presented as the average ± standard deviation unless otherwise specified. Two-sample two-tailed t-tests were conducted comparing the inner diameters and total thickness of optimized grafts to those of rat aorta. One sample two-tailed t-tests were conducted comparing the compliance of optimized grafts to their respective target compliance values. A Bonferroni correction was applied to the *p*-values of comparative statistical tests to account for familywise error. For all statistical tests, a critical p-value of 0.05 was considered significant.

3.2 RESULTS

3.2.1 Material Characterization

The G:PCL characterization constructs (80G:20PCL, 50G:50PCL and 20G:80PCL) and the T:PCL characterization constructs (80T:20PCL, 50T:50PCL and 20T:80PCL) were mechanically characterized and the Fung constitutive model constants, $\mathcal{A}_1/\mathcal{A}_2$ (measure of anisotropy) and R^2 values are shown in Table 2.

3.2.2 Stress-Strain Predictive Model

For both gelatin and tropoelastin, the developed predictive model was used to interpolate circumferential and axial stress-strain data for any ratio between 80:20 and 20:80. Predicted circumferential and axial stress-strain response surfaces for the G:PCL and T:PCL ratios are shown in Figure 18 and Figure 19, respectively.

3.2.3 Rat Aorta and Optimized Graft Characterization

To validate the finite element model and the predictive model, both were used to predict the compliance of the characterization constructs previously mentioned using the respective composition and thickness measurements. Paired t-tests were conducted to determine significant differences between the experimental and model compliance values. These comparisons are shown in Figure 20.

Table 2. Fung strain energy equation constants, $\mathcal{A}_2/\mathcal{A}_1$ values, and R^2 values for the average, upper and lower limit dataset for the G:PCL characterization constructs (80G:20PCL, 50G:50PCL and 20G:80PCL) and the T:PCL characterization constructs (80T:20PCL, 50T:50PCL and 20T:80PCL). R^2 values compare the Fung equation surface plots to the averaged surface data for all three replicates for the respective experimental group

Group	Dataset	c (MPa)	$\mathcal{A}_1$	$\mathcal{A}_2$	$\mathcal{A}_3$	$\mathcal{A}_2/\mathcal{A}_1$	R^2
20G:80PCL	Upper Limit	77.9	0.051	0.26	0.044	5.2	0.99
	Average	146.9	0.020	0.12	0.016	6.1	0.99
	Lower Limit	14.1	0.122	1.01	0.088	8.3	0.99
50G:50PCL	Upper Limit	93.7	0.012	0.065	0.009	5.6	0.98
	Average	21.6	0.044	0.22	0.034	4.9	0.98
	Lower Limit	72.5	0.011	0.045	0.009	4.0	0.96
80G:20PCL	Upper Limit	70.9	0.003	0.027	0.001	9.5	0.98
	Average	1.3	0.119	1.063	0.057	9.0	0.98
	Lower Limit	0.2	0.502	3.95	0.23	8.0	0.97
20T:80PCL	Upper Limit	302.2	0.024	0.063	0.015	2.6	0.81
	Average	3.3	1.621	4.79	1.034	3.0	0.81
	Lower Limit	0.3	9.208	29.434	5.723	3.2	0.92
50T:50PCL	Upper Limit	57.2	0.073	0.260	0.047	3.6	0.80
	Average	4.5	0.834	2.834	0.545	3.4	0.80
	Lower Limit	0.8	3.982	11.744	2.589	3.0	0.87
80T:20PCL	Upper Limit	319.7	0.004	0.021	0.002	5.1	0.99
	Average	13.2	0.092	0.461	0.052	5.0	0.99
	Lower Limit	272.2	0.004	0.021	0.002	5.0	0.99

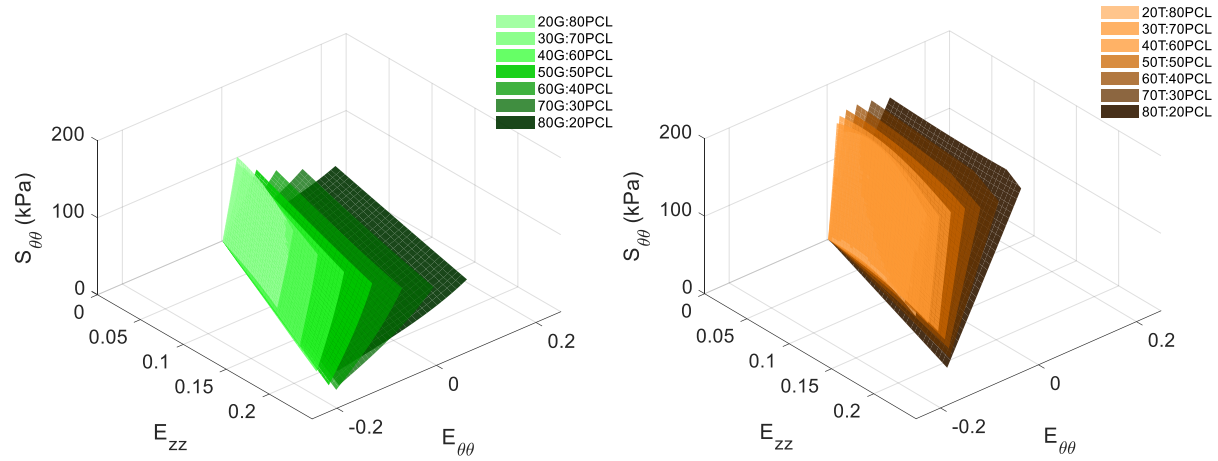

Figure 18. Predicted circumferential stress-strain response surfaces for (left) G:PCL ratios and (right) T:PCL ratios of 80:20, 70:30, 60:40, 50:50, 40:60, 30:70 and 20:80. The T:PCL materials are qualitatively stiffer than the G:PCL materials at the same protein:PCL ratios.

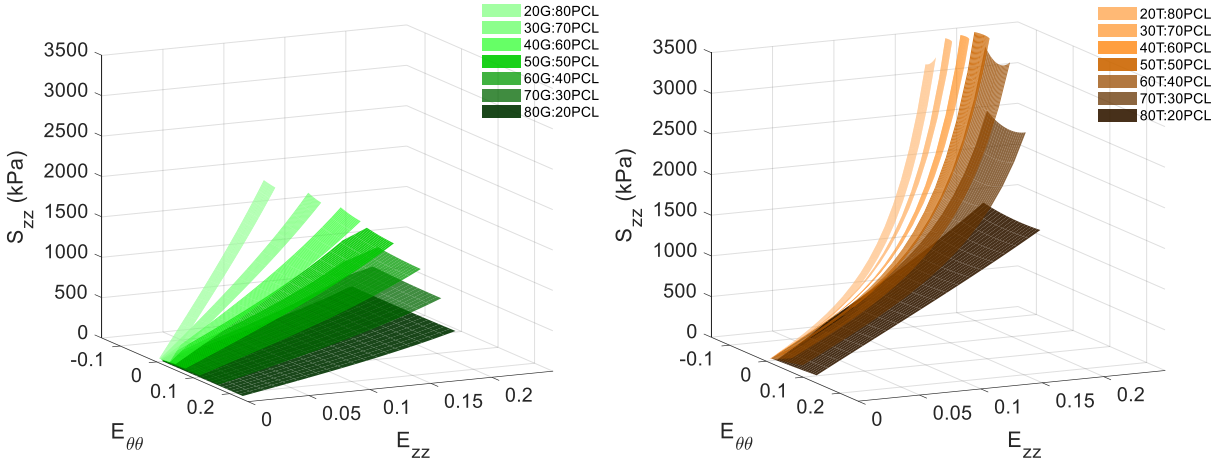

Figure 19. Predicted axial stress-strain response surfaces for (left) G:PCL ratios and (right) T:PCL ratios of 80:20, 70:30, 60:40, 50:50, 40:60, 30:70 and 20:80. The T:PCL materials are qualitatively stiffer than the G:PCL materials at the same protein:PCL ratios.

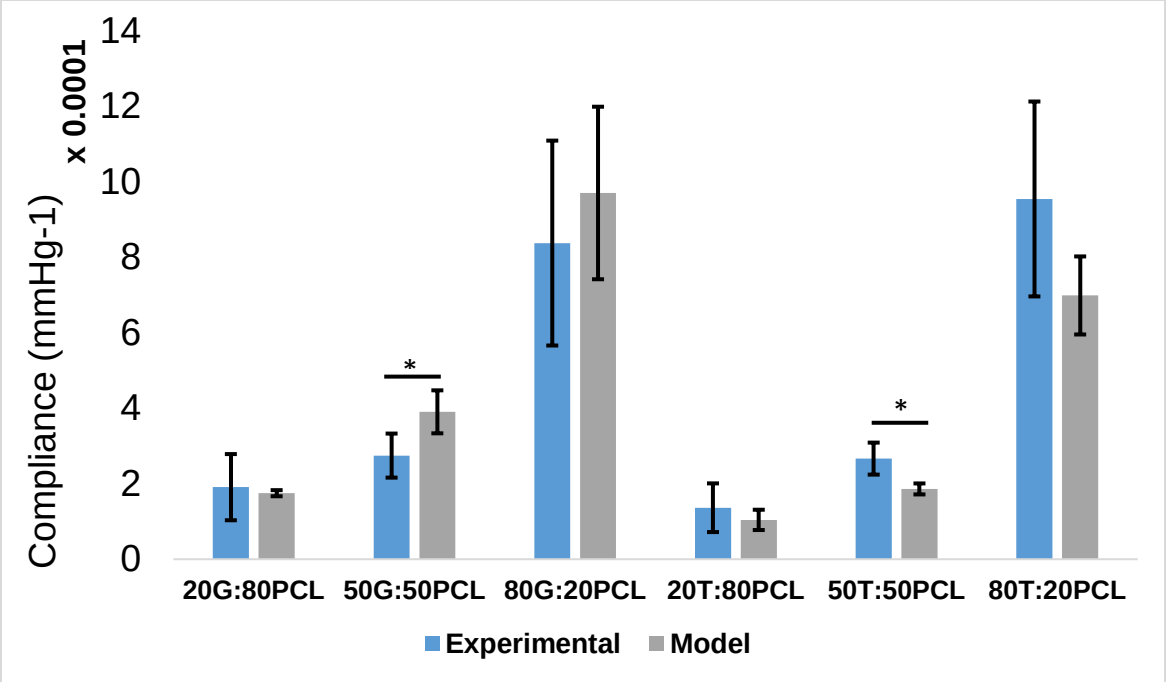

Figure 20. Compliance comparison of experimental values and model values for all characterization constructs. A paired t-test was run to compare reach individual replicate to its simulated compliance using the predictive model. Astriesk indicates p-value < 0.05. The results show that the experimental compliance of the 20:80 and 80:20 protein:PCL ratio for both gelatin and tropoelastin were not statistically different than their model compliance values. The experimental compliance for the 50:50 protein:PCL ratios for gelatin and tropoelastin were statistically significant than their model compliance values.

3.2.4 Rat Aorta and Optimized Graft Characterization

The average outer diameters of the rat aortas (n=13) were determined to be 1.28 ± 0.11 mm. The average rat aorta media layer thickness was determined to be 55 ± 7 microns. The individual rat aorta thicknesses were subtracted from the outer diameter values and the average inner diameter was determined to be 1.17 ± 0.15 mm. To match the inner diameter of optimized grafts to the inner diameter of rat aorta, the electrospinning mandrel target was chosen to have an outer diameter of about 1.17 mm. To qualitatively match the number of elastin/collagen layers of rat aorta, the total

number of G:PCL and T:PCL layers was set at 12 layers (6 each). Using the MOD system, the average compliance value of the rat aorta was determined to be 0.000568 ± 0.000318 $mmHg^{-1}$. Based on this compliance range, the target compliance values for the hypocompliant, isocompliant and hypercompliant optimized grafts were set at 0.000256, 0.000568 and 0.000880 $mmHg^{-1}$, respectively. The optimization scheme was utilized and the resulting G:PCL ratios, T:PCL ratios and individual layer thicknesses for all optimized experimental groups are shown in Table **3**, which were used to fabricate all optimized grafts.

Table 3. Optimization scheme predicted results for G:PCL and T:PCL layer ratios and thicknesses for individual layers for all optimized graft groups.

Optimized Experimental Group	**Predicted G:PCL Layer Ratio**	**Predicted T:PCL Layer Ratio**	**Predicted Individual Layer Thickness (microns)**												
			G1	**T1**	**G2**	**T2**	**G3**	**T3**	**G4**	**T4**	**G5**	**T5**	**G6**	**T6**	**Total**
Hypercompliant	75:25	68:32	7	5	7	5	8	5	8	5	7	5	7	5	74
Isocompliant	71:29	48:52	6	5	5	5	6	5	7	5	6	5	7	5	67
Hypocompliant	35:65	28:72	5	5	9	5	9	5	9	5	8	5	9	5	79

Fluorescence images of the cross-sections of fabricated optimized grafts were used to determine the actual thickness values, which were compared to the optimized target values. The average G:PCL layer thickness relative error (%) for the hypocompliant (n=3), isocompliant (n=3), and hypercompliant (n=3) were 30.0 ± 7.3%, 12.7 ± 8.7% and 27.15 ± 8.7%, respectively. The average T:PCL layer thickness relative error (%) for the hypocompliant, isocompliant, and hypercompliant were 16.0 ± 8.8%, 15.6 ± 8.5% and 33.2 ± 5.7%, respectively. The average inner diameter values for the hypocompliant, isocompliant, and hypercompliant grafts were 1.04 ± 0.01

mm, 0.86 ± 0.07 mm, 0.92 ± 0.05 mm, respectively. The inner diameters of the isocompliant and hypercompliant were significantly lower than that of rat aorta (p-value = 0.002 and 0.001, respectively), whereas the inner diameter values of hypocompliant grafts were not statistically different than that of rat aorta (p-value = 0.25). The average wall thickness values for the hypocompliant grafts, isocompliant grafts, hypercompliant grafts were 57 ± 4 microns, 59 ± 8 microns and 56 ± 6 microns, respectively. The total wall thickness of the hypocompliant, isocompliant, and hypercompliant grafts were not statistically different than that of rat aorta (p-value > 0.99 for all). Fluorescence images of cross-sections of the optimized grafts and graphs demonstrating the inner diameter values and thickness values of the optimized grafts are shown compared to rat aorta in Figure 21. Additionally, a detailed image comparison of an optimized construct to rat aorta is shown in Figure 22.

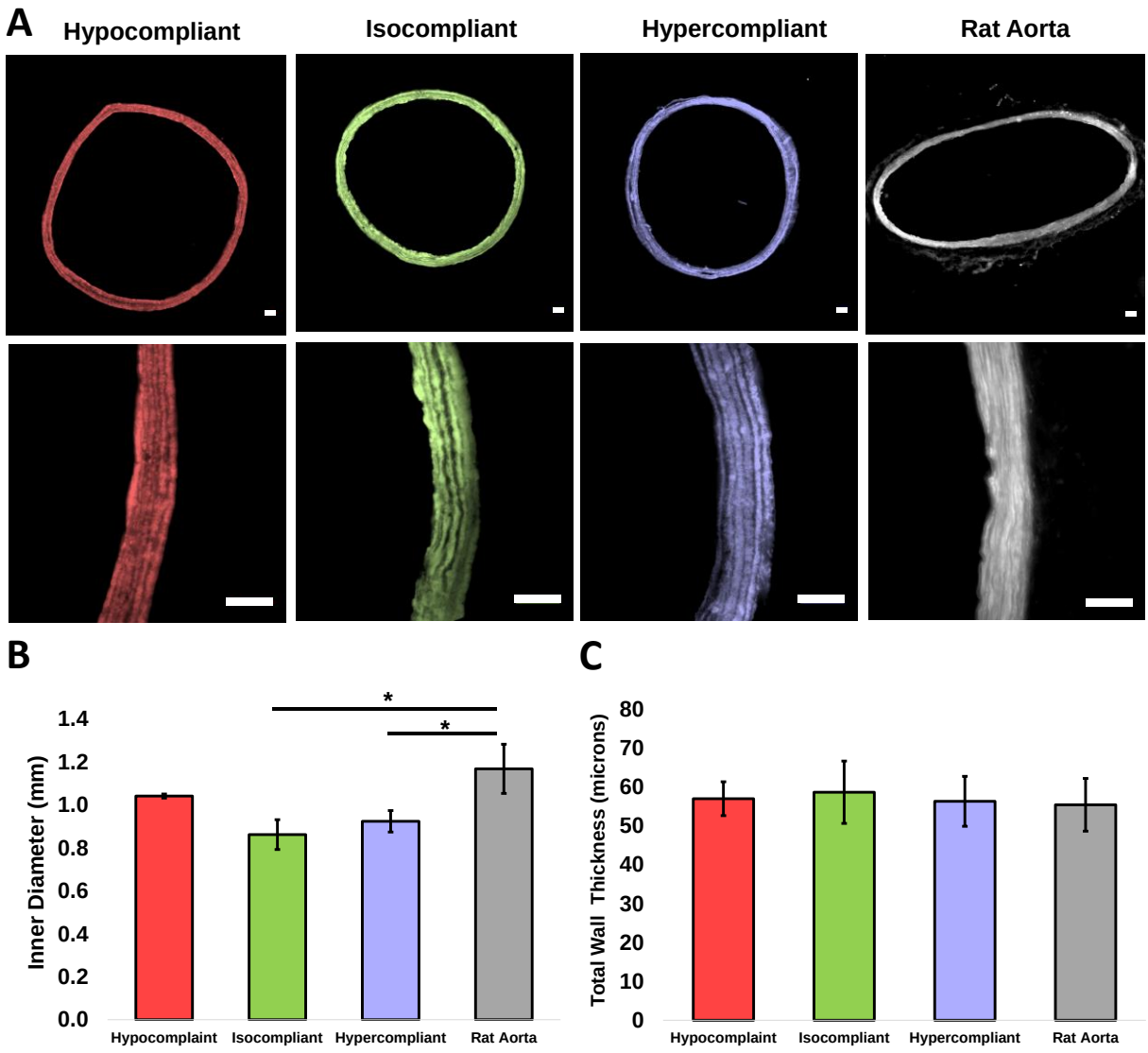

Figure 21. (A) 4X and 20X fluorescence images of representative samples of the hypocompliant, isocompliant, and hypercompliant optimized grafts and rat aorta. Scale bar indicates 50 microns for all images. (B) Inner diameter and (C) total thickness of the hypocompliant, isocompliant, and hypercompliant optimized grafts compared to rat aorta. Error bars indicate one standard deviation. Asterisk indicates statistical significance of difference compared to rat aorta using two-sample two-tailed t-test (p-value<0.05)

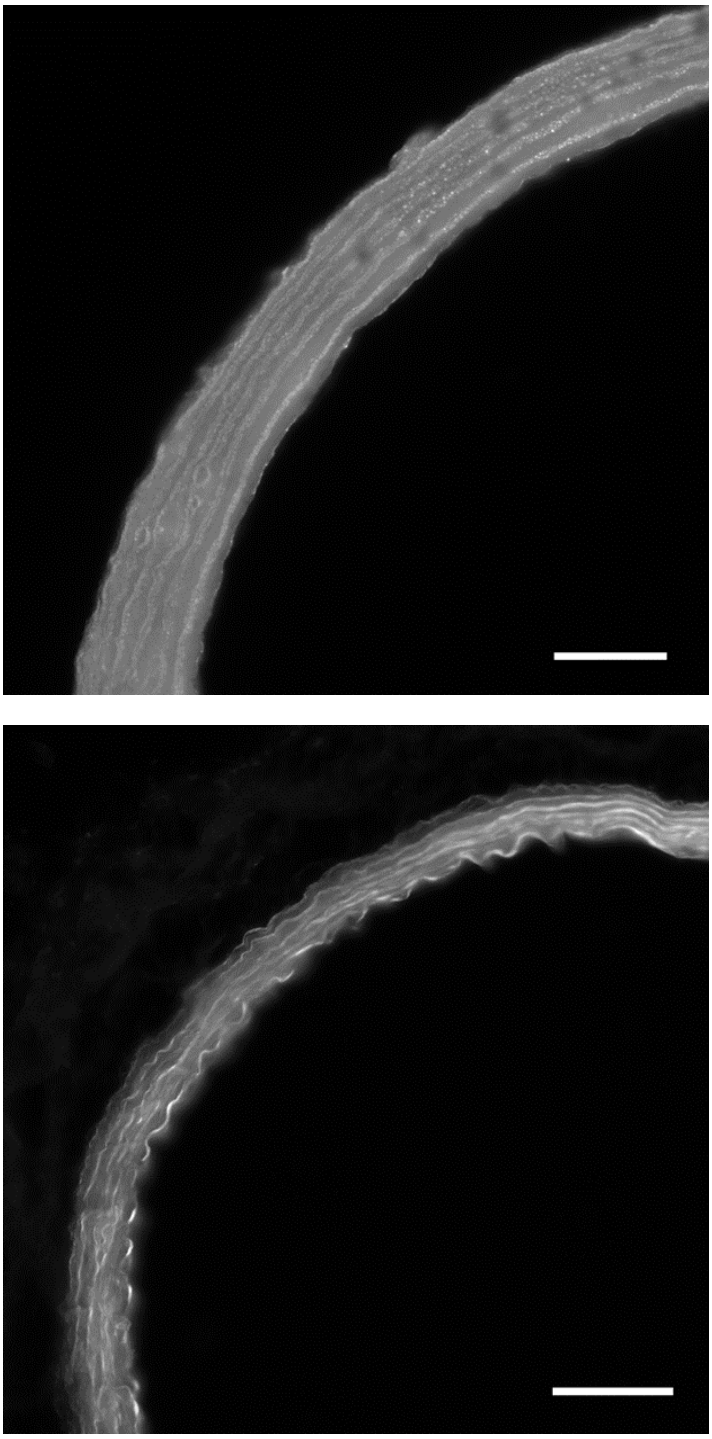

Figure 22. Detailed fluorescence image comparison of optimized graft (top) compared to rat aorta (below).Please note the similarity between the distinct layers of G:PCL/T:PCL layers (top) and collagen/elastin (bottom). Scale bar represents 100 microns.

3.2.5 Optimized Compliance and Mechanical Characterization

The compliance values of the hypercompliant optimized grafts (0.0010 ± 0.00020 $mmHg^{-1}$) and isocompliant optimized grafts (0.00056 ± 0.000051 $mmHg^{-1}$) were not statistically different than their respective target compliances (p-value = 0.37 and 0.89, respectively). The compliance values of the hypocompliant optimized grafts (0.00017 ± 0.000055 mmHg-1) was statistically different than their respective target compliance (p-value = 0.047). The average compliance values are shown in Figure 23. The Fung equation constants, R^2 values and $\mathcal{A}_2/\mathcal{A}_1$ values for the upper limit, average and lower limit dataset for each of these groups are shown in Table 4. The average circumferential and axial stress-strain Fung-fit responses surfaces for the hypocompliant, isocompliant, and hypercompliant optimized grafts (n=3 for each) and rat aorta (n=8) are shown in Figure 24 and Figure 25, respectively.

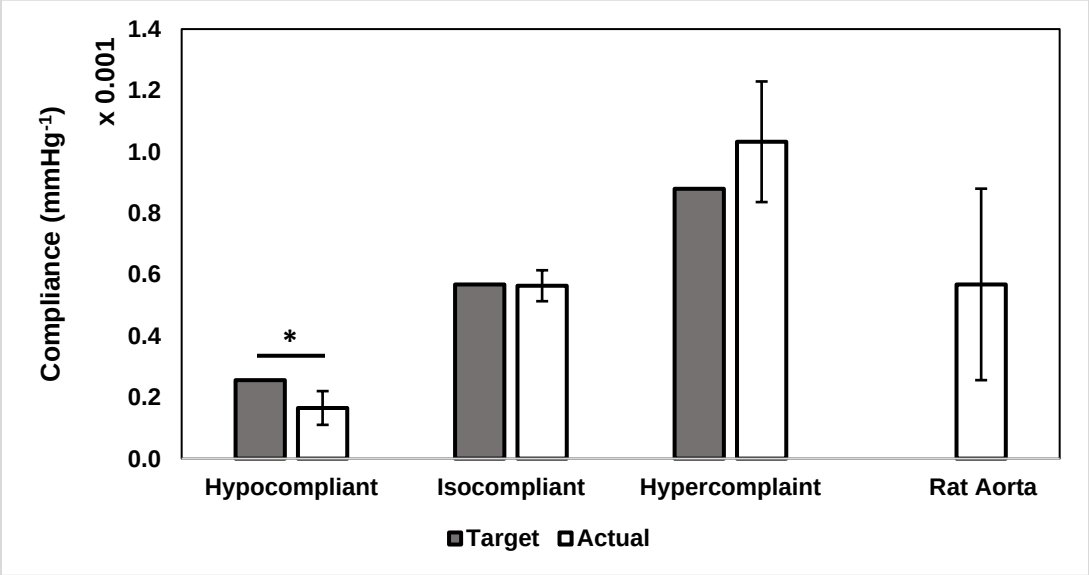

Figure 23. Target and actual compliance values of the hypocompliant, isocompliant, and hypercompliant optimized grafts compared to rat aorta compliance values. Error bars indicate one standard deviation. Asterisk indicates significant difference to target compliance value using one sample two-tailed t-test (*p*-value < 0.05).

Table 4. Fung strain energy equation constants, $\mathcal{A}_2/\mathcal{A}_1$ values, and R^2 values for the average, upper, and lower limit dataset for the hypocompliant, isocompliant, and hypercompliant optimized grafts and rat aorta. R^2 values compare the Fung equation surface plots to the averaged surface data for all three replicates for the respective experimental group.

Group	Dataset	c (MPa)	$\mathcal{A}_1$	$\mathcal{A}_2$	$\mathcal{A}_3$	$\mathcal{A}_2/\mathcal{A}_1$	R^2
Hypocompliant	Upper Limit	188.21	0.046	0.17	0.029	3.7	0.99
	Average	149.40	0.048	0.19	0.029	4.0	0.99
	Lower Limit	122.98	0.047	0.21	0.027	4.5	0.99
Isocompliant	Upper Limit	1.35	1.033	9.62	0.487	9.3	0.97
	Average	1.55	0.865	7.92	0.399	9.2	0.96
	Lower Limit	2.23	0.587	5.31	0.264	9.1	0.92
Hypercompliant	Upper Limit	154.93	0.011	0.062	0.006	6.0	0.86
	Average	64.34	0.024	0.14	0.014	5.8	0.85
	Lower Limit	74.92	0.020	0.12	0.011	5.9	0.83
Rat Aorta	Upper Limit	136.08	0.011	0.038	0.005	3.4	0.98
	Average	1.10	0.850	2.66	0.371	3.1	0.98
	Lower Limit	0.005	31.805	50.11	9.433	1.6	0.90

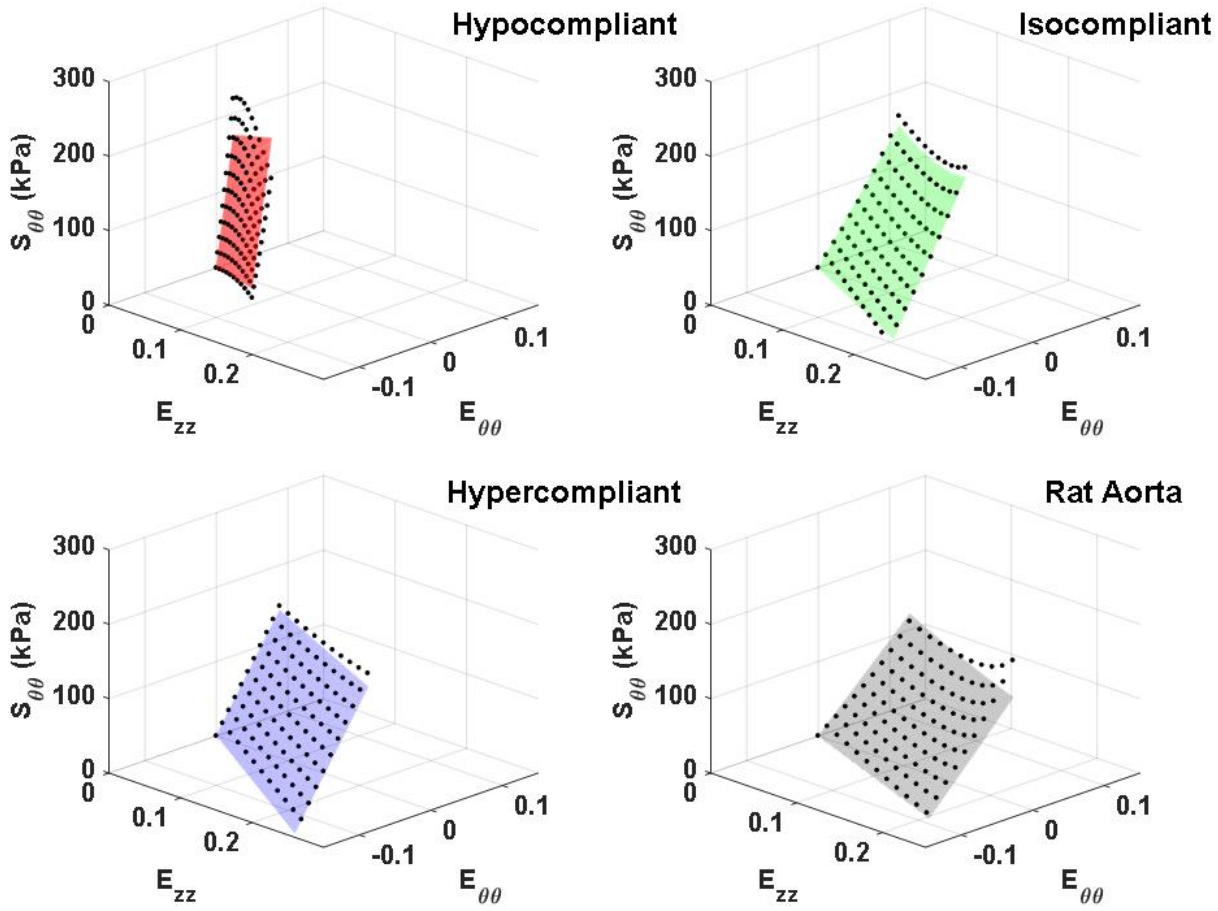

Figure 24. Average circumferential stress-strain Fung fitted response surface plots for the hypocompliant, isocompliant, and hypercompliant optimized grafts as well as for rat aorta. Averaged data points from all replicates are displayed for fit evaluation and visualization. Please note that the isocompliant grafts and hypercompliant grafts response surfaces were qualitatively similar to that of rat aortas, whereas the hypocompliant grafts were noticeably different.

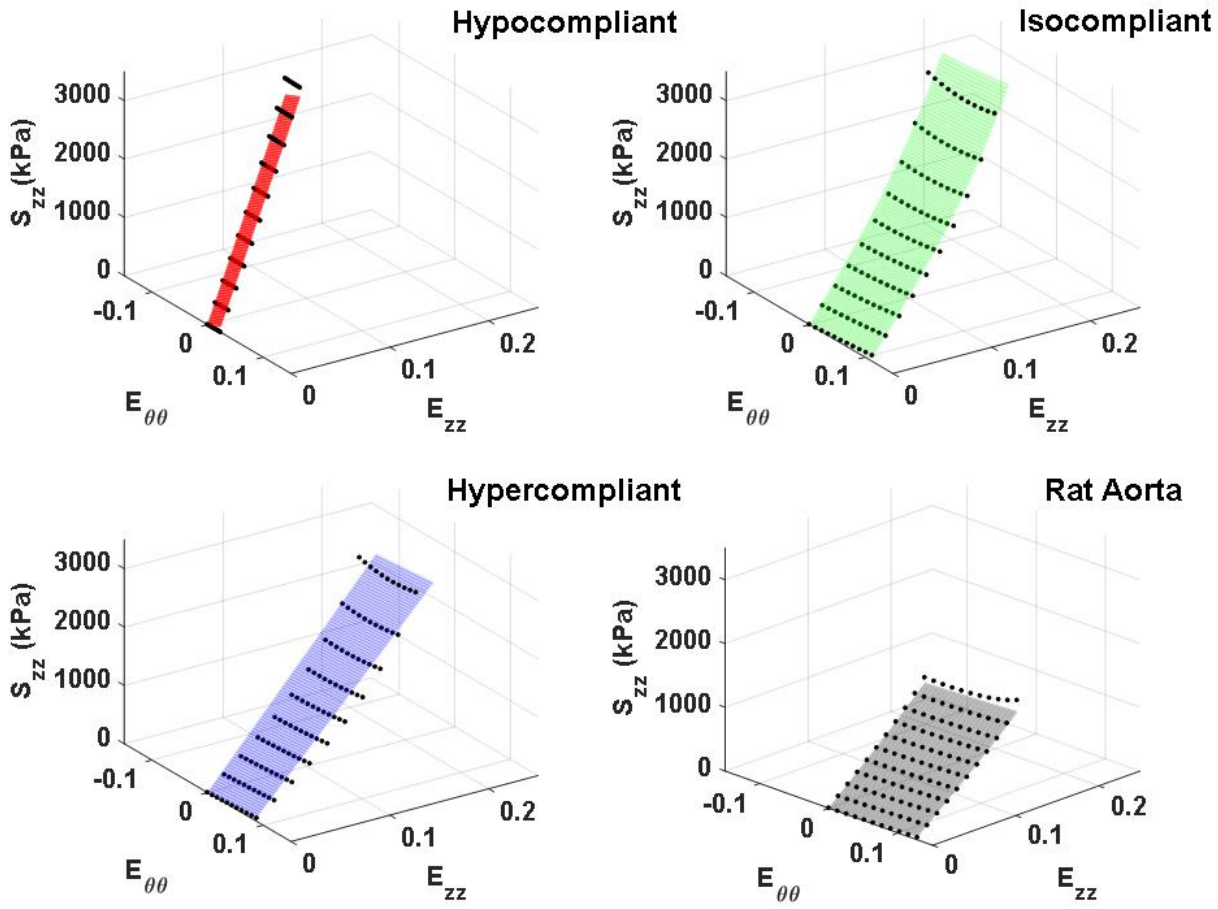

Figure 25. Average axial stress-strain Fung-fitted response surface plots for the hypocompliant, isocompliant, and hypercompliant optimized grafts as well as for rat aorta. Averaged data points from all replicates are displayed for fit evaluation and visualization. Please note that all optimized grafts were qualitatively stiffer in the axial direction compared to the rat aorta.

3.3 DISCUSSION

Electrospun cylindrical hybrid constructs comprised of various G:PCL and T:PCL ratios were mechanically characterized. The mechanical data was used to develop a stress-strain predictive model, which could predict the mechanical properties of any ratio G:PCL and T:PCL between 80:20 and 20:80 using Lagrangian polynomial interpolation. The predictive model was used as

part of an optimization scheme to determine the appropriate protein:PCL ratios and thicknesses, which were then used to fabricate G:PCL/T:PCL alternating layered constructs that could compliance match to rat aorta. The alternating two-nozzle electrospinning method produced optimized grafts with distinct G:PCL and T:PCL layers for all three target compliances (Figure **21**). These optimized grafts had G:PCL and T:PCL layers with thickness percentage relative errors averages of less than 30.0% and 33.2%, respectively. Mechanical characterization of the optimized grafts showed that the optimization scheme was successful at compliance-matching grafts with high gelatin and tropoelastin content. Specifically, the optimization model successfully determined the appropriate protein:PCL ratios and layer thickness configurations to properly match the compliance of hypercompliant (75G:25PCL and 68T:32PCL) and isocompliant (71G:29PCL and 48T:52PCL) grafts. However, the experimental results showed that the optimization scheme overestimated the compliance of the hypocompliant grafts, which had lower gelatin and tropoelastin content (35G:65PCL and 28T:72PCL).

As expected, the mechanical data generated from the pure G:PCL and T:PCL characterization constructs, and consequently the predictive model, showed that as the gelatin and tropoelastin content increases the material became less stiff and exhibited higher deformability. Our laboratory group had previously demonstrated in preliminary experiments (Figure 4) that electrospinning cylindrical constructs composed of a blend of tropoelastin and gelatin allowed for greater elasticity, deformability, and compliance compared to construct made of exclusively gelatin. We had expected that any T:PCL ratio would be less stiff than its counterpart for G:PCL and that tropoelastin would be used to help tune the optimized grafts to become more compliant. However, T:PCL materials were qualitatively stiffer than G:PCL of the same protein:PCL ratio in both circumferential and axial directions. This may be due to a difference in crosslinking

mechanism between glutaraldehyde and genipin [160, 161]. Whereas our previous crosslinking method consisted of exposing constructs to glutaraldehyde vapor phase, our genipin crosslinking procedure involved submerging our electrospun constructs in a 0.5% genipin solution in ethanol. Since a portion of the tropoelastin cake is comprised of PEG, it may be possible that the electrospun PEG solution dissolved in the ethanol. This may have resulted in a higher degree of crosslinking on T:PCL materials, due to an increase in crosslinking site availability, compared to the G:PCL materials which did not contain PEG.

Another explanation of this tropoelastin behavioral discrepancy may be due to how differently genipin interacts with gelatin compared to tropoelastin. It may be necessary to investigate other crosslinking non-toxic methods that could better utilize the elastic nature of tropoelastin. It is important to note that for both gelatin and tropoelastin, as protein content increased so did the anisotropic behavior as indicated by $\mathcal{A}_2/\mathcal{A}_1$ values for both the G:PCL and T:PCL materials. This could be due to a higher diversity of fiber diameters in materials with higher protein content. Moreover, the inner diameter of the optimized grafts with higher protein content were lower compared to those with lower protein content. Although all optimized grafts were electrospun on the same mandrel with a fixed outer diameter to match rat aorta inner diameter, only the hypocompliant optimized graft had an inner diameter not statistically different than that of rat aorta. The decrease in inner diameter of the hypercompliant and isocompliant could be attributed to a compressive effect of the genipin crosslinking, which only affected the protein component of the graft. Mandrels with larger outer diameters may be necessary in order match inner diameter of rat aorta for optimized grafts with higher percentages of protein to account for the crosslinking shrinking effect.

In our previous work, we fabricated and characterized glutaraldehyde-crosslinked gelatin/fibrinogen constructs, which were limited in deformability and mechanical integrity. Our current study added PCL to the graft composition, allowing axial strains beyond the 0.17 limit exhibited by some gelatin/fibrinogen grafts previously fabricated [78]. This was achieved while still compliance matching to the different compliance range values of rat aorta. It should also be noted that most values of the anisotropy indicator $\mathcal{A}_2/\mathcal{A}_1$ for the protein:PCL grafts in our current study increased compared to that of the previous study. Few researchers have reported fabricated layered constructs compared to a biological native sample. Huang et al. created a triple-layered vascular graft composed of two synthetic polymers (PCL and polyethylene glycol) using a combination of E-Jet 3D printing and electrospinning [162]. The authors found that their layered grafts, which had thicknesses on the order of 700 microns, had higher burst strength and tensile strength to abdominal aortas from Sprague Dawley rats. While the study by Huang et al. did not report on compliance measures, it is unlikely that their grafts compliance matched rat aorta, because of the observed high thicknesses and synthetic polymer composition. Yu et al. developed a biomimetic hybrid small-diameter vascular graft at different ratios of polyurethane and fibroin. Similar to our study, they demonstrated that the mechanical properties (Young's Modulus and Ultimate Strength) could be changed by varying the ratio of the synthetic polymer to the natural polymer. However, the focus of the study was mainly on the suitability of the graft for endothelialization and did not compare the mechanical properties of the graft to native tissue. In contrast to these studies, the thickness of our optimized grafts were not statistically different from that of our target biological sample, and we have demonstrated that at least two of our optimized graft experimental groups compliance matched their target compliance value. However, future studies are necessary to determine the suitability of the graft for endothelialization and cell culture.

Few researchers have attempted to compliance match vascular grafts to native tissue. Nezarati et al. fabricated electrospun different poly(carbonate urethanes) and evaluated the effect of changing thickness and microstructure on the compliance of the constructs with inner diameters and thicknesses on the order of 5 mm and 400 microns, respectively [163]. The study attempted to tune the compliance of their synthetic constructs (0.0006 ± 0.00006 $mmHg^{-1}$) to exceed that of human saphenous vein (0.00044 ± 0.00008 $mmHg^{-1}$) mechanically characterized in other literature [164]. Soletti et al. fabricated a bilayered vascular graft using both electrospinning and thermally induced phase separation and were compared mechanically to native human saphenous veins (hSV) and porcine internal mammary arteries (IMAs) [124]. The compliance values of the grafts were measured to be 0.00046 ± 0.00005 $mmHg^{-1}$ and were considered similar to both hSV and porcine IMAs without matching geometric dimensions of either. These compliance values were similar to those of the isocompliant optimized grafts in our study, which measured at 0.00056 ± 0.000051 $mmHg^{-1}$. However, the geometrical dimensions of these grafts (4.7 mm ID with 490 microns thickness) were larger than the small diameter rat aorta, as they were meant for the larger dimensions of hSV and porcine IMAs. In another study, Soletti et al. fabricated electrospun synthetic grafts with inner diameters and thicknesses similar to that of Lewis rat abdominal aorta [165]. However, in this case the compliance values of their synthetic grafts were significantly lower than that of measured Lewis rat aorta. This mismatch shown in the literature between native tissue and grafts, in regards to geometry and compliance, highlights the importance and significance of having the ability to tune compliance by adding natural polymers while also controlling geometrical parameters, which was successfully demonstrated by our optimization scheme as presented in this study. There are few studies that have also electrospun recombinant human tropoelastin [70, 95, 119]. In one study, Wise et al. fabricated an electrospun bilayered

construct by sequentially delivering tropoelastin and tropoelastin:PCL [119]. Similar to our study, Wise et al. added tropoelastin to PCL to fabricate cylindrical constructs and determined mechanical properties like compliance, burst pressure and elastic modulus. Their constructs had two layers, with only one outer hybrid layer of tropoelastin:PCL at one ratio of 80:20 with a thickness and inner diameter on the order of 300 microns and 3 mm, respectively. The compliance value of their construct was on the order 0.0008 $mmHg^{-1}$, which they demonstrated was not statistically different than that of human IMAs but was different from that of human saphenous vein. Their study did not show how changing the T:PCL ratio can tune the compliance of their constructs to match different compliance ranges nor did they perform biaxial mechanical characterization and constitutive modelling. They were, however, able to show that these layered tropoelastin/tropoelastin:PCL grafts had the mechanical integrity and biocompatibility to be successfully implanted in an animal model for one month. Although these grafts were crosslinked with glutaraldehyde instead of genipin, these results exhibit the suitability of our materials to be used for a functional vascular graft in future studies.

Some studies in the literature have utilized computational methods to characterize vascular constructs. A study by Jankowska et al. used constitutive modelling to characterize the mechanical behavior of human coronary artery using a Holzapfel constitutive model at different stages of atherosclerosis [166], which could prove useful in developing finite element models for vascular grafts with the goal of targeting suitable mechanical properties. There are few examples in the literature of studies that utilize computational methods to predict vascular graft compliance. Szafron et al. developed and performed a parametric computational study of different parameters, like thickness and shear modulus, on the compliance of a bilayered cylindrical construct [167]. This study did not present experimental validation of their findings. However, it did provide a wide

range of insights into the parameters important to vascular graft design. A study by Castillo-Cruz et al. investigated the suitability of an analytical expression to determine the compliance of a cylindrical construct made of Tecoflex (polyurethane). Their analytical solution was successful at compliance prediction based solely on the elastic modulus and Poisson's ratio of the polymer material, which was determined through uniaxial tensile and compressive tests of the materials [168]. Castillo-Cruz et al. used finite element analysis to predict compliance using a four-noded axisymmetric model, similar to the finite element technique presented in the current study [168]. Although the material was modelled using a simple isotropic linear elastic model, the finite element model was validated by predicting the compliance values measured experimentally. However, their study was limited to the prediction of the behavior of one isotropic non-fibrous synthetic material. Our approach adds to the current state of the art by combining a computational predictive model with finite element-based optimization, anisotropic constitutive modeling, and the prediction and validation of a multilayered construct composed of biomimetic materials.

There are a number of limitations to this study. All finite element simulations were performed at zero axial load and therefore did not take into account the axial mechanical properties of the graft. This is noticeable in the results, as only the circumferential stress-strain response surfaces for the isocompliant and hypercompliant were qualitatively similar to that of rat aorta (Figure 24). Whereas none of the optimized grafts had axial stress-strain response surfaces qualitatively similar to rat aorta, all optimized grafts exhibited noticeably stiffer behavior in the axial strain range presented (Figure 25). This axial behavior mismatch is expected as the optimization scheme was focused on compliance matching, which would most directly impact the stress-strain behavior in the circumferential direction. Future studies will investigate compliance matching grafts while also taking into account the axial behavior so as to match all mechanical

properties of rat aorta. Another limitation to this study is the low resolution in creating the relatively low layer thicknesses that are required to match the number of elastin layers of a rat aorta, as thicknesses on the order of 5 microns are difficult to fabricate in a controlled manner with our current setup. This may explain the overestimated compliance for hypocompliant grafts, which had the highest percentage relative error for the G:PCL and T:PCL materials (27.6 ± 8.7% and 33.2 ± 5.7%, respectively). Additionally, the predictive model used to fabricate the hypocompliant grafts used mechanical data of materials which exhibited low strain ranges due to the high synthetic polymer content. Finite element simulations may result in strains beyond what is captured by the mechanical data and may therefore be less accurate at predicting mechanical behavior. The accuracy of the predictive model is heavily dependent on the captured mechanical data from strain ranges of the characterization constructs. Therefore, it is important in future studies to conduct mechanical tests that capture a broader range of strains and characterize other different types of synthetic and biological polymers blends that would increase our capacity to simulate different strain and compliance ranges. Finally, additional studies are necessary to evaluate important mechanical and biological properties of our optimized grafts such as permeability, burst pressure and cell and blood biocompatibility.

3.4 ACKNOWLEDGMENTS

This research was funded by the NIH, grant 1R56HL136517-01 to JPVG. Additional support for E.A. Tamimi was also provided by the National Institute of Biomedical Imaging and Bioengineering under award number EB003392. We would also like to acknowledge Scott Harrison for his contributions to the optimization scheme used in this work.

4.0 CHAPTER 4: SPECIFIC AIM 3

Specific Aim 3: *Quantify the strains of non-glaucomatous posterior scleral shells using sequential digital image correlation to evaluate the across three racioethnic groups: African descent (AD), European descent (ED), and Hispanic ethnicity(HIS), four regions: temporal (T), nasal (N), superior (S), and inferior (I), and three zones: peripapillary (PP) sclera, non-PP sclera, and optic nerve stumps at four intraocular pressure states: 5, 15, 30 and 45 mmHg.*

My hypothesis is that differences in the mechanical properties of the posterior sclera exist as a function of racioethnicity. The rationale for this is that ocular disease like open angle glaucoma is caused by the degeneration of retinal ganglion cells, which pass through the lamina cribrosa (LC). The mechanical theory of glaucoma rests on the assumption that mechanical damage forces acting on the optic nerve cause a loss of retinal ganglion cell function. The three zones currently being considered have the most proximity to the LC and could be part of the mechanism that leads to the onset of glaucoma.

The results presented in this chapter are the culmination of five years of research as part of an R01 grant (1R01EY020890-01A1). Originally, posterior sclera macroscopic biomechanical deformations were intended to be measured using digital image correlation of graphite markers glued in eight equally distributed 45° equatorial increments and three ~15° degree meridional increments about the posterior globe. However, this method was determined to produce relatively low strain resolution, especially with the geometry of the posterior of the eye. Our research group

collaborated with Dr. Katia Genovese, a co-author on work in which panoramic digital image correlation (p-DIC) was used to collect full-field biaxial data of murine aortas [169]. In that study, Bersi et al. cannulated aorta samples proximally and distally to a translating blunt-ended needle composite, which allowed both axial load and intraluminal pressurization. A random speckle pattern was generated on the sample, which was then placed coaxially within a conical mirror imaged by a camera fixed above the setup. The protocol resulted in detailed circumferential and axial deformations of the aorta samples. The p-DIC method was adapted by our research group into an S-DIC method meant to capture the deformations in the posterior sclera of eyes [170], which I utilized in the biomechanical response of the posterior scleras studied in the following chapter.

It should be noted that the work done for this aim was published with the following reference [171]:

Ehab A. Tamimi, Jeffrey D. Pyne, Dominic K. Muli, Katelyn F. Axman, Stephen J. Howerton, Matthew R. Davis, Christopher A. Girkin, Jonathan P. Vande Geest; *Racioethnic Differences in Human Posterior Scleral and Optic Nerve Stump Deformation*. Invest. Ophthalmol. Vis. Sci. 2017;58(10):4235-4246. doi: 10.1167/iovs.17-22141.

4.1 INTRODUCTION

Glaucoma is a neuronal degenerative disease that damages retinal ganglion cells leading to irreversible vision loss [172]. In 2010, glaucoma affected 60.5 million people, a number that is projected to rise to about 80 million by 2020 [173]. Risk factors for glaucoma include family history of glaucoma, race, age, and increased intraocular pressure [172, 174, 175]. These factors influence the biomechanical environment of the lamina cribrosa (LC), which is hypothesized to be

the primary region of mechanical insult in glaucoma [174, 176-179]. Changes in tissue properties of the optic nerve head and surrounding sclera are believed to accompany the initiation and progression of glaucoma by either influencing LC deformations or by causing a reduction of ocular blood flow [180-187]. Open angle glaucoma (OAG) has been shown to be more prevalent in AD populations at all ages, but proportionally increases more rapidly in the ED population over the same age compared to AD populations [175]. Stiffness of PP sclera surrounding the optic nerve has been reported to increase with age and in those of AD when compared to those of ED [188, 189]. Significant microstructural differences in human posterior scleral tissue are also present between these two racioethnic groups with those of AD having less equatorially aligned collagen fibers compared to those of ED [188, 190]. These microstructural and material property differences may be responsible for the varying rates of glaucoma occurrence observed between those of AD and ED. In addition, the prevalence of OAG for those of HIS was found to be higher compared to those of ED, but lower compared to those of AD [191]. To the authors' knowledge, no experimental biomechanical characterization of HIS posterior ocular tissues has been reported in the literature.

From these prior studies, it became evident to determine if there exist any fundamental biomechanical differences in non-glaucomatous eyes in posterior ocular tissues across races and posterior eye regions. Experimental determination of the biomechanical properties of the enucleated optic nerve stump (ONS) and sclera is challenging due to their non-linear and anisotropic response as well as their complex geometry. High-resolution deformation protocols of the posterior sclera that use pressure-inflation experiments have been reported with 3D digital image correlation (DIC) [192-194], 3D ultrasound speckle tracking (UST) [195-199], and electronic speckle pattern interferometry (ESPI) [200-204] being among the most commonly used

full-field optical techniques. ESPI offers very high scleral deformation sensitivity [200, 203] while 3D DIC has achieved high resolution measurement of in-plane scleral displacement [192, 194]. 3D UST has been used to acquire volumetric scans quantifying complex internal scleral strains [198]. Despite their numerous utilization in scleral deformation studies, none of these 3D deformation measuring techniques have been used to quantify human ONS displacement, due to current measurement limitations and the aspherical geometry of posterior ocular tissues [192]. This complex geometry demands proper contouring and matching of the local shape with the displacement measurement to enable correct strains map calculation [192, 205, 206]. For ESPI, these geometry deviations lead to shadows from oblique illumination that results in irregular data analysis [207]. In standard DIC techniques, such complex non-spherical geometries with sharp angles are not fully captured in the two viewing angles leading to improper correlation and reconstruction. Since these angles cannot be readily changed without influencing in-plane and out-of-plane resolution [208], data analysis from these methods is not accurate for these complex geometry regions.

Our research group recently developed an S-DIC method with advanced 3D capabilities to map posterior sclera and ONS deformations [208]. In this method, we improved the *z* (in-depth) resolution without loss of x-y (in-plane) sensitivity in DIC measurements. Our approach employed one high-resolution camera that recorded videos of a pressure inflation device as it moved through two orthogonal parallax axes using a standard 3D DIC approach to quantify the deformation of posterior sclera and ONS across carefully selected sequential movie frames (up to the frame rate of the camera). The capabilities of the S-DIC technique were assessed in a prior work by the measurements of shape and displacement on a rigid complex geometry (ONS surrogate) with a reconstruction accuracy of 0.17% and 8 μm uncertainty in the out-of-plane direction [208]. There

are few studies in the literature which have studied the biomechanical properties of the ONS [184, 186, 209-212]. As for comparisons across racioethnic groups, only variation of laminar depth with age [213] and LC displacement [214] in normal eyes across AD and ED groups have recently been reported. The racioethnic variation in intraocular pressure (IOP) induced deformation of the human ON in non-glaucomatous tissue has not been reported in the literature, in particular for those of HIS. The purpose of this work was to use S-DIC to evaluate the strains of non-glaucomatous scleral shells across three racioethnic groups (AD, ED, and HIS), four regions: temporal (T), nasal (N), superior (S), and inferior (I), and three zones (PP sclera, non-PP sclera, and ONS). This comparison was done by analyzing data from four IOP states: 5, 15, 30 and 45 mmHg.

4.2 MATERIALS AND METHODS

4.2.1 Posterior Scleral Shells and Optic Nerve Stumps

Posterior scleral shells from human donors of AD (57-98 years old, n= 7 eyes), of ED (52-92 years old, n=11 eyes) and HIS (56-95 years old, n=5 eyes) were received from the Alabama Eye Bank in Birmingham, AL, the Banner Sun Health Research Institute in Sun City, AZ, the Donor Network of Arizona in Phoenix and Tucson, AZ, the Illinois Eye Bank in Chicago and Bloomington, IL, the Michigan Eye Bank in Ann Arbor, MI, and the San Diego Eye Bank in San Diego, CA. All eyes were classified as non-glaucomatous according to available medical paperwork, next of kin questionnaires, and/or later confirmed via optic nerve axon count. Age of all donors for this study was limited to those over 50 years of age. The eyes were kept on ice until they were shipped to our laboratory and were stored in physiological saline at 4 °C. For axon counting, the optic nerves corresponding to the scleral shells were cut and fixed immediately in Poly/LEM (Polyscience, Inc,

USA) at their respective eye banks, at which point they were sent to our laboratory. Once received, the nerves were transferred to vials containing 2.5% glutaraldehyde, in which they stored for 24 hours, transferred to phosphate buffered saline (PBS) and stored at 4 °C until they were sent out for processing. For processing, two to three 1mm thick slices were cut from the middle of the available axial length of each nerve. In a few cases, a clean slice could not be prepared, and these nerves were left intact. The slices were washed several times with PBS, and fixed with 1% osmium tetroxide in PBS for 2 hours on ice. The samples were extensively rinsed with ddH20, dehydrated through a grades series of ethanol concentrations, treated with propylene oxide, and infiltrated with Eponate 12 resin overnight (Ted Pella, Redding, USA). The following day, the slices were placed in fresh resin, and polymerized at 60°C overnight. Semi-thin sections were cut from the blocks on an Ultracut E ultramicrotome (Reichert-Jung, Wein, Austria) and stained with 1% toluidine blue in 1% sodium borate. Unfortunately, some of the embedded slides lacked the necessary quality for axon counting and were not used. Table 5 reports the race, age, gender and anatomical location of all donor eyes, including whether or not the optic nerve cross-section was used for axon counting.

Table 5. Donor race, age, gender, anatomical location and axon count availability of all donor eyes used in this study.

Eye #	1	2	3	4	5	6	7	8	9	10	11	12	13	14	15	16	17
Race	AD	AD	AD	AD	AD	AD	AD	ED	ED	ED	ED	ED	ED	ED	ED	ED	ED
Age	62	64	57	66	72	70	98	90	62	78	72	64	70	52	70	92	74
Gender	F	F	F	M	M	F	F	F	M	M	F	M	M	M	M	F	M
Globe	OS	OD	OS	OS	OS	OS	OS	OD	OD	OS	OD	OS	OS	OS	OS	OD	OS
Axons?	Y	Y	Y	Y	Y	N	N	N	Y	Y	Y	Y	Y	Y	Y	Y	Y

Table 5. (continued)

Eye #	18	19	20	21	22	23
Race	ED	HIS	HIS	HIS	HIS	HIS
Age	75	58	80	95	86	56
Gender	M	M	M	M	F	M
Globe	OS	OS	OS	OS	OS	OS
Axons?	Y	N	N	N	Y	Y

4.2.2 Automated S-DIC

All scleral shells were tested using an S-DIC inflation procedure previously developed by our research group [208]. As part of our research group's efforts to enhance our previously reported S-DIC imaging approach, significant improvements were made to the system to reduce hands-on imaging time, maintain consistent eye hydration, upgrade vibration control, and streamline post-processing methods. Overall, the most significant improvement to the S-DIC system was the

inclusion of automated motor rotational stages (Thorlabs CR1-Z7, PRM1Z8), controlled by LabView (National Instruments, Inc) that acted as the primary controller that managed the camera acquisition and rotational stage movements throughout the experiments. The inclusion of the automatic motors allowed for improved vibration control due to the fine incremental rotational motion resolution, as well as eliminated the need to open the humidity chamber doors for manual actuation thus improving humidity consistency. All other S-DIC experimental protocol steps remained identical to our previously published approach [34], including eye dissection, eye positioning within the clamp system, speckle pattern application, preconditioning, and imaging at the pressure steps of 5, 15, 30, and 45 mmHg. With decreased image acquisition time, the automated S-DIC method allowed the user interaction with the system to be completely hands-off once the eye was properly installed. The S-DIC post-processing techniques were also improved with the automated system through acquiring consistent angle sequence images between ocular experiments. This allowed for robust post-processing scripts, less procedural variations between eyes and faster generation of ocular strain fields. To generate strain maps, strains were calculated following the protocol described in our previous study [208]. Briefly, a geometry mesh was generated using measured position data triangulation. Larger elements were re-meshed using custom Matlab code so that the element sizes for all regions and zones were similar. The Green–Lagrange strain tensor, **E**, was computed for each element using the equation $\boldsymbol{E} = \frac{1}{2}(\boldsymbol{F}^T\boldsymbol{F} - \boldsymbol{I})$, where $\boldsymbol{F}$ is the deformation gradient tensor and $\boldsymbol{I}$ is the identity matrix. $\boldsymbol{E}$ was used to calculate two in-plane principal strains for each element, E1 and E2. The strain calculations assumed that the 5 mmHg base geometry was the undeformed state for each inflation pressure. This resulted in three pairs of elemental principal strains: E1 and E2 from 5 to 15, 5 to 30, and 5 to 45 mmHg (simply referred to as pressures 15, 30, and 45 mmHg for the remainder of this manuscript).

4.2.3 Zonal and Regional Segmentation

In order to compare strain values from different spatial locations, all geometries were segmented into three zones and four regions. With regards to the zones, each geometry was divided into the ONS, the PP sclera and the non-PP sclera. Briefly, the geometry was rotated so that the ONS pointed in the positive z-direction. A Hessian matrix was calculated along the geometry and was used to determine the mean curvature for each element. Using a curvature criterion, the saddle points of the ONS ring were determined and used to fit to a dividing plane. All elements above the plane were designated as ONS elements as shown in Figure 26A. The remaining elements within a distance of 2 mm below the plane were designated as PP scleral elements [215]. The remainder of the scleral elements were designated as non-PP scleral elements, as shown in Figure 26B. After zonal segmentation, the ONS elements were imported into Rhinoceros 3D (Robert McNeel & Associates, USA), which was used to close the ONS geometry so that the volume of each ONS could be calculated for each sample (mm^3). In addition, the diameter and length of the ONS were calculated. Due to the non-uniform shape of the ONS, the diameter was calculated for each sample by subtracting the maximum and minimum positions of the ONS in the x and y direction. Both of these measurements were averaged and recorded as the diameter (mm). Similarly, the maximum and minimum positions of the ONS were subtracted in the z-direction. This was recorded as the ONS length (mm). It should also be noted that the ONS zone for all eyes encompassed mostly the optic nerve sheath and a small portion of the optic nerve that was exposed during the enucleation process.

For regional definition, the geometry was divided into S, I, T, and N. To do this, the centroid of the scleral opening produced by the dividing plane was set as the origin of the geometry. Furthermore, the geometry was rotated so that the normal of the dividing plane was aligned with

the z-axis. The nodes of the all elements were converted from Cartesian to spherical coordinates. The known S direction was set as 0° in the meridional direction. All elements within 45° of the S direction were designated as S elements. The same was done for the remaining regions dividing the whole geometry into four equally spaced regions as shown in Figure 26C. The orientation of the T and N direction was determined by whether the eye was oculus dextrus (OD) or oculus sinister (OS). The overall twelve spatial locations defined by regions and zones are shown in Figure 26D.

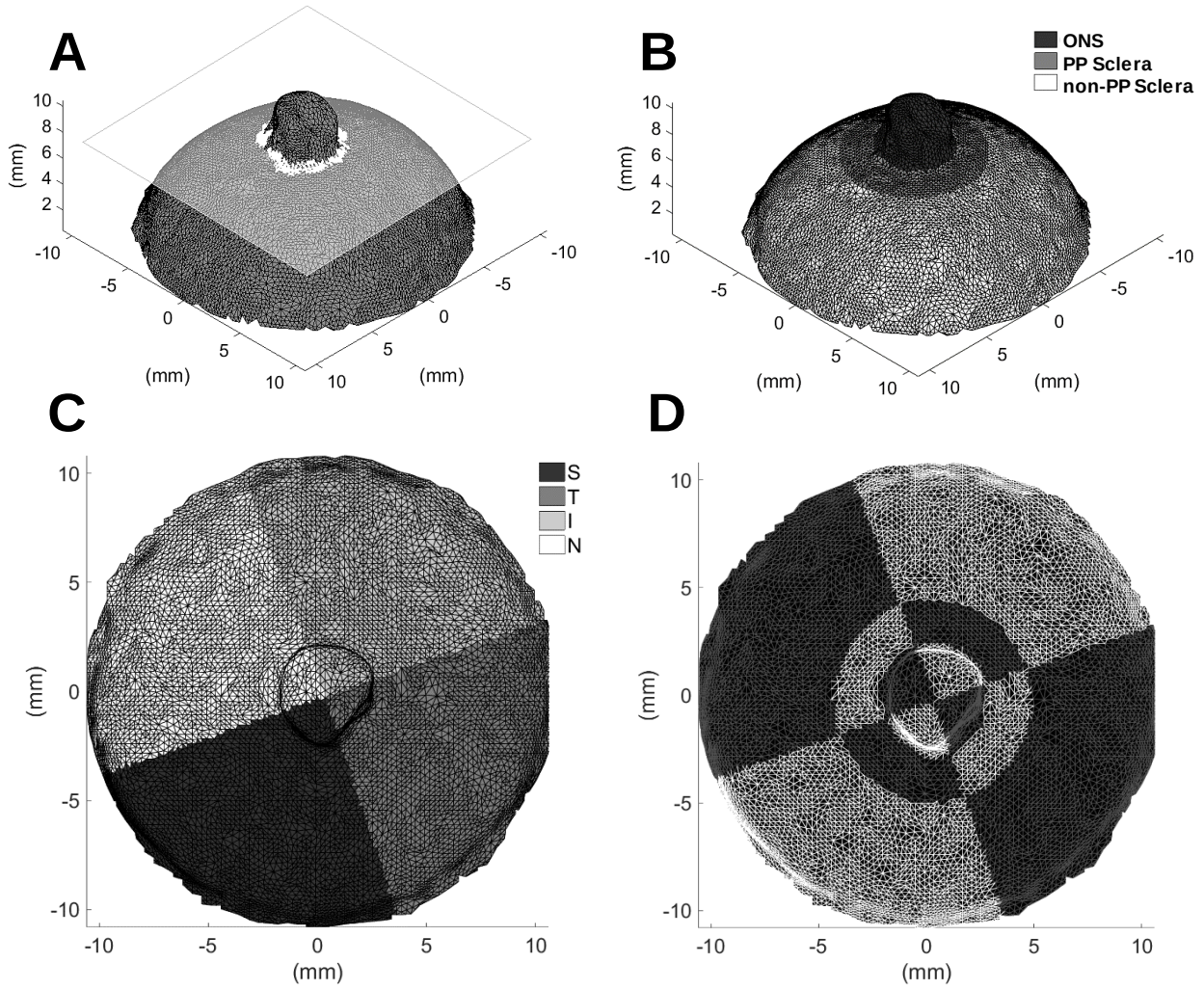

Figure 26. Posterior scleral pole showing: A) the dividing plane based on optic nerve stump saddle ring points, and the division into B) optic nerve stump, peripapillary scleral and non-peripapillary scleral zones, C) superior, temporal, inferior and nasal regions, D) twelve spatial locations defined by regions and zones.

4.2.4 Optic Nerve Axon Counting

The embedded optic nerve cross-sections were visualized on a Nikon Eclipse 90i microscope using a montaging method with Nikon NIS-Elements software. The method utilized individually imaged

60x magnifications with autofocus capabilities and a 15% overlap. A complete montage of an axon cross-section is shown in Figure 27. Semi-automated axon counts were executed using image processing techniques in Matlab, and methodology adapted from literature [216, 217]. The user was first prompted to identify the bounds of the optic nerve cross section in order to crop the image. Contrast-limited adaptive histogram equalization was applied to the cropped image to improve user accuracy of axon identification. The cropped portion of the image was divided equally into a sectional grid comprised of 200 sections horizontally by 200 sections vertically. From these 40,000 sections, ten individual sections of axons were randomly selected and presented one at a time, and the user was prompted to manually click on the axons in each section. These manual counts were averaged across all ten counted sections, providing an average axon density for the small image size. This was done to create a more accurate representation of the average axon density in these sections with respect to the entire optic nerve area, as axon distribution is somewhat non-uniform by nature. This calculated density was then used to extrapolate across the entire cross-section to give an estimated axon count for the whole nerve. Each image was "counted" through the program three times to improve repeatability and accurate averages with standard deviations of axon counts being calculated for all nerves.

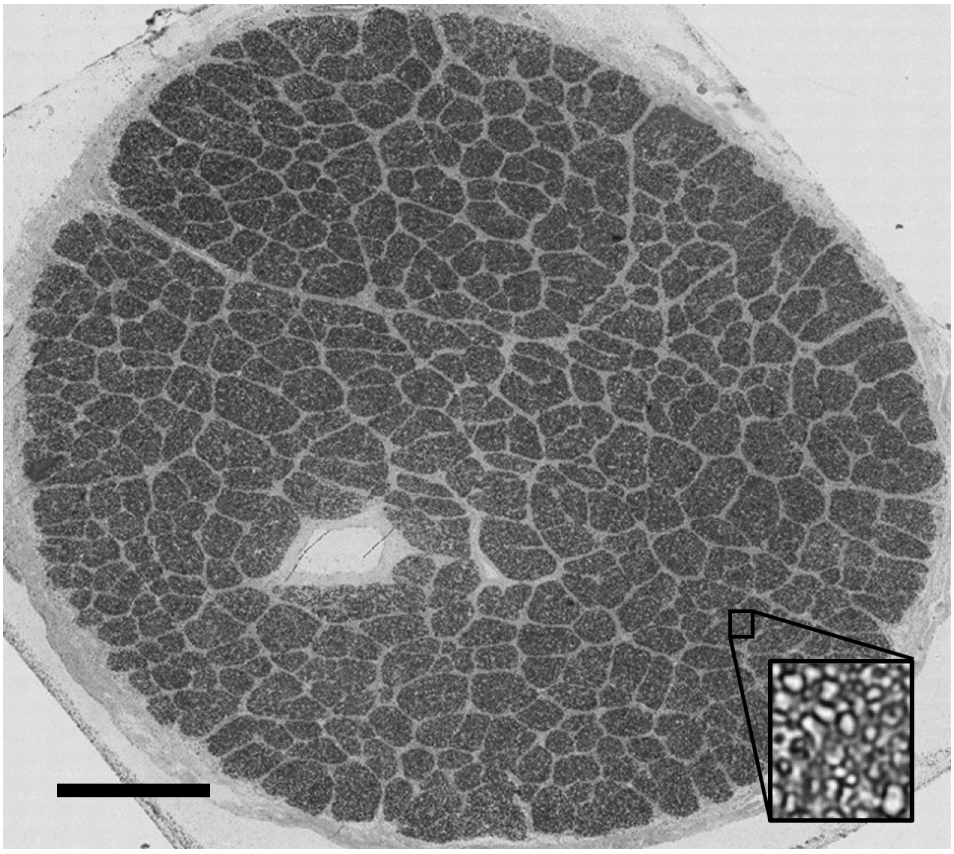

Figure 27. Microscope image of full optic nerve cross section used for semi-automated axon counting. Dark sections indicate bundles of axons separated by lighter connective tissue. Scale bar indicates 500 microns.

4.2.5 Statistical Analysis

A statistical analysis was performed using scripts written in R (R Core Team, GNU General Public License). Specifically, a parsimonious linear mixed model built to account for repeated measures (lmer) was utilized. Racioethnicity (AD, ED and HIS), zone (ONS, PP sclera, non-PP sclera), region (S, T, I, and N) and pressure (15, 30, and 45 mmHg) were considered fixed repeated measure variables. For this model, pressure was considered as a discrete variable to evaluate racial and zonal differences at specific inflation pressures. Each donor was considered an individual subject for the repeated measures portion of the model. Mean E1 and E2 estimates were determined

for each spatial location at every inflation pressure. The data was arranged in a factorial form suitable for the statistical model. All data was normalized using a two-step SPSS Statistics (IBM Corporation, USA) transformation procedure that utilized inverse distribution functions [218]. *Post hoc* mean E1 and E2 estimates were calculated using an R least squares mean function (lsmeansLT). Pairwise comparisons were calculated using an R differences of least squares means function (difflsmeans). Both of these functions utilized the R linear mixed model previously mentioned. To account for familywise error, a Bonferroni-type correction was applied on any pairwise test conducted.

For regression analysis, pressure was considered as a continuous variable to determine the relationship of E1 and E2 as a function of pressure for every zone for each racioethnic group. This was done using the linear mixed model in SPSS. Similar to the R model already mentioned, zone and region were considered repeated measure variables and each donor considered an individual subject for the model. Additionally, the same regression model was used to determine the relationships of mean E1 and mean E2 at all spatial locations and inflation pressures as a function of ONS volume and optic nerve axon count.

4.3 RESULTS

4.3.1 Principal Strain Maps

The principal strain magnitudes (E1 and E2) for the 5 to 45 mmHg inflation of one representative sample from each racioethnic group are shown in Figure 28. The E1 and E2 magnitudes in the ONS region were qualitatively larger than that of the scleral zones for all racioethnic groups. E2 magnitudes (compressive) were qualitatively higher than that of E1 magnitudes (tensile) in the

same region. Furthermore, more qualitative regional heterogeneity can be observed in the ED and HIS samples, compared to the AD sample. Overall, the reported values of E1 and E2 in the scleral zones were consistent with values reported in the literature.

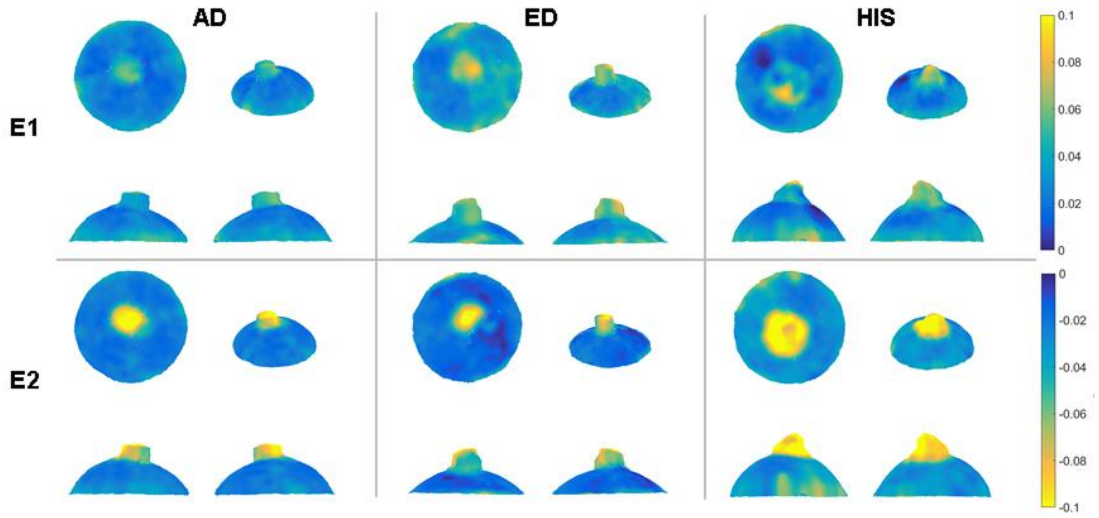

Figure 28. A representative example of E1 and E2 strain maps at 45 mmHg from each racioethnic group. Four views are included for each sample: top view (upper left), isoparametric view (upper right), back side view (lower left) and front side view (lower right). Note: the color map for the E2 strain maps has been reversed compared to the E1 strain maps to emphasize absolute value.

4.3.2 Statistical Analysis

4.3.2.1 Pressure as discrete variable. A linear mixed model was performed in R using pressure as a discrete variable. The R linear mixed model results showed that all interaction terms higher than a second order interaction were not significant and were therefore removed from the main model expression. The mean E1 and E2 estimates, which represent the values predicted by the statistical model, were calculated and pairwise comparisons were performed between racioethnic

groups for all three zones at each inflation pressure. The zonal comparisons are shown in Figure 29.In the ONS (Figure 29A), the mean E1 values for AD eyes were significantly higher than that of ED eyes (p-value = 0.024) at 15 mmHg. Similarly, the mean E2 absolute values were significantly higher for AD eyes compared to that of ED at 15 mmHg. No significant zonal differences across racioethnic groups were shown at 30 and 45 mmHg for both mean E1 and E2 values. For the PP scleral zone (Figure 29B), the mean E1 values for ED eyes were significantly lower than that of AD and HIS eyes (p-value = 0.0219 and 0.0387, respectively) at 15 mmHg. No significant racioethnic differences were observed at 30 and 45 mmHg in the PP scleral zone. The mean E2 values were significantly higher for AD eyes compared to ED eyes at 15 mmHg (p-value = 0.049). For the non-PP scleral zone (Figure 29C), there were no significant racioethnic differences for mean E1 nor mean E2 values at all inflation pressures.

There were few significant regional differences within racioethnic groups at different inflation pressures. In the PP zone for HIS eyes, the mean E2 absolute values for the T region was lower than that of the N region at 15 mmHg (p-value = 0.048, respectively). For the non-PP scleral zone, the ED mean E1 values for I region were higher compared to the S region for 30 mmHg (p-value = 0.048). For the mean E2 absolute values, the I region was significantly higher than the T region at 30 and 45 mmHg for ED eyes (p-value = 0.024 and 0.03, respectively). All other mean E1 and mean E2 regional differences within racioethnic groups were not significant. For zonal differences within racioethnic groups, the mean E1 values and mean E2 absolute values for the ONS zone were significantly higher than that of both the PP and non-PP scleral zone for all racioethnic groups at all inflation pressure (p-value < 0.001 for all). All other mean E1 and mean E2 differences between PP and non-PP scleral regions within racioethnic groups were not significant.

Pairwise comparisons were made between different pressure states for each zone within each racioethnic groups. For the AD eyes in the ONS zone, E1 values at 30 mmHg were significantly lower than that of 45 mmHg (p-value = 0.033) and the E2 absolute values at 15 mmHg were significantly lower than that of 45 mmHg (p-value = 0.012). In the non-PP zone, the E1 values for AD eyes at 15 mmHg were significantly lower than that of 45 mmHg (p-value <0.001). For ED eyes, the ONS mean E1 values at 45 mmHg were significantly higher than that of 30 and 15 mmHg (p-value = 0.045 and <0.001, respectively). The ONS mean E2 absolute values at 15 mmHg were significantly lower than that of 45 mmHg (p-value = 0.026). In the PP scleral zone, the ED mean E1 values at 15 mmHg was significantly lower than that of 30 and 45 mmHg (p-value = 0.033 and <0.001, respectively). Furthermore, the mean E1 values for ED eyes at 30 mmHg in the PP scleral zone was significantly lower than that of 45 mmHg (p-value = 0.015). As for the non-PP scleral zone, the mean E1 values for ED eyes at 15 mmHg were significantly lower than that at 45 mmHg (p-value = 0.026). As for HIS eyes, in the ONS zone, the mean E2 absolute values at 15 mmHg were significantly lower than that at 45 mmHg (p-value = 0.023). In the PP scleral zone, the mean E1 values at 15 mmHg were significantly lower than that at 45 mmHg (p-value = 0.002). In the non-PP scleral zone, the mean E1 values at 15 mmHg were significantly lower than that at 45 mmHg (p-value = 0.028). All other comparisons in all zones for all racioethnic groups were not significantly different.

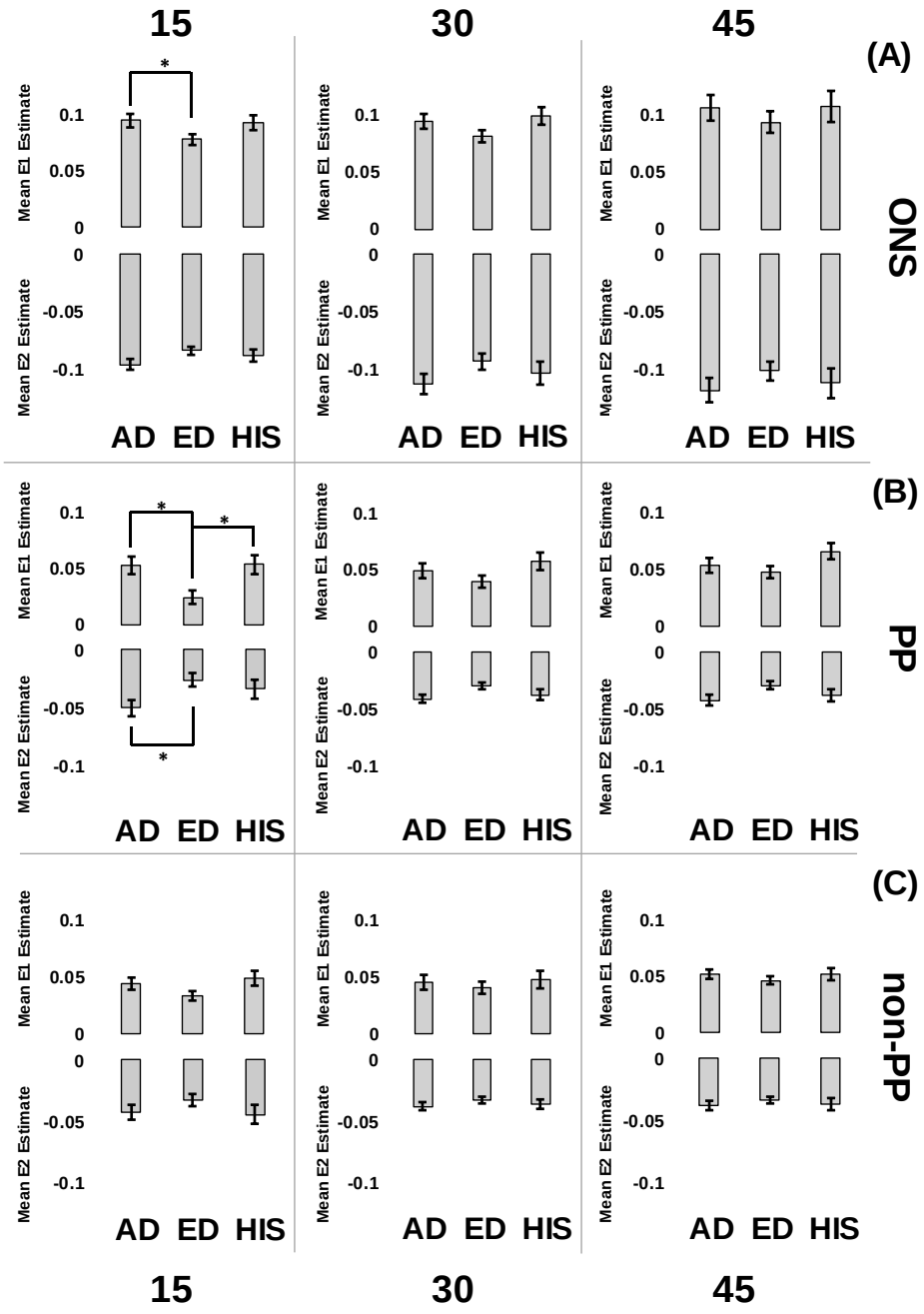

Figure 29. Mean E1 and E2 value estimate regional and zonal comparisons for all inflation pressures for each racioethnic group. Asterisk indicates p-value < 0.05. The error bars indicate the standard error as estimated by the statistical model. There were significant racioethnic differences in tensile principal strains values in the optic nerve stump and the peripapillary sclera zones. Additionally, there were significant racioethnic differences in compressive principal strains values only in the peripapillary sclera zone.

4.3.2.2 Pressure as continuous variable. A mixed linear model was performed in SPSS using pressure as a continuous variable to determine the relationship of mean E1 and E2 values as a function of pressure. This was done for each zone for each racioethnic group. The regression results are shown in Figure 30. In the ONS, only ED eyes had a significant positive relationship between mean E1 values and pressure (p-value = 0.003). AD, ED, and HIS eyes had a significant positive relationship between mean E2 absolute values and pressure (p-value = 0.005, < 0.001 and 0.017, respectively). In the PP scleral zone, both ED and HIS eyes had a positive relationship between mean E1 values and pressure. Furthermore, the slope of the mean E1 pressure relationship of the ED eyes was significantly higher than that of AD eyes (p-value = 0.04). For mean E2 values, there was no significant relationship with pressure for any of the racioethnic groups. As for the non-PP scleral zone, AD, ED and HIS eyes had a significant positive relationship between mean E1 values and pressure (p-value = 0.003, <0.001 and 0.006, respectively).

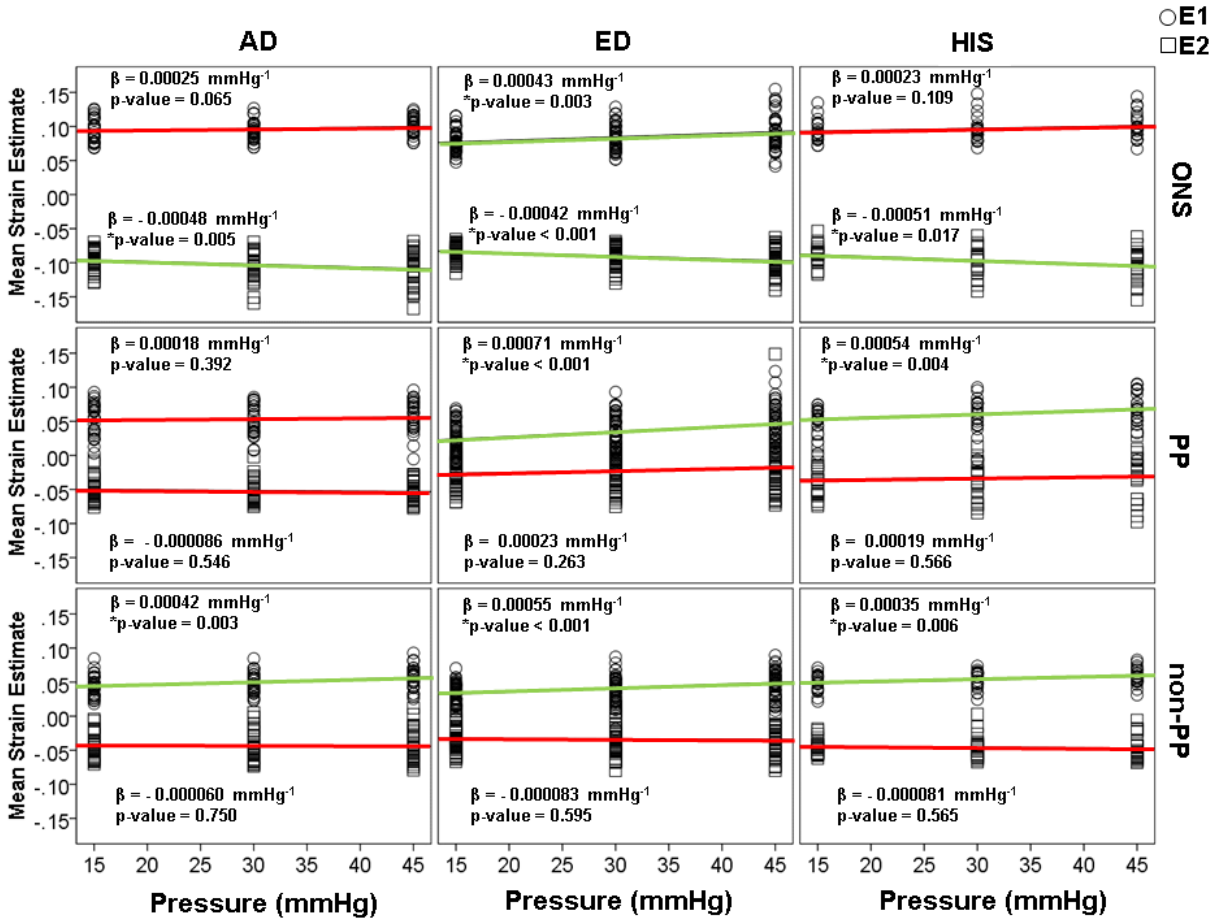

Figure 30. Regression plots of mean E1 and E2 values as a function of pressure as a continuous variable for all racioethnic groups within each zone. The tensile principal strains (E1) of European descent and Hispanic ethnicity peripapillary sclera were had a significant relationship with pressure, whereas African descent peripapillary sclera did not. Green indicates regressions that are significant, whereas red indicates regressions that are not significant.

4.3.3 Axon Count

The mean axon counts were $9.05x10^5 \pm 1.2x10^5$, $9.65x10^5 \pm 2.1x10^5$, $1.1x10^6 \pm 3.0x10^5$ for the AD (n=4), ED (n=10), and HIS (n=2) donors, respectively, where the ranges indicate standard deviations. A two-tailed Student's t-test was performed comparing the AD and ED eyes, which showed that there was no significant difference between both groups in regards to the optic nerve

axon count (p-value = 0.964). A mixed linear model was performed in SPSS using axon count as a continuous variable to determine the relationship of mean E1 and E2 values for all eyes as a function of axon count for all three zones at 15, 30 and 45 mmHg. In the ONS zone, there was a significant negative relationship between mean E1 values and axon count at 45 mmHg (p-value = 0.002). There was a significant positive relationship between mean E2 absolute values and axon count at 45 mmHg (p-value =0.006). In the PP scleral zone at 45 mmHg, there was no significant relationship between mean E1 values and pressure (p-value = 0.961) however there was a significant positive relationship between E2 absolute values and axon count (p-value = 0.022). In the non-PP scleral zone at 45 mmHg, there were no significant relationships of neither mean E1 values nor mean E2 values with axon count (p-value = 0.106 and 0.596, respectively). All relationships between mean E1 and E2 and axon counts at 15 and 30 mmHg at all zones were shown to be not significant. The regression plots for all zones at 45 mmHg are shown in Figure 31.

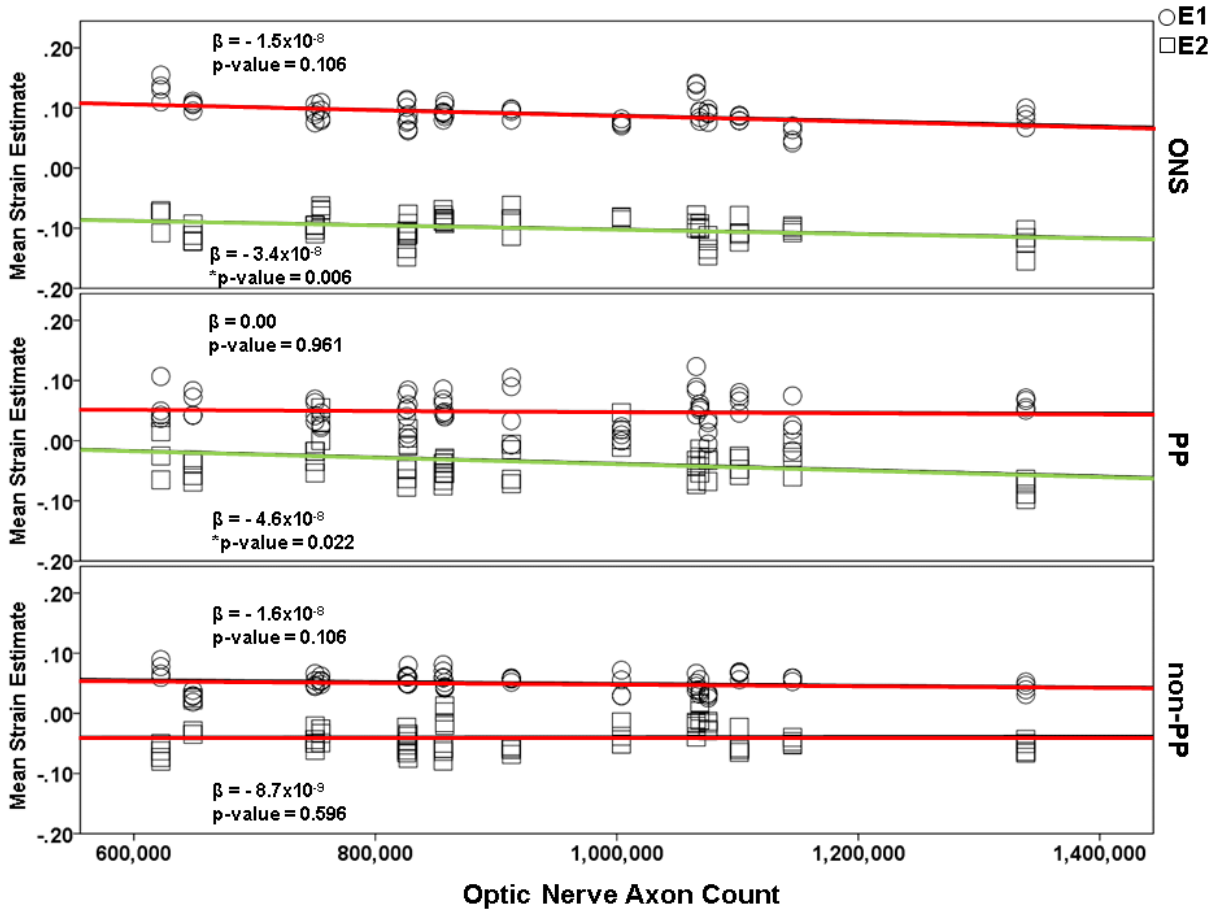

Figure 31. Regression plots of mean E1 and E2 values as a function of optic nerve axon count at 45 mmHg within each zone. The compressive principal strains (E2) had a significant relationship with optic nerve count in the optic nerve stump and peripapillary scleral zones. Green indicates regressions that are significant, whereas red indicates regressions that are not significant.

4.3.4 ONS Dimensions

The mean ONS volumes were 16.2 ± 6.0 mm^3, 23.6 ± 7.9 mm^3, 17.1 ± 11.9 mm^3 for the AD, ED, and HIS donors, respectively. The mean ONS diameters were 5.2 ± 0.4 mm, 6.4 ± 0.7 mm, and 6.3 ± 1.7 mm for the AD, ED, and HIS donors, respectively. The mean ONS lengths were 2.9 ± 0.4 mm, 3.2 ± 0.7 mm, and 6.3 ± 0.9 mm for the AD, ED, and HIS donors, respectively. All ranges

for all dimensions indicate 95% confidence intervals. Single factor ANOVA analysis revealed that there were no significant differences between the different racioethnic groups in regards to the ONS volume (p-value = 0.330), diameter (p-value = 0.154) and length (p-value = 0.632). Comparisons of ONS volume, diameter, and length between racioethnic groups are shown in Figure **32**.

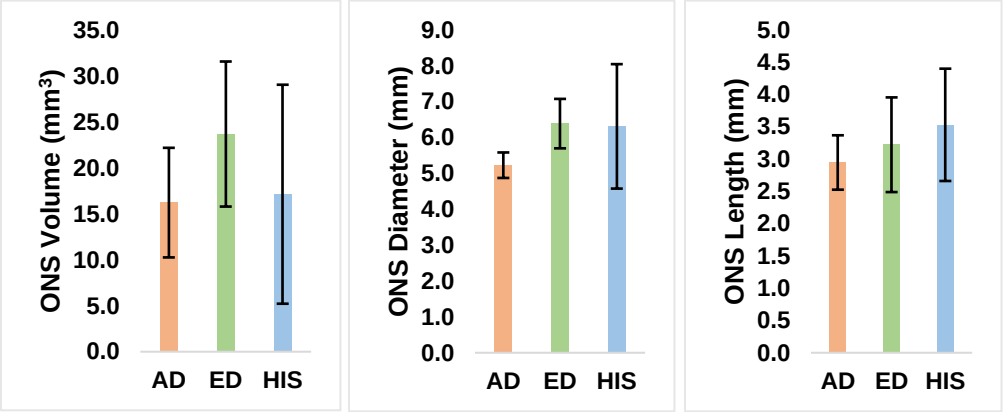

Figure 32. ONS volume (left), diameter (middle) and length (right) comparisons between racioethnic groups. Error bars indicate 95% confidence interval. There were no significant racioethnic differences in ONS volume, diameter or length for all eyes.

In addition, to evaluate the effect of the ONS size on the E1 and E2 values, a mixed linear model was performed in SPSS determine the relationship of mean E1 and E2 values for all eyes as a function of ONS volume for all three zones at 15, 30 and 45 mmHg. The results are shown in Figure 33. Overall, it was found that the mean E1 and mean E2 value did not have a significant relationship with the ONS volume in the ONS zone. As for the PP scleral zone, the mean E1 values had a significant negative relationship with the ONS volume at 15 mmHg only (p-value = 0.002). As for the non-PP scleral zone, there was a significant relationship between mean E1 and ONS volume at all pressures (p-value < 0.001 for all).

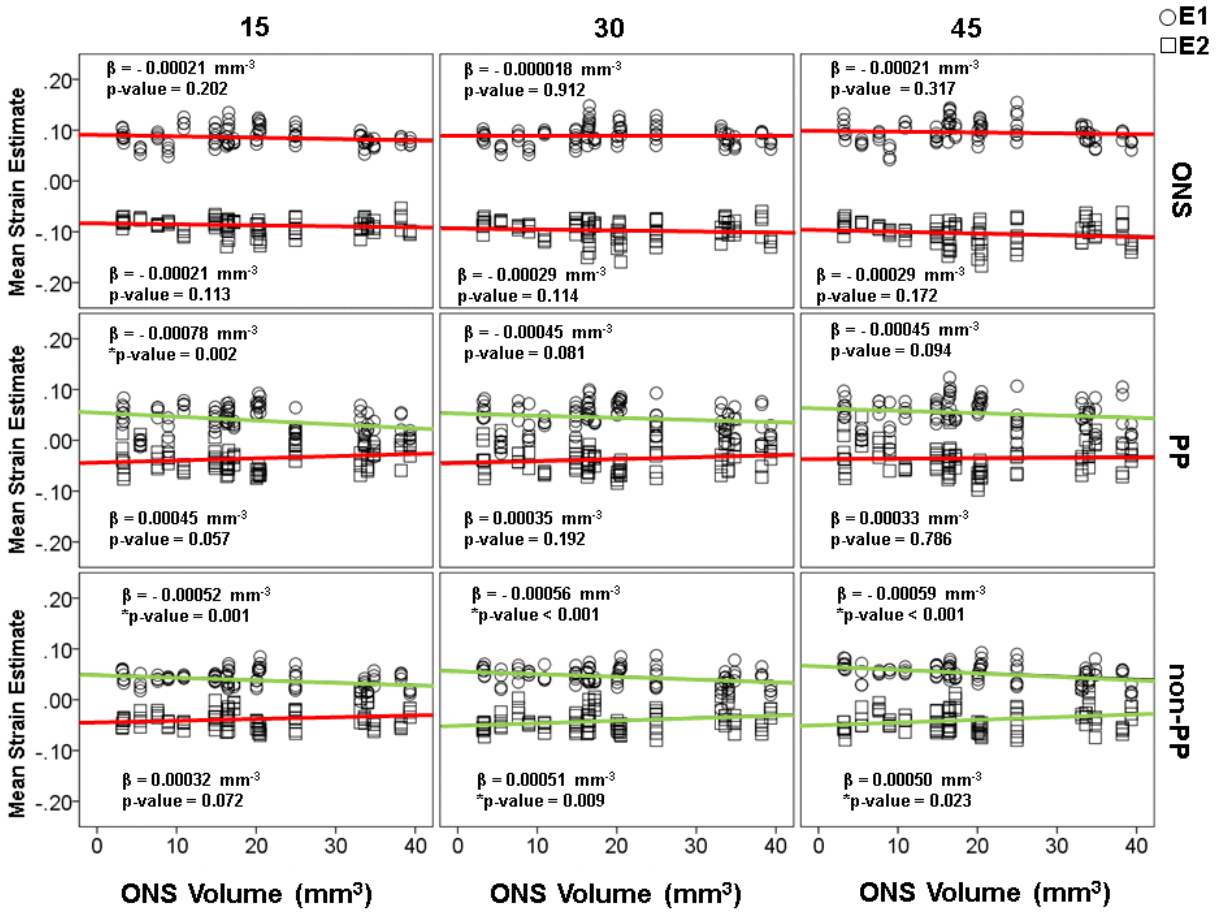

Figure 33. Regression plots of mean E1 and E2 values as a function of ONS volume for all inflation pressures within each zone. The tensile principal strains (E1) had significant relationships with ONS volume in the peripapillary scleral zone for all pressures. Most tensile (E1) and compressive (E2) principal strains had significant relationships with the ONS volume in the non peripapillary scleral zone for all pressures.

4.4 DISCUSSION

A zonal racioethnic in-plane principal strain comparison was conducted across three inflation pressures for normal human scleral shells using displacement measurements collected via S-DIC. The ONS tensile and compressive strains for the ED eyes were significantly lower than that of AD

eyes at 15 mmHg (Figure 29A). The PP scleral compressive strains for the AD eyes were significantly larger than that of ED eyes at 15 mmHg (Figure 29B). For ED and HIS eyes, tensile strains in the ONS and non-PP scleral zones increased significantly with pressure, while AD eyes showed a significant relationship with pressure in the non-PP scleral zone only (Figure 30). Additionally, only ED and HIS eyes had a significant positive relationship between tensile strain in the PP scleral region, while AD PP scleral strains did not have a significant relationship with pressure. All racioethnic groups had significant compressive strain relationships with pressure in the ONS zone (Figure 30).

Several studies have previously used principal strains as an endpoint to compare spatial locations in eyes [184, 200, 219, 220], while some used circumferential and meridional strain [192, 221, 222]. The principal strain values reported in our study were found to be within the range of principal strain values shown in other studies. Fazio et al. used ESPI to investigate the mean maximum principal strain (E1) regional variability in the PP and mid-peripheral scleral regions (each divided into eight meridional regions) in 10 pairs of normal eyes ages 57-90 years old with non-specified racioethnic classification [200]. The study by Fazio et al. showed that the I region demonstrated E1 strain values higher than the S and N regions, which was consistent with our regional trend of the ED tensile strains in the non-PP scleral zone. Coudrillier et al. found regional differences in fiber alignment in the PP scleral location for normal eyes (n=9) [222]. In addition, our research group has previously investigated regional microstructural differences for glaucomatous and normal human eyes of ED [223]. In that study, Danford et al. showed that normal ED eyes exhibited lower percent of equatorial fiber organization in the I region compared to all other regions, especially as compared to the N region which had the highest degree of circumferential fiber alignment. This disparity may explain the higher tensile and compressive

strains in the I region of ED samples reported in the current study as a larger degree of non-circumferential fibers may lead to increased fiber realignment into the circumferential direction and subsequently larger in-plane compressive strains. Future microstructural information in AD and HIS eyes could further explain the various regional strain differences observed throughout all racioethnic groups. These studies are currently ongoing in our laboratory.

With regards to zonal differences within racioethnic groups, the study by Fazio et al. found that the PP sclera exhibited significantly higher mean maximum values of principal strains (E1) than mid-peripheral scleral regions for a 5-45 mmHg pressure inflation [200]. This is not consistent with our results which showed tensile differences only between the ONS and the both scleral zones at all pressures. The study by Fazio et al. also reported that PP sclera exhibited significantly higher values of mean E1 strains than mid-peripheral sclera for both donors of AD and ED[188]. This was also in contrast to our results which indicated that the PP sclera did not differ significantly from the non-PP region for AD and ED eyes. This could be due to our study including non-PP sclera beyond the mid-peripheral scleral zone. Furthermore, the ONS volume of eyes in our study seemed to have a significant effect on the tensile and compressive strain values in the non-PP scleral zone (Figure 33). This could further explain why our ED and AD zonal comparison results differed from those of Fazio et al. who did not include the ONS [188]. In addition, the discrepancy between our research groups in zonal differences within racioethnic groups could be explained by a number of other factors, including scleral thickness variations. For example, a study by Norman et al. showed that strain differences between PP and non-PP strains could be attributed to the thickness increases adjacent to the optic nerve head [220]. This was also confirmed by Coudrillier et al., who measured scleral thickness and reported a different stiffness between the PP and mid-posterior scleral regions for both normal and glaucomatous eyes [192], which they attributed to

the PP sclera having lower degree of fiber alignment and lower mechanical anisotropy compared to mid-posterior scleral regions [221]. To the author's knowledge, Grytz et al. and Fazio et al. are two of the few research groups that have studied racioethnicity as a factor in normal posterior scleral material properties using ESPI. In a study by Grytz et al., the authors report that the in-plane strain, which they describe as the strain tangent to the scleral shell surface, was found to be significantly lower in donors of AD compared to ED in the PP scleral region (p-value = 0.015) for age groups of 20-90 and 23-73 years old, respectively, inflated from 5 to 45 mmHg [189]. The scleral strain results from Grytz et al. were not consistent with our results, which showed significantly lower PP scleral tensile strain for ED samples compared to AD samples at 15 mmHg (p-value = 0.024). Furthermore, the PP scleral compressive strains for the ED samples were significantly smaller than that of AD at 15 mmHg (p-value = 0.049) (Figure 29B). Discrepancies between our results and those of Grytz et al. could be attributed to differences in scleral thickness. Grytz et al. found no significant difference in scleral thickness between ED and AD eyes [189].

However, racioethnic differences in scleral thickness could have contributed to the discrepancies that we observe between our different groups. Our laboratory is currently analyzing x-ray micro computed tomography (μCT) images of the same scleral shells used in this study. Our preliminary results suggest that the sclera of ED eyes may be thicker than that of AD eyes, which would explain why the PP scleral strains of ED eyes would be smaller than that of AD eyes in our study. Grytz et al. used ultrasound to obtain thickness at 20 points for each eye (n=40 for ED 20-90 years old, n=22 for AD 23-73 years old). Eyes included in this study are restricted to donors older than 50 years old and the sample number in our study is lower than that of Grytz et al. The differences in thickness measurements between the racioethnic groups could be due to differences in measurement technique, age, the source and/or inherent variability. Furthermore, the eyes

examined by Grytz et al. had their optic nerves severed flush, which as was previously suggested could alter scleral deformation. Hence, comparing these two results may not be appropriate without accounting for these main differences in method and eye geometry. Grytz et al. used thickness data in FE simulations to calculate the shear moduli and estimate stiffness. AD eyes were shown to have a higher shear modulus than those of ED [189]. The study by Fazio et al. found that age-related stiffening was significantly greater in the PP sclera for donors of AD compared to donors of ED [188]. Both these studies are consistent with our results where the slope of the tensile strain-pressure relationship of the ED eyes was significant while than that of AD eyes was not, suggesting that AD eyes deformed less with pressure (stiffer) compared to ED eyes.

All axon counts were within ranges that have been considered normal in different studies in the literature[224-231]. Both axon count and ONS volume were found to have significant effects on tensile and/or compressive strains in the different zones for at least one level of pressure. One possible concern may be that the biomechanical differences found between racioethnic groups could be due to racioethnic differences in ONS volume in our enucleated eyes. However, a statistical comparison on ONS volume (Figure 32) showed no significant differences between racioethnic groups that would explain differences in tensile and compressive strains. Additionally, it is noteworthy that a significant correlation existed between axon count and strains at 45 mmHg for normal non-glaucomatous eyes (Figure 6). The fact that this correlation was found in normal eyes suggests that axon loss may be a normal ongoing process in humans. It remains to be seen if this relationship plays a role in the predisposition of a person to glaucomatous damage. Furthermore, it seems that as proximity to the ONS decreases, the effect of axon count on strain diminishes (from ONS to PP to non-PP). It also seems that a loss of axons is associated with increased deformation in the optic nerve, especially at higher pressures.

While there is clinical evidence that both people of AD and HIS are more predisposed to developing glaucoma compared to people of ED, ocular biomechanical studies of AD and particularly HIS scleral shells are not common in the literature. Our results showed that those of HIS exhibited PP scleral tensile strains that were significantly different than those of ED at 15 mmHg. HIS tensile strains in the ONS region did not have a significant relationship with pressure, while ED eyes did. However, the behavior of tensile and compressive strains in both PP and non-PP scleral zones did not differ significantly between ED and HIS eyes. Preliminary results from our ongoing research (data not shown) suggest that ED eyes may also have significantly thicker sclera that of HIS eyes. The lack of consistency between HIS and AD strain patterns compared to ED suggests that the mechanism of higher prevalence of OAG in AD eyes could be different than that of HIS. More comprehensive studies are necessary to investigate possible alternative explanations to prevalence of ocular disease in both people of AD and HIS. In addition, it is important to note that these results show increasing pressure above 15 mmHg did not result in additional strain in the PP for AD eyes. This may be due to the nonlinear stress-strain material behavior presenting a more prominent strain-stiffening effect in that zone for AD eyes, which is considered a higher risk group. In future work, it would be interesting to explore if glaucomatous eyes demonstrate this type of behavior and how this may play a role in the incidence or progression of glaucoma. Another result of our study was that the ONS strains were much higher than the scleral strains at every IOP for all racioethnic groups (Figure 4). While it should be noted that the strains measured on the ONS in this study should not be interpreted as identical to those occurring in-vivo, this result strongly confirms that there is an IOP-dependent mechanical link between the peripapillary sclera and the dural sheath. This link may include bending modes of the sclera/dural sheath and may contribute to the overall biomechanical environment of the optic nerve head.

There are several limitations to the work presented here. While our study does provide ONS and PP scleral strain information, the reported strain is only surface strain and does not provide information regarding the mechanical environment at the LC, which has been shown to be an important region as it relates to RGC damage. On that note, the authors also wish to recommend that interpretations of the ONS strain results reported here not be construed as "optic nerve deformations" but rather as strains of mostly the sheath surrounding the optic nerve and a small portion of the optic nerve that was exposed during enucleation. It should be noted that all optic nerve stumps most likely were swollen in our experiments compared to in-vivo geometry. However, the well-controlled temperature and humidity environment and consistent preconditioning at all inflation pressures did not allow for any additional swelling during SDIC imaging. Unavoidable issues related to tissue edema and a somewhat non-physiological unconstrained severed nerve stump should serve as caution to the reader when interpreting these results. That being said, the fact that the presence (and volume) of the ONS volume did influence peripapillary scleral deformation indicate its inclusion may be important in future studies. Our study also focused entirely on assessing normal eyes and did not include glaucomatous eyes of any race or ethnicity. Future studies should be designed to study more thoroughly how glaucoma differentially affects posterior pole deformations in these populations, especially in regions close to the ONS. Furthermore, due to errors in nerve processing, our research group was unable to measure the axon counts for all the eyes used in S-DIC in this study. Therefore, the axon count relationship with strains is restricted to a subset of the eyes analyzed for strain. Lastly, the authors acknowledge the limited sample sizes used in this study and that later studies will be needed to draw more solid conclusions.

4.5 ACKNOWLEDGEMENTS

The authors would like to acknowledge the support of Alabama Eye Bank, Banner Sun Health Research, Donor Network of Arizona, Illinois Eye Bank, Michigan Eye Bank, and San Diego Eye Bank for their help in obtaining the human donor tissue. The authors would like to acknowledge Melanie Brucks and Scott Harrison for their statistical and post-processing contributions in this paper, and Thomas Cahir and Forest Danford for their contributions in the development of the axon counting method. Finally, the authors would like to thank Marianne Cilluffo at the University of California Los Angeles and Ben Christensen at the University of Utah for their help in nerve sample preparation and staining. Funding for this work was provided by the National Institute of Health (NIH) grant to JPVG (5R01EY020890). Research reported in this publication was supported by the National Eye Institute of the National Institutes of Health under award number R01EY020890. Additional support for E. Tamimi was also provided by the National Institute of Biomedical Imaging and Bioengineering under award number EB003392.

5.0 CHAPTER 5: DISSERTATION SUMMARY

5.1 SUMMARY OF RESULTS

5.1.1 Chapter 2: Specific Aim 1

Specific Aim 1: *Determine how glutaraldehyde-crosslinking duration modulates the biaxial mechanical properties and compliance of acellular gelatin/fibrinogen TEVGs in an effort to compliance match to porcine LADC and rat abdominal aorta*.

This study investigated the biaxial mechanical characterization of acellular electrospun glutaraldehyde vapor-crosslinked gelatin/fibrinogen cylindrical constructs, using a custom-made microbiaxial optomechanical device. Constructs crosslinked for 2, 8 and 24 hours are compared to mechanically-characterized porcine left anterior descending coronary (LADC) artery. The mechanical response data was used for constitutive modeling using a modified Fung strain energy equation. The results showed that constructs crosslinked for 2 and 8 hours exhibited circumferential and axial tangential moduli similar to that of the LADC. Furthermore, the 8-hour experimental group was the only one to compliance-match the LADC, with compliance values of 0.0006 ± 0.00018 mmHg $^{-1}$ and 0.00071 ± 0.00027 mmHg $^{-1}$, respectively. The results of this study show the feasibility of meeting mechanical specifications expected of native arteries through manipulating glutaraldehyde vapor crosslinking time.

5.1.2 Chapter 3: Specific Aim 2

Specific Aim 2: *Fabricate TEVGs composed of alternating layers of genipin-crosslinked porcine gelatin and human tropoelastin with varying polycaprolactone (PCL) percentages to compliance-match to rat aorta using an experimental/computational optimization approach.*

In this study, I developed an experimental/computational approach to fabricate an acellular biomimetic hybrid tissue engineered vascular graft composed of alternating layers of electrospun porcine gelatin/polycaprolactone (PCL) and human tropoelastin/PCL blends with the goal of compliance-matching to rat abdominal aorta, while maintaining specific geometrical constraints. Polymeric blends at three different gelatin:PCL (G:PCL) and tropoelastin:PCL (T:PCL) ratios (80:20, 50:50 and 20:80) were mechanically characterized individually using an in-house optomechanical biaxial tensile testing device. For each ratio, generated stress-strain data were used to develop a computational model that could predict the mechanical response of a polymeric blend at any G:PCL or T:PCL ratio within the experimental strain range. These predictive models were used as part of an optimization scheme that was implemented to determine the ratios of G:PCL and T:PCL and the thickness of the individual layers within a TEVG that would compliance match a target compliance value. Results showed that the average compliance value of the rat aorta was 0.00057 ± 0.00032 $mmHg^{-1}$. Based on these results, the optimization scheme was used to determine the parameters to make a hypocompliant, isocompliant, and hypercompliant graft with target compliance values of 0.00026, 0.00057 and 0.00088 $mmHg^{-1}$, respectively. Our experimental validation of the optimization demonstrated that the hypercompliant and isocompliant grafts were not statistically significant from their respective target compliance values (p-value = 0.37 and 0.89, respectively). However, the experimental compliance value of the hypocompliant graft was statistically significant than their target compliance value (p-value =

0.047). I have successfully demonstrated a design optimization scheme that can be used to fabricate multilayered and biomimetic vascular grafts with targeted geometry and compliance.

5.1.3 Chapter 4: Specific Aim 3

Specific Aim 3: *Quantify the strains of non-glaucomatous posterior scleral shells using sequential digital image correlation to evaluate the across three racioethnic groups: African descent (AD), European descent (ED), and Hispanic ethnicity(HIS), four regions: temporal (T), nasal (N), superior (S), and inferior (I), and three zones: peripapillary (PP) sclera, non-PP sclera, and optic nerve stumps at four intraocular pressure states: 5, 15, 30 and 45 mmHg.*

In this study, I quantified the biomechanical response of human posterior ocular tissues from donors of various racioethnic groups to better understand how differences in these properties may play a role in the racioethnic health disparities known to exist in glaucoma. Sequential digital image correlation (S-DIC) was used to measure the pressure induced surface deformations of 23 normal human posterior poles from three racioethnic groups: African descent (AD), European descent (ED), and Hispanic ethnicity (HIS). Regional in-plane principal strains were compared across three zones: the optic nerve stump (ONS), the peripapillary (PP) sclera, and non PP sclera. The PP scleral tensile strains were found to be lower for ED eyes compared to AD and HIS eyes at 15 mmHg (p-value = 0.024 and 0.039, respectively). The mean compressive strains were significantly higher for AD eyes compared to ED eyes at 15 mmHg (p-value = 0.018). I also found that the relationship between tensile strain and pressure was significant for those of ED and HIS eyes (p-value = <0.001 and 0.004, respectively), whereas it was not significant for those of AD (p-value = 0.392). The results suggested that, assuming glaucomatous nerve loss is caused by mechanical strains in the vicinity of the optic nerve head, the mechanism of increased glaucoma

prevalence may be different in those of AD versus HIS. The ONS strain analysis also suggested that it may be important to account for ONS geometry and material properties in future scleral biomechanical analysis.

5.2 FUTURE DIRECTIONS

Future studies should evaluate burst pressure and suture retention of all vascular grafts as a measure of durability *in vivo*. The effects of cell proliferation and remodeling on the compliance of these grafts should be determined. These remodeling mechanisms should be investigated in greater details using *ex vivo* cell cultures seeded onto our grafts in our current custom-made bioreactors setup, which have been designed to be imaged intravitally using multiphoton imaging. Experiments could be designed to investigate the biodegradability and biocompatibility of our materials using vascular smooth muscle culture.

Blood compatibility and thrombogenicity remain important factors for these constructs and should be evaluated. To accommodate this concern, possible modifications to the constructs could include surface modification to the lumen of the construct, which could be made to be hydrophilic and inhibit protein absorption. Endothelialization of the lumen is another method make the constructs more anti-thrombogenic. Studies performed by my colleague Catalina Ardila has shown that the addition of a collagen IV/fibronectin blend to the lumen promoted the development of an endothelial monolayer on electrospun gelatin fibers constructs. These methods could be used to promote both *ex vivo* and *in situ* endothelialization.

For full clinical translational use of the grafts, one must consider issues related to potential toxicities of the crosslinking agent used in this study. While Specific Aim 2 used an alternative crosslinker (genipin) to replace glutaraldehyde, future studies may be able to still utilize

glutaraldehyde for crosslinking grafts by detoxifying the grafts with glycine [105]. Other chemical crosslinkers may be utilized that do not have the same cytotoxicity and calcification effect of glutaraldehyde. For example, one study by Carrabba et al. has recently performed *in vivo* studies using electrospun gelatin constructs crosslinked with 3-glycidyloxy-propyl-trimethoxy-silane (GPTMS) [232], which showed good biocompatibility and implant durability.

The immunogenicity and inflammation due to the presence of these grafts are another set of concerns. One possible solution for future studies is to utilize the natural biopolymers of the animal model to reduce the immunoresponse and possibly prevent inflammation. It may also be helpful to investigate the mechanism of *in vivo* reactions so as to modify the material appropriately to prevent undesired reactions.

The ABAQUS finite element model used in Specific Aim 2 was an axisymmetric element model undergoing a pressurization at zero axial load. This type of simulation largely only utilized the circumferential stress-strain input data. Hence, the optimization scheme did not account for axial properties. This was confirmed experimentally, as all optimized grafts had qualitatively higher tensile strength than that of rat aorta. Future studies could aim to match the rat aorta in both circumferential and axial directions. This could be performed by developing a three-dimensional finite element model geometry pressurized at various axial stretches. Matching native axial properties would contribute to less graft failure through improved suture retention. In addition, all optimized grafts demonstrated coupling between the circumferential and axial directions and therefore, matching properties in the axial direction may contribute to further matching them in the circumferential direction as well.

Initial preliminary results in our laboratory demonstrated that tropoelastin/gelatin electrospun constructs were less stiff and more elastic than gelatin construct, if both were

crosslinked with glutaraldehyde for the same duration. In Specific Aim 2, I decided to use genipin for concerns regarding cytotoxicity and *in vivo* calcification. I was expecting to see that the tropoelastin:PCL material be more elastic and less stiff than the gelatin:PCl material with the same protein:PCL ratio. However, the opposite was true. This could be due to a difference in crosslinking mechanism between glutaraldehyde and genipin. Future studies could investigate different types of natural and chemical crosslinking agents to better utilize the inherent elastic properties of tropoelastin.

The experimental compliance measures of the hypocompliant grafts were different than their target values. This could be due to the low strain range for stress-strain data for low protein gelatin:PCL and tropoelastin:PCL ratios. Future studies could expand the availability of circumferential stress-strain data by pressurizing all constructs beyond 120 mmHg, which was set as the maximum intraluminal pressure during mechanical tests. Additionally, axial stress-strain data could be generated by stretching the constructs axially beyond 25%, which was set as the maximum axial stretch. This would improve the predictive model, Fung model fitting and generate more accurate compliance values.

Another method to improve the accuracy of the optimization scheme in Specific Aim 2 is by increasing the resolution of the fabrication thickness. This could be done either by reducing the number of overall layers or upgrading the equipment to enable real-time thickness measurement. Preliminary calibration curves between dispensed volume and construct thickness would be helpful to more accurately fabricate the correct thickness of any layer. This would remove any errors associated with the interpolation method in determining layer thickness as a function of polymeric solution dispensed volume.

In regards to ocular biomechanics in Specific Aim 3, future studies could expand our current racioethnic biomechanical comparison to include diseased glaucomatous eyes in each racioethnic group. This could enable us to more closely relate biomechanical properties of racioethnic groups that are at risk of ocular disease to that of eyes that are more prone to experience that particular ocular disease. Future studies can also relate how the biomechanics of the posterior sclera may be related to promotion of cellular pathways that increase ECM deposition and cause additional stress on the retinal ganglion nerves, which may lead to their degeneration. Additionally, future studies by our group will combine geometry data collected via micro computed tomography with strain data collected from this study to develop an inverse finite element model, which will investigate if the strain differences quantified in this study correspond to true mechanical property differences. In addition, our research group is currently using 3D digital image correlation and multiphoton images of the lamina cribrosa to determine the biomechanics of the microstructure of the LC, which is directly implicated in the onset of glaucoma.

Finally, by using S-DIC in Specific Aim 3, we was able to capture the mechanical response of the posterior eyes being pressurized. With the appropriate setup and equipment, this same method could also be applied to the characterization of tissue engineered vascular grafts. In the analysis in both Specific Aims 1 and 2, the microbiaxial optomechanical device methods relied on the assumption of cylindrical axisymmetry, which simplifies the circumferential strains to be uniform throughout the graft. Future studies could utilize S-DIC to provide more three-dimensional detail to the biomechanical response of both our fabricated constructs and native tissue. Multiphoton imaging can also be used to capture deformations in construct microstructure enabling us to gather more biomechanical information, like the relationship between fiber orientation and mechanical behavior.

5.3 DISSERTATION CONCLUSIONS

My study for Specific Aim 1 is the first to quantify and compare the anisotropic behavior of electrospun biopolymers to that of native porcine coronary tissue. This was accomplished using the custom-made microbiaxial optomechanical tensile testing device that evaluated the anisotropic cylindrical geometries using tubular biaxial protocols, which serves as a more comprehensive evaluation of the mechanical suitability of electrospun biopolymer constructs for use as vascular grafts. The hypothesis for this aim was that there is a glutaraldehyde crosslinking duration that would yield electrospun gelatin/fibrinogen tubular constructs with mechanical properties similar to native vessels. The results indicated that glutaraldehyde crosslinking increased the stiffness and density of the electrospun gelatin/fibrinogen constructs. Therefore, glutaraldehyde-crosslinking could be used as a means of modulating the material properties of constructs to compliant-match to a specific compliance value. Based on this analysis, my hypothesis for this aim was supported.

My study for Specific Aim 2 is one of the first research efforts to use a computational/ experimental optimization scheme to fabricate a multilayered biomimetic vascular graft using protein analogues to elastin and collagen. These methods contribute towards the design of a functional and clinically translatable tissue engineered vascular graft. My hypothesis for this aim was that electrospun TEVGs composed of alternating layers of PCL-enforced genipin-crosslinked gelatin and tropoelastin can be compliance matched to rat aorta by varying the percentage of PCL in each layer. The results demonstrated that grafts can be designed to compliance match to a wide range of compliance values. I have shown that we can tune the mechanical properties of our hybrid synthetic/protein grafts by varying the ratio of protein to synthetic polymer using an optimization scheme that can be used to target a specific compliance value while considering geometry. Based on my analysis, my hypothesis for this aim was supported.

My study for Specific Aim 3 is the first to determine strains for all zones and regions of the posterior eyes of donors of Hispanic ethnicity. Overall, I found that the Hispanic ethnicity peripapillary scleral tensile strain relationship with pressure were more similar to those of European descent than African descent for tensile strains. This study is also the first to map the strain behavior of the human optic nerve stump for any racioethnic group using sequential digital image correlation. This study was also the first to find a significant relationship between tensile and compressive strains and optic nerve stump volume and axon count. This shows that studying the strains of optic nerve stump, which serves as the sheath for nerves, may be an important consideration in biomechanical evaluation of the posterior pole. The results in this study indicate that keeping optic nerve stumps attached to their scleral shells, while accounting for volume and axon count, may be necessary to conduct a more complete ocular biomechanical analysis. My hypothesis for this aim was that differences in the mechanical properties of the posterior sclera exist as a function of racioethnicity. The results showed that there were biomechanical differences between the eyes of all three racioethnic groups, which may explain the disparity in ocular disease between these groups. Based on this analysis, the hypothesis for this aim was supported.

There are currently no clinically translatable compliance matched and biologically functional small diameter TEVG. I expect that the work presented in this dissertation will contribute to the development of a TEVG that could remain compliance matched post implantation, while displaying excellent antithrombogenic properties and minimal intimal hyperplasia when used in both a small and large preclinical animal model.

APPENDIX A

PREDICTIVE STRESS-STRAIN MODEL

```
function [Szz_predicted, STT_predicted, Ezz_predicted, ETT_predicted] =
predictive_model_simple(Szz_average,STT_average,ETTNew, EzzNew,
definition_matrix, desired_level,pr)
global root_folder
%This function interprolates using a second degree Lagrangian polynomial
function

%First we define the N ratios
x0 = definition_matrix(1);
x1 = definition_matrix(2);
x2 = definition_matrix(3);

x = desired_level;

N1 = (x-x0)*(x-x2)/((x1-x0)*(x1-x2));
N2 = (x-x1)*(x-x2)/((x0-x1)*(x0-x2));
N3 = (x-x1)*(x-x0)/((x2-x1)*(x2-x0));


Szz_predicted = N1*Szz_average(:,:,2,pr) + N2*Szz_average(:,:,1,pr) +
N3*Szz_average(:,:,3,pr);
STT_predicted = N1*STT_average(:,:,2,pr) + N2*STT_average(:,:,1,pr) +
N3*STT_average(:,:,3,pr);
ETT_predicted = N1*ETTNew{2,pr} + N2*ETTNew{1,pr} + N3*ETTNew{3,pr};
Ezz_predicted = N1*EzzNew{2,pr} + N2*EzzNew{1,pr} + N3*EzzNew{3,pr};


End
```

APPENDIX B

OPTIMIZATION SCHEME MATLAB CODE

```
iter=1;
options = optimset('TolFun',1e-1,'TolX',1e-1,'PlotFcns',@optimplotfval);
k = 0;
% for j=[80 100 12]
min_total_thickness = 60;
max_total_thickness = 100;
% k=k+1
for i = [6]
initial_number_of_layers = i*2;
ti_initial = ones(1,initial_number_of_layers);  %Initial guess for thickness
of each material (m)
per_initial_gelatin = 0;
per_initial_tropo = 0;



T_thickness_max = 5;
T_thickness_min = 5;

total_T_thickness_min = i*T_thickness_min;
total_T_thickness_max = i*T_thickness_max;
G_thickness_min = (min_total_thickness - total_T_thickness_min)/i;
G_thickness_max = (max_total_thickness - total_T_thickness_max)/i;

odd_numbers = [1 3 5 7 9 11 13 15];
even_numbers = [2 4 6 8 10 12 14 16];

odd_numbers = odd_numbers(1:i);
even_numbers = even_numbers(1:i);

global t_max
t_max = ones(1,length(ti_initial));
t_max(odd_numbers) = G_thickness_max*1e-6*t_max(odd_numbers);
t_max(even_numbers) = T_thickness_max*1e-6*t_max(even_numbers);
% t_max = 1e-6*[40 40];
```

```
global t_min
t_min = ones(1,length(ti_initial));
t_min(odd_numbers) = G_thickness_min*1e-6*t_min(odd_numbers);
t_min(even_numbers) = T_thickness_min*1e-6*t_min(even_numbers);
% t_min = 1e-6*[10 10];

ti_max = 1*ones(1,length(ti_initial)); %Upper bounds on layer thickness
ti_min = 1*ones(1,length(ti_initial)); %Lower bounds

%for gelatin
ti_max(odd_numbers) = 1*ti_max(odd_numbers);
ti_min(odd_numbers) = 0*ti_min(odd_numbers);
ti_initial(odd_numbers) = 0.5*ti_initial(odd_numbers);
%for tropo
ti_max(even_numbers) = 1*ti_max(even_numbers);
ti_min(even_numbers) = 1*ti_min(even_numbers);
ti_initial(even_numbers) = 1*ti_initial(even_numbers);


global gelatin_max
gelatin_max = 80;
global gelatin_min
gelatin_min = 20;
global tropo_max
tropo_max = 80;
global tropo_min
tropo_min = 20;

global comp


per_gelatin_max = 1;
per_gelatin_min = 0;
per_tropo_max = 1;
per_tropo_min = 0;

target_comp = 5e-5;



results{i} = fminsearchbnd(@compliance_gel_tropo_,[ti_initial,
per_initial_gelatin, per_initial_tropo],[ti_min, per_gelatin_min,
per_tropo_min],[ti_max, per_gelatin_max, per_tropo_max],options,target_comp)
compliance{i} = comp


end
toc
```

APPENDIX C

ABAQUS-MATLAB COUPLED OPTIMIZATION ROUTINE

```
function f = compliance_gel_tropo(t,compliance_to_match)



global gelatin_max
global gelatin_min
global tropo_max
global tropo_min
global t_max
global t_min
global comp



t


t_i = t(1:length(t)-2);  %Thickness of each layer

t_delta = t_max - t_min;
t_i = t_min + t_i.*t_delta;


P_gelatin = t(length(t)-1); %percentage of gelatin
P_gelatin_delta = gelatin_max - gelatin_min;
P_gelatin = gelatin_min + P_gelatin.*P_gelatin_delta;

P_tropo = t(length(t)); %percentage of tropo
P_tropo_delta = tropo_max - tropo_min;
P_tropo = tropo_min + P_tropo.*P_tropo_delta;



L = 0.00005;  %Length of tube (m)
```

```
dia = 0.001;  %Inner Diameter of tube (m)

n = (length(t_i))/2; %Number of layers, each layer consists one layer of
material 1 and one layer of material 2
l =5;  %Number of elements accross thickness
% e = round(l*L/min(t_i)) %Number of elements in the direction of length
e=5;
ti = sum(t_i);  %Total initial thickness
E = 2*e*n*l;  %Total number of elements
N = (2*n*l+1)*(e+1);  %Total number of nodes
h = L/e;  %Height of each element
te_i = t_i/l;   %Thickness of each element within each layer


%Create mesh grid in ETT-EZZ plane that doesn't extrapolate



load('C:\Users\ehab\Documents\AIM2\best_variables.mat')

P(1) = P_gelatin;
P(2) = P_tropo;


[Szz_predicted_T,STT_predicted_T,  Ezz_predicted_T, ETT_predicted_T] =
predictive_model_simple(Szz_average,STT_average,ETTNew, EzzNew, [20 50 80],
P(1),2);
[Szz_predicted_G,STT_predicted_G,  Ezz_predicted_G, ETT_predicted_G] =
predictive_model_simple(Szz_average,STT_average,ETTNew, EzzNew, [20 50 80],
P(2),1);

%These are settings for the fmincon function below
            xz = [1 1 1 1];

            lb = [0,0,0,0]; %Lower limit: this says that the constants have
to be positive and more than zero
            ub = [inf,inf,inf,inf]; %Upper limit


            %Objective function minimization: fitting to the fung model
             options = optimset('MaxFunEvals',1e200,'MaxIter',1e200, 'TolX',
1e-10);

            mode = 'both';
            f=@(x)objfung(x,Ezz_predicted_G, Szz_predicted_G,
ETT_predicted_G, STT_predicted_G,mode); %define parameter function handle
that allows code to pass additional parameters to merit function

[fitvars,FVAL,EXITFLAG,OUTPUT]=fmincon(f,xz,[],[],[],[],lb,ub,[],options);
            constants_predicted(1) = fitvars(1);
            constants_predicted(2) = fitvars(2);
            constants_predicted(3) = fitvars(3);
            constants_predicted(4) = fitvars(4);
```

```
            b(1,4) = constants_predicted(1)*1000;
            b(1,1) = constants_predicted(2);
            b(1,2) = constants_predicted(3);
            b(1,3) = constants_predicted(4);

             xz = [1 1 1 1];

            lb = [0,0,0,0]; %Lower limit: this says that the constants have
to be positive and more than zero
            ub = [inf,inf,inf,inf]; %Upper limit


            %Objective function minimization: fitting to the fung model
             options = optimset('MaxFunEvals',1e200,'MaxIter',1e200, 'TolX',
1e-10);

            mode = 'both';
             f=@(x)objfung(x,Ezz_predicted_T, Szz_predicted_T,
ETT_predicted_T, STT_predicted_T,mode); %define parameter function handle
that allows code to pass additional parameters to merit function

[fitvars,FVAL,EXITFLAG,OUTPUT]=fmincon(f,xz,[],[],[],[],lb,ub,[],options);
            constants_predicted(1) = fitvars(1);
            constants_predicted(2) = fitvars(2);
            constants_predicted(3) = fitvars(3);
            constants_predicted(4) = fitvars(4);


            b(2,4) = constants_predicted(1)*1000;
            b(2,1) = constants_predicted(2);
            b(2,2) = constants_predicted(3);
            b(2,3) = constants_predicted(4);



            % Surface model fit for material 1 GELATIN
mat_prop1 = [ 1e-20, 1e-20, b(1,2), 1e-20, b(1,3), b(1,1), 1e-20, 1e-20];
mat_prop2 = [1e-20, b(1,4), 0];

%Material Properties of Material 2 T mixture
mat_prop12 = [1e-20, 1e-20, b(2,2), 1e-20, b(2,3), b(2,1), 1e-20, 1e-20];
mat_prop22 = [1e-20, b(2,4), 0];

nodes = zeros(N,3);
%First column of node matrix corresponds to node number
for i=1:N
    nodes(i,1)=i;
end

%Define horizontal coordinate of each node
for i=1:2*n
    if mod(i,2) ==1
        for j=1:l
```

```
            for k=j+(i-1)*l:2*n*l+1:e*(2*n*l+1)+j+(i-1)*l
                nodes(k,2) = dia/2 + sum(t_i(1:i-1)) + (j-1)*te_i(i);
            end
        end
    elseif mod(i,2) == 0
        for j=1:l
            for k=j+(i-1)*l:2*n*l+1:e*(2*n*l+1)+j+(i-1)*l
                nodes(k,2) = dia/2 + sum(t_i(1:i-1)) + (j-1)*te_i(i);
            end
        end
    end
end

for i=2*n*l+1:2*n*l+1:(2*n*l+1)*(e+1)
    nodes(i,2) = dia/2+ti;
end

%Define vertical coordinate of each node
for i=1:e+1
    for j = 1+(i-1)*(2*n*l+1):i*(2*n*l+1)
        nodes(j,3) = h*(i-1);
    end
end

%Define elements
elements = zeros(E,5);
%First column of element matrix corresponds to element number
for i=1:E
    elements(i,1)=i;
end

%Assign nodes to elements, starting at the bottom left and moving
%counter-clockwise
for i=1:E/(2*n*l)
    elements(i,2) = 1+(i-1)*(2*n*l+1);
    elements(i,3) = elements(i,2)+1;
    elements(i,4) = elements(i,3)+2*n*l+1;
    elements(i,5) = elements(i,4)-1;
end
for i=E/(2*n*l)+1:E
    elements(i,2:5) = elements(i-e,2:5)+1;
end

%Node Set assigned to material 1
nset1 = zeros(e+1,l+1);
for k=1:n
    for i=1:e+1
        for j=1:l+1
            nset1(i+(k-1)*(e+1),j) = j+(i-1)*(2*n*l+1)+2*l*(k-1);
        end
    end
end

%Element Set assigned to material 1
el_set1 = zeros(n*l,3);
for j=1:n
```

```
    for i=1:l
        el_set1(i+(j-1)*l,1:2) = [1+(i-1)*e+2*e*l*(j-1),i*e+2*e*l*(j-1)];
    end
end
el_set1(:,3) = 1;

%Node Set assigned to material 2
nset2 = zeros(e+1,l+1);
nset2 = nset1+l;

%Element Set assigned to material 2
el_set2 = zeros(n*l,3);
el_set2 = el_set1+e*l;
el_set2(:,3) = 1;

%Node Set along top and bottom boundary
nset3=zeros(2,3);
nset3(:,1) = [1; (2*n*l+1)*e+1];
nset3(:,2) = [2*n*l+1; N];
nset3(:,3) = [1; 1];

%Element Set along top and bottom boundary
el_set3 = zeros(2*n*l,2);
for i=1:2*n*l
    el_set3(i,1) = (i-1)*e+1;
    el_set3(i,2) = (i-1)*e+e;
end

%Node along inner boundary
n_inner = 1+(2*n*l+1)*round(e/2);
%Node along outer boundary
n_outer = (2*n*l+1)+(2*n*l+1)*round(e/2);

%Element Set for pressurized surface
el_set4 = [1, e, 1];

%Create an .inp file for the above mesh
fID = fopen('TEVG120.inp','w');
fclose(fID);
fID = fopen('TEVG120.inp','a');

fprintf(fID,'*Heading\r\n');
fprintf(fID,'** Job name: TEVG120 test\r\n');
fprintf(fID,'** Generated by: Abaqus/CAE Student Edition 6.13-2\r\n');
fprintf(fID,'*Preprint, echo=NO, model=NO, history=NO, contact=NO\r\n');
fprintf(fID,'**\r\n');
fprintf(fID,'** PARTS\r\n');
fprintf(fID,'**\r\n');
fprintf(fID,'*Part, name=Part-1\r\n');
fprintf(fID,'*End Part\r\n');
fprintf(fID,'**  \r\n');
fprintf(fID,'**\r\n');
fprintf(fID,'** ASSEMBLY\r\n');
fprintf(fID,'**\r\n');
fprintf(fID,'*Assembly, name=Assembly\r\n');
```

```
fprintf(fID,'**  \r\n');
fprintf(fID,'*Instance, name=Part-1-1, part=Part-1\r\n');
fprintf(fID,'*Node\r\n');
%Insert nodes
dlmwrite('TEVG120.inp',nodes,'-append','newline','pc');

fprintf(fID,'*Element, type=CAX4RH\r\n');
%Insert elements
dlmwrite('TEVG120.inp',elements,'-append','newline','pc');

fprintf(fID,'*Nset, nset=Set-1\r\n');
%Insert nset1 which contains nodes belonging to material 1
dlmwrite('TEVG120.inp',nset1,'-append','newline','pc');

fprintf(fID,'*Elset, elset=Set-1, generate\r\n');
%Insert el_set1 which contains elements belonging to material 1
dlmwrite('TEVG120.inp',el_set1,'-append','newline','pc');

fprintf(fID,'*Nset, nset=Set-2\r\n');
%Insert nset2 which contains nodes belonging to material 2
dlmwrite('TEVG120.inp',nset2,'-append','newline','pc');

fprintf(fID,'*Elset, elset=Set-2, generate\r\n');
%Insert el_set2 which contains elements belonging to material 2
dlmwrite('TEVG120.inp',el_set2,'-append','newline','pc');

fprintf(fID,'*Orientation, name=Ori-1\r\n');
fprintf(fID,'1., 0., 0., 0., 1., 0.\r\n');
fprintf(fID,'3, 0.\r\n');
fprintf(fID,'** Section: Section-2\r\n');
fprintf(fID,'*Solid Section, elset=Set-2, orientation=Ori-1,
material=Material-2\r\n');
fprintf(fID,',\r\n');
fprintf(fID,'** Section: Section-1\r\n');
fprintf(fID,'*Solid Section, elset=Set-1, orientation=Ori-1,
material=Material-1\r\n');
fprintf(fID,',\r\n');
fprintf(fID,'*End Instance\r\n');
fprintf(fID,'**  \r\n');
fprintf(fID,'*Nset, nset=Set-1, instance=Part-1-1, generate\r\n');
%Insert nset3 which contains nodes along top and bottom
dlmwrite('TEVG120.inp',nset3,'-append','newline','pc');

fprintf(fID,'*Elset, elset=Set-1, instance=Part-1-1\r\n');
%Insert el_set3 which contains elements along top and bottom
dlmwrite('TEVG120.inp',el_set3,'-append','newline','pc');

fprintf(fID,'*Elset, elset=_Surf-1_S4, internal, instance=Part-1-1,
generate\r\n');
%Insert el_set4, which contains elements along the pressurized surface
dlmwrite('TEVG120.inp',el_set4,'-append','newline','pc');

fprintf(fID,'*Surface, type=ELEMENT, name=Surf-1\r\n');
fprintf(fID,'_Surf-1_S4, S4\r\n');
```

```
fprintf(fID,'*Nset, nset=inner_node, instance=Part-1-1\r\n');
dlmwrite('TEVG120.inp',n_inner,'-append','newline','pc');
fprintf(fID,'*Nset, nset=outer_node, instance=Part-1-1\r\n');
dlmwrite('TEVG120.inp',n_outer,'-append','newline','pc');

fprintf(fID,'*End Assembly\r\n');
fprintf(fID,'** \r\n');
fprintf(fID,'** MATERIALS\r\n');
fprintf(fID,'** \r\n');
fprintf(fID,'*Material, name=Material-1\r\n');
fprintf(fID,'*Anisotropic Hyperelastic, fung-orthotropic\r\n');
%insert material properties
%Mat 1
dlmwrite('TEVG120.inp',mat_prop1,'-append','newline','pc');
dlmwrite('TEVG120.inp',mat_prop2,'-append','newline','pc');
%Mat 2
fprintf(fID,'*Material, name=Material-2\r\n');
fprintf(fID,'*Anisotropic Hyperelastic, fung-orthotropic\r\n');
dlmwrite('TEVG120.inp',mat_prop12,'-append','newline','pc');
dlmwrite('TEVG120.inp',mat_prop22,'-append','newline','pc');
fprintf(fID,'** ----------------------------------------------------------------
---\r\n');
fprintf(fID,'** \r\n');
fprintf(fID,'** STEP: Step-1\r\n');
fprintf(fID,'** \r\n');
fprintf(fID,'*Step, name=Step-1, nlgeom=YES, inc=960\r\n');
fprintf(fID,'*Static\r\n');
% fprintf(fID,'0.00125, 1.2,1.2e-6, 0.00125,\r\n');
fprintf(fID,'0.00125, 1.2, 1.2e-100, 0.00125,\r\n');
fprintf(fID,'** \r\n');
fprintf(fID,'** BOUNDARY CONDITIONS\r\n');
fprintf(fID,'** \r\n');
fprintf(fID,'** Name: BC-1 Type: Displacement/Rotation\r\n');
fprintf(fID,'*Boundary\r\n');
fprintf(fID,'Set-1, 2, 2\r\n');
fprintf(fID,'** \r\n');
fprintf(fID,'** LOADS\r\n');
fprintf(fID,'** \r\n');
fprintf(fID,'** Name: Load-1   Type: Pressure\r\n');
fprintf(fID,'*Dsload\r\n');
fprintf(fID,'Surf-1, P, 15998.\r\n');
fprintf(fID,'** \r\n');
fprintf(fID,'** OUTPUT REQUESTS\r\n');
fprintf(fID,'** \r\n');
fprintf(fID,'*Restart, write, frequency=0\r\n');
fprintf(fID,'** \r\n');
fprintf(fID,'** FIELD OUTPUT: F-Output-1\r\n');
fprintf(fID,'** \r\n');
fprintf(fID,'*Output, field, variable=PRESELECT\r\n');
fprintf(fID,'** \r\n');
fprintf(fID,'** HISTORY OUTPUT: H-Output-1\r\n');
fprintf(fID,'** \r\n');
fprintf(fID,'*Output, history, variable=PRESELECT\r\n');
fprintf(fID,'*Node print, nset=inner_node, frequency=560\r\n');
fprintf(fID,'U1, COORD\r\n');
fprintf(fID,'*Node print, nset=outer_node, frequency=560\r\n');
fprintf(fID,'U1, COORD\r\n');
```

```
fprintf(fID,'*End Step\r\n');
fclose(fID);
%Run the job, generate an ODB
dos('abaqus job=TEVG120job inp=TEVG120.inp');

pause(10)
% while exist('TEVG1203job.023') == 0
%     pause(1)
% end
while exist('TEVG120job.023')==2
    pause(2)
end
try
  fid = fopen('TEVG120job.dat', 'r');
C = textscan(fid, '%s', 'Delimiter', ' ','MultipleDelimsAsOne',1);
fclose(fid);
D = strfind(C{1}, 'MAXIMUM');
rows = find(~cellfun('isempty', D));
%
% DD = strfind(C{1}, 'INCREMENT');
% rows_b = find(~cellfun('isempty', DD));
%  max_increment= C{1}(rows_b(length(rows_b))-4);




O1 = C{1}(rows(4)+2);

O2 = C{1}(rows(6)+2);

% inner_disp1 = str2num(I1{1});
 OD70 = 2*str2num(O1{1});
% inner_disp2 = str2num(I2{1});
OD120 = 2*str2num(O2{1})

 del_P = 50;
%
 comp = (OD120-OD70)/(OD70*del_P)
 f = abs(compliance_to_match-comp)
catch

    comp=NaN
     f = NaN

end

%************************************************************
End
```

APPENDIX D

PRELIMINARY CROSSLINKING EXPERIMENTS

The following graphs represent preliminary mechanical testing of different crosslinking methods that we were investigating to use on our constructs. They compare genipin to GLUT and UV at different crosslinking times.

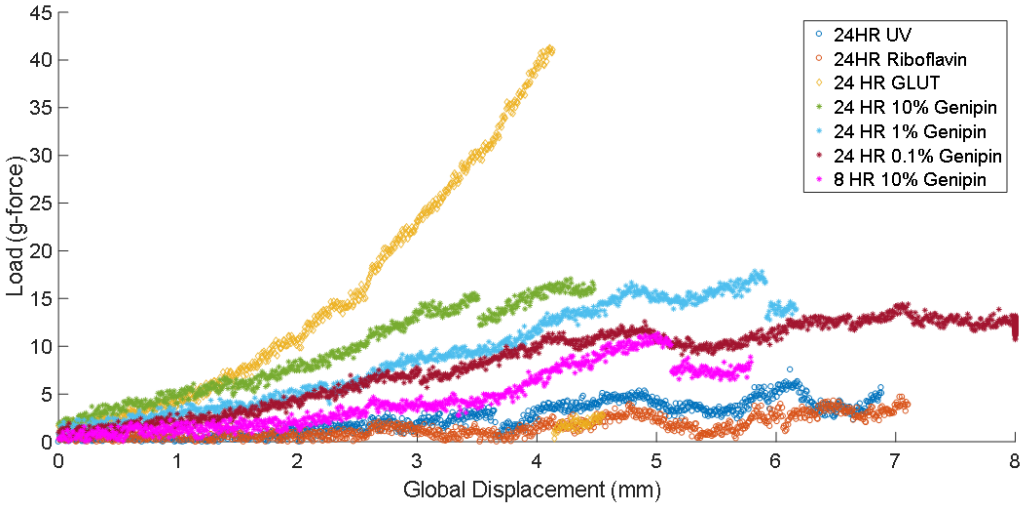

Figure 34. Preliminary load versus displacement data for different types of gelatin crosslinking

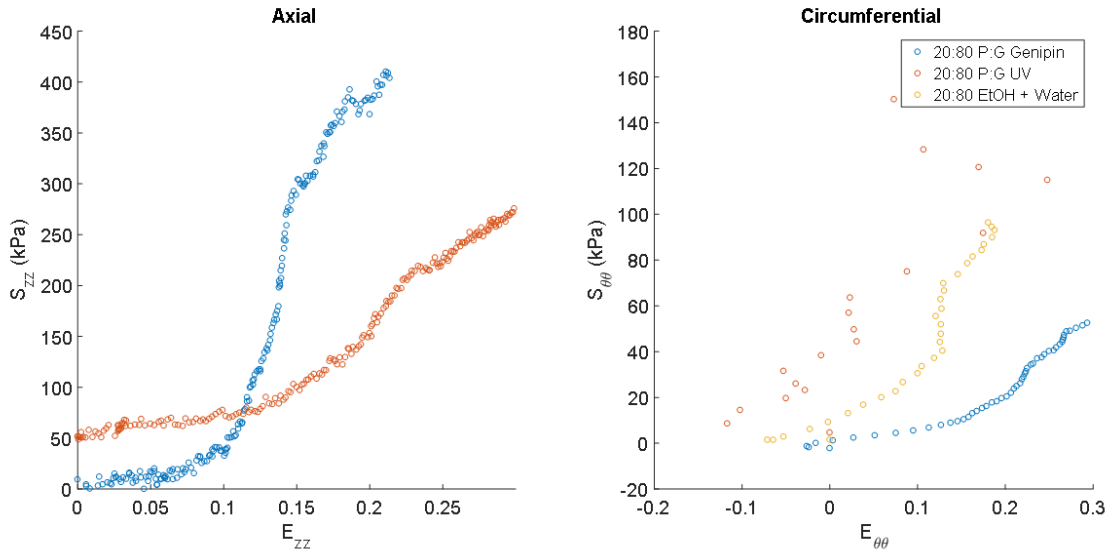

Figure 35. Preliminary axial and circumferential stress-strain data for different crosslinking methods on 20:80 PCL:gelatin constructs

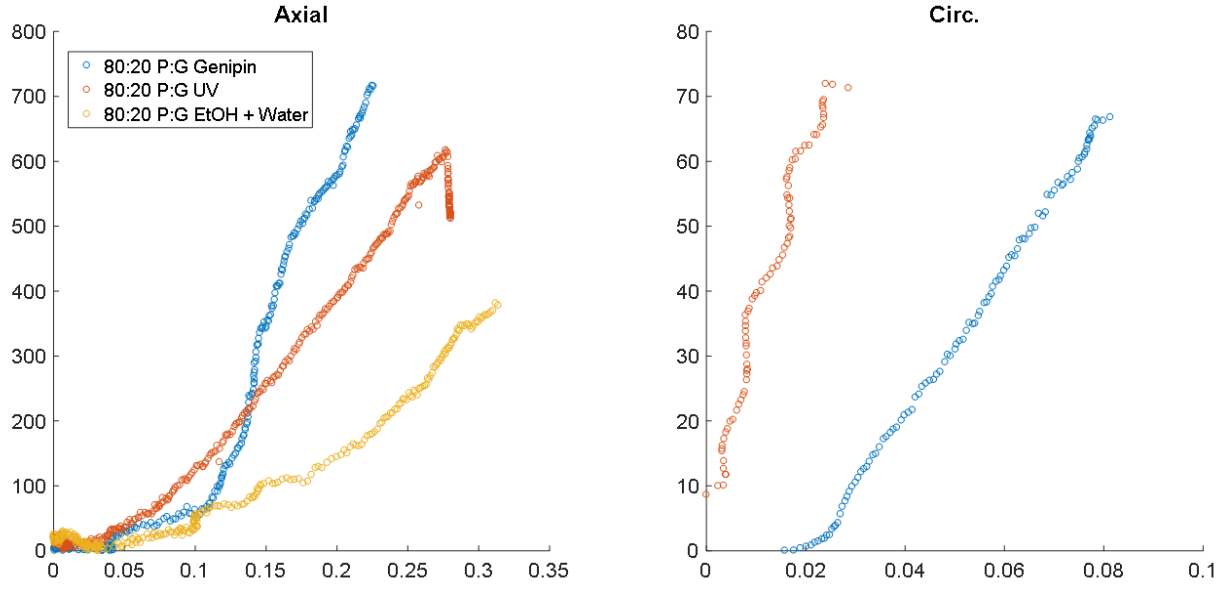

Figure 36. Preliminary axial and circumferential stress-strain data for different crosslinking methods on 80:20 PCL:gelatin constructs

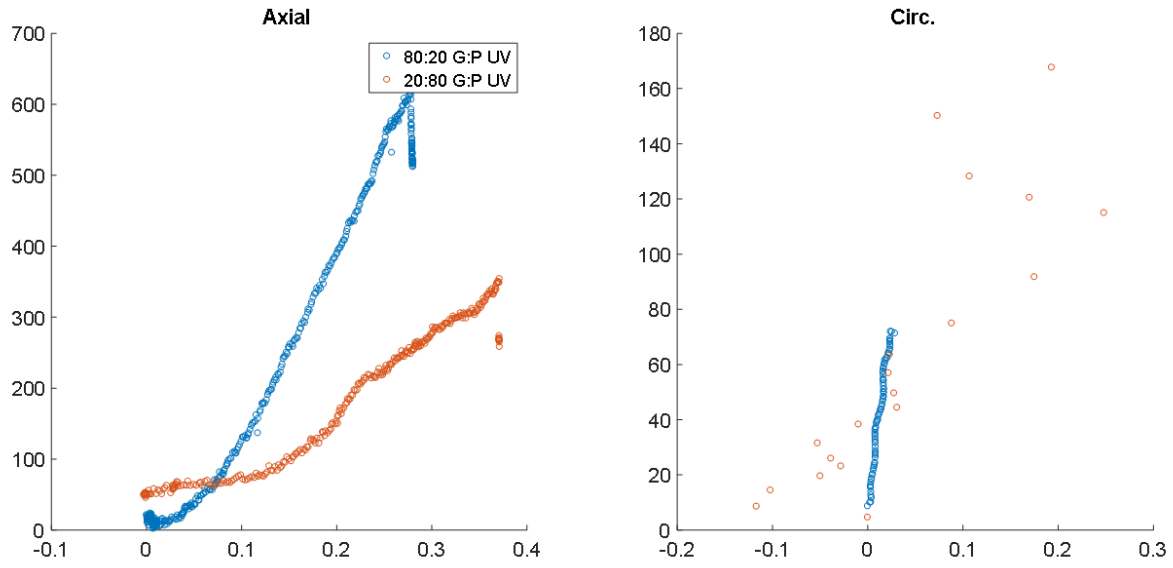

Figure 37. Preliminary axial and circumferential stress-strain data comparison between 80:20 PCL:gelatin and 20:80 PCL:gelatin constructs crosslinked with UV

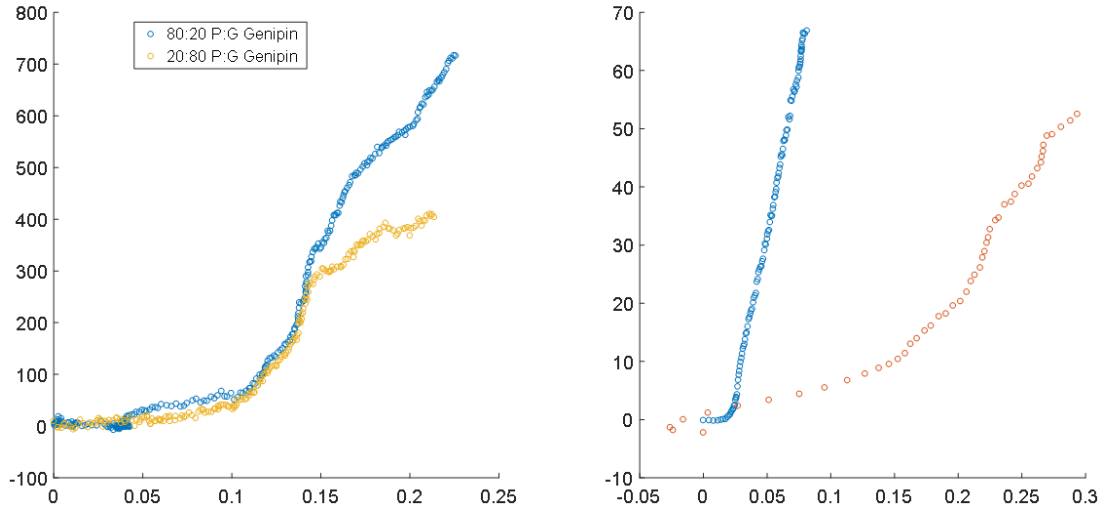

Figure 38. Preliminary axial and circumferential stress-strain data comparison between 80:20 PCL:gelatin and 20:80 PCL:gelatin constructs crosslinked with genipin

BIBLIOGRAPHY

[1] Benjamin, E. J., Blaha, M. J., Chiuve, S. E., Cushman, M., Das, S. R., Deo, R., de Ferranti, S. D., Floyd, J., Fornage, M., Gillespie, C., Isasi, C. R., Jiménez, M. C., Jordan, L. C., Judd, S. E., Lackland, D., Lichtman, J. H., Lisabeth, L., Liu, S., Longenecker, C. T., Mackey, R. H., Matsushita, K., Mozaffarian, D., Mussolino, M. E., Nasir, K., Neumar, R. W., Palaniappan, L., Pandey, D. K., Thiagarajan, R. R., Reeves, M. J., Ritchey, M., Rodriguez, C. J., Roth, G. A., Rosamond, W. D., Sasson, C., Towfighi, A., Tsao, C. W., Turner, M. B., Virani, S. S., Voeks, J. H., Willey, J. Z., Wilkins, J. T., Wu, J. H., Alger, H. M., Wong, S. S., and Muntner, P., 2017, "Heart Disease and Stroke Statistics—2017 Update: A Report From the American Heart Association," Circulation.

[2] Ferrari, E. R., and von Segesser, L. K., 2006, "Arterial grafting for myocardial revascularization: how better is it?," Current opinion in cardiology, 21(6), pp. 584-588.

[3] Goldman, S., Zadina, K., Moritz, T., Ovitt, T., Sethi, G., Copeland, J. G., Thottapurathu, L., Krasnicka, B., Ellis, N., Anderson, R. J., and Henderson, W., 2004, "Long-term patency of saphenous vein and left internal mammary artery grafts after coronary artery bypass surgery: Results from a Department of Veterans Affairs Cooperative Study," Journal of the American College of Cardiology, 44(11), pp. 2149-2156.

[4] Hess, C. N., Lopes, R. D., Gibson, C. M., Hager, R., Wojdyla, D. M., Englum, B. R., Mack, M., Califf, R., Kouchoukos, N. T., Peterson, E. D., and Alexander, J. H., 2014, "Saphenous Vein Graft Failure after Coronary Artery Bypass Surgery: Insights from PREVENT IV," Circulation.

[5] Kurobe, H., Maxfield, M. W., Breuer, C. K., and Shinoka, T., 2012, "Concise review: tissue-engineered vascular grafts for cardiac surgery: past, present, and future," Stem cells translational medicine, 1(7), pp. 566-571.

[6] Kannan, R. Y., Salacinski, H. J., Butler, P. E., Hamilton, G., and Seifalian, A. M., 2005, "Current status of prosthetic bypass grafts: a review," Journal of biomedical materials research. Part B, Applied biomaterials, 74(1), pp. 570-581.

[7] Rocco, K. A., Maxfield, M. W., Best, C. A., Dean, E. W., and Breuer, C. K., 2014, "In vivo applications of electrospun tissue-engineered vascular grafts: a review," Tissue engineering. Part B, Reviews, 20(6), pp. 628-640.

[8] Roll, S., Müller-Nordhorn, J., Keil, T., Scholz, H., Eidt, D., Greiner, W., and Willich, S. N., 2008, "Dacron(®)vs. PTFE as bypass materials in peripheral vascular surgery – systematic review and meta-analysis," BMC Surgery, 8, pp. 22-22.

[9] Spadaccio, C., Nappi, F., Al-Attar, N., Sutherland, F. W., Acar, C., Nenna, A., Trombetta, M., Chello, M., and Rainer, A., 2016, "Old Myths, New Concerns: the Long-Term Effects of Ascending Aorta Replacement with Dacron Grafts. Not All That Glitters Is Gold," Journal of Cardiovascular Translational Research, 9, pp. 334-342.

[10] Catto, V., Far, #xe8, , S., Freddi, G., and Tanzi, M. C., 2014, "Vascular Tissue Engineering: Recent Advances in Small Diameter Blood Vessel Regeneration," ISRN Vascular Medicine, 2014, p. 27.

[11] Nemeno-Guanzon, J. G., Lee, S., Berg, J. R., Jo, Y. H., Yeo, J. E., Nam, B. M., Koh, Y.-G., and Lee, J. I., 2012, "Trends in Tissue Engineering for Blood Vessels," Journal of Biomedicine and Biotechnology, 2012, p. 956345.

[12] Wang, X., Lin, P., Yao, Q., and Chen, C., 2007, "Development of small-diameter vascular grafts," World journal of surgery, 31(4), pp. 682-689.

[13] Wang, S., Mo, X. M., Jiang, B. J., Gao, C. J., Wang, H. S., Zhuang, Y. G., and Qiu, L. J., 2013, "Fabrication of small-diameter vascular scaffolds by heparin-bonded P(LLA-CL) composite nanofibers to improve graft patency," International journal of nanomedicine, 8, pp. 2131-2139.

[14] Hashi, C. K., Derugin, N., Janairo, R. R. R., Lee, R., Schultz, D., Lotz, J., and Li, S., 2010, "Anti-Thrombogenic Modification of Small-Diameter Microfibrous Vascular Grafts," Arteriosclerosis, thrombosis, and vascular biology, 30(8), pp. 1621-1627.

[15] Guo, H.-F., Dai, W.-W., Qian, D.-H., Qin, Z.-X., Lei, Y., Hou, X.-Y., and Wen, C., 2017, "A simply prepared small-diameter artificial blood vessel that promotes in situ endothelialization," Acta Biomaterialia, 54, pp. 107-116.

[16] Trubel, W., Moritz, A., Schima, H., Raderer, F., Scherer, R., Ullrich, R., Losert, U., and Polterauer, P., 1994, "Compliance and formation of distal anastomotic intimal hyperplasia in Dacron mesh tube constricted veins used as arterial bypass grafts," ASAIO journal (American Society for Artificial Internal Organs : 1992), 40(3), pp. M273-278.

[17] Trubel, W., Schima, H., Moritz, A., Raderer, F., Windisch, A., Ullrich, R., Windberger, U., Losert, U., and Polterauer, P., 1995, "Compliance mismatch and formation of distal anastomotic intimal hyperplasia in externally stiffened and lumen-adapted venous grafts," European journal of vascular and endovascular surgery : the official journal of the European Society for Vascular Surgery, 10(4), pp. 415-423.

[18] Ballyk, P. D., Walsh, C., Butany, J., and Ojha, M., 1998, "Compliance mismatch may promote graft-artery intimal hyperplasia by altering suture-line stresses," Journal of biomechanics, 31(3), pp. 229-237.

[19] Aydin, S., Aydin, S., Eren, M. N., Sahin, İ., Yilmaz, M., Kalayci, M., and Gungor, O., 2013, "The cardiovascular system and the biochemistry of grafts used in heart surgery," SpringerPlus, 2(1), p. 612.

[20] Kim, S. H., Turnbull, J., and Guimond, S., 2011, "Extracellular matrix and cell signalling: the dynamic cooperation of integrin, proteoglycan and growth factor receptor," The Journal of endocrinology, 209(2), pp. 139-151.

[21] Wagenseil, J. E., and Mecham, R. P., 2009, "Vascular extracellular matrix and arterial mechanics," Physiological reviews, 89(3), pp. 957-989.

[22] Ma, K., 2013, "Diagram of an artery," https://en.wikipedia.org/wiki/Artery#/media/File:Artery_(retouched).svg.

[23] Ma, H., Hu, J., and Ma, P. X., 2010, "Polymer scaffolds for small-diameter vascular tissue engineering," Advanced functional materials, 20(17), pp. 2833-2841.

[24] Nieponice, A., Soletti, L., Guan, J., Hong, Y., Gharaibeh, B., Maul, T. M., Huard, J., Wagner, W. R., and Vorp, D. A., 2010, "In vivo assessment of a tissue-engineered vascular graft combining a biodegradable elastomeric scaffold and muscle-derived stem cells in a rat model," Tissue engineering. Part A, 16(4), pp. 1215-1223.

[25] Wang, W., Hu, J., He, C., Nie, W., Feng, W., Qiu, K., Zhou, X., Gao, Y., and Wang, G., 2015, "Heparinized PLLA/PLCL nanofibrous scaffold for potential engineering of small-diameter blood vessel: tunable elasticity and anticoagulation property," J Biomed Mater Res A, 103(5), pp. 1784-1797.

[26] Jing, X., Mi, H. Y., Salick, M. R., Cordie, T. M., Peng, X. F., and Turng, L. S., 2015, "Electrospinning thermoplastic polyurethane/graphene oxide scaffolds for small diameter vascular graft applications," Materials science & engineering. C, Materials for biological applications, 49, pp. 40-50.

[27] Tan, Z., Wang, H., Gao, X., Liu, T., and Tan, Y., 2016, "Composite vascular grafts with high cell infiltration by co-electrospinning," Materials science & engineering. C, Materials for biological applications, 67, pp. 369-377.

[28] Woods, I., and Flanagan, T. C., 2014, "Electrospinning of biomimetic scaffolds for tissue-engineered vascular grafts: threading the path," Expert review of cardiovascular therapy, 12(7), pp. 815-832.

[29] Pillay, V., Dott, C., Choonara, Y. E., Tyagi, C., Tomar, L., Kumar, P., du Toit, L. C., and Ndesendo, V. M. K., 2013, "A Review of the Effect of Processing Variables on the Fabrication of Electrospun Nanofibers for Drug Delivery Applications," Journal of Nanomaterials, 2013, p. 22.

[30] Chew, S. Y., Wen, Y., Dzenis, Y., and Leong, K. W., 2006, "The Role of Electrospinning in the Emerging Field of Nanomedicine," Current pharmaceutical design, 12(36), pp. 4751-4770.

[31] Zeugolis, D. I., Khew, S. T., Yew, E. S., Ekaputra, A. K., Tong, Y. W., Yung, L. Y., Hutmacher, D. W., Sheppard, C., and Raghunath, M., 2008, "Electro-spinning of pure collagen nano-fibres - just an expensive way to make gelatin?," Biomaterials, 29(15), pp. 2293-2305.

[32] Burke, L. D., Blackwood, K. A., and Zomer Volpato, F., 2017, "Reproducibility and Robustness in Electrospinning with a View to Medical Device Manufacturing," Electrospun Biomaterials and Related Technologies, J. Almodovar, ed., Springer International Publishing, Cham, pp. 1-19.

[33] Kim, T., Yang, S. J., Sung, S. J., Kim, Y. S., Chang, M. S., Jung, H., and Park, C. R., 2015, "Highly reproducible thermocontrolled electrospun fiber based organic photovoltaic devices," ACS applied materials & interfaces, 7(8), pp. 4481-4487.

[34] Suyitno, Sholiehul, H., Zainal, A., Syamsul, H., and Raymundus Lullus, L., 2014, "Repeatability and Reproducibility of Fibre-Based Nanogenerator Synthesized by Electrospinning Machine," IOP Conference Series: Materials Science and Engineering, 58(1), p. 012013.

[35] Hasan, A., Memic, A., Annabi, N., Hossain, M., Paul, A., Dokmeci, M. R., Dehghani, F., and Khademhosseini, A., 2014, "Electrospun scaffolds for tissue engineering of vascular grafts," Acta Biomaterialia, 10(1), pp. 11-25.

[36] Rocco, K. A., Maxfield, M. W., Best, C. A., Dean, E. W., and Breuer, C. K., 2014, "In Vivo Applications of Electrospun Tissue-Engineered Vascular Grafts: A Review," Tissue Engineering Part B: Reviews, 20(6), pp. 628-640.

[37] Yao, J., Bastiaansen, C., and Peijs, T., 2014, High Strength and High Modulus Electrospun Nanofibers.

[38] He, J., Qin, T., Liu, Y., Li, X., Li, D., and Jin, Z., 2014, "Electrospinning of nanofibrous scaffolds with continuous structure and material gradients," Materials Letters, 137(0), pp. 393-397.

[39] Hong, Y., Ye, S. H., Nieponice, A., Soletti, L., Vorp, D. A., and Wagner, W. R., 2009, "A small diameter, fibrous vascular conduit generated from a poly(ester urethane)urea and phospholipid polymer blend," Biomaterials, 30(13), pp. 2457-2467.

[40] Nieponice, A., Soletti, L., Guan, J., Deasy, B. M., Huard, J., Wagner, W. R., and Vorp, D. A., 2008, "Development of a tissue-engineered vascular graft combining a biodegradable scaffold, muscle-derived stem cells and a rotational vacuum seeding technique," Biomaterials, 29(7), pp. 825-833.

[41] Soletti, L., Hong, Y., Guan, J., Stankus, J. J., El-Kurdi, M. S., Wagner, W. R., and Vorp, D. A., 2010, "A bilayered elastomeric scaffold for tissue engineering of small diameter vascular grafts," Acta biomaterialia, 6(1), pp. 110-122.

[42] Tai, N. R., Salacinski, H. J., Edwards, A., Hamilton, G., and Seifalian, A. M., 2000, "Compliance properties of conduits used in vascular reconstruction," The British journal of surgery, 87(11), pp. 1516-1524.

[43] Hong, Y., Ye, S.-H., Nieponice, A., Soletti, L., Vorp, D. A., and Wagner, W. R., 2009, "A small diameter, fibrous vascular conduit generated from a poly(ester urethane)urea and phospholipid polymer blend," Biomaterials, 30(13), pp. 2457-2467.

[44] K. Awad, N., Niu, H., Ali, U., S. Morsi, Y., and Lin, T., 2018, Electrospun Fibrous Scaffolds for Small-Diameter Blood Vessels: A Review.

[45] Punnakitikashem, P., Truong, D., Menon, J. U., Nguyen, K. T., and Hong, Y., 2014, "Electrospun biodegradable elastic polyurethane scaffolds with dipyridamole release for small diameter vascular grafts," Acta biomaterialia, 10(11), pp. 4618-4628.

[46] Bergmeister, H., Seyidova, N., Schreiber, C., Strobl, M., Grasl, C., Walter, I., Messner, B., Baudis, S., Fröhlich, S., Marchetti-Deschmann, M., Griesser, M., di Franco, M., Krssak, M., Liska, R., and Schima, H., 2015, "Biodegradable, thermoplastic polyurethane grafts for small diameter vascular replacements," Acta biomaterialia, 11, pp. 104-113.

[47] Catto, V., Fare, S., Cattaneo, I., Figliuzzi, M., Alessandrino, A., Freddi, G., Remuzzi, A., and Tanzi, M. C., 2015, "Small diameter electrospun silk fibroin vascular grafts: Mechanical properties, in vitro biodegradability, and in vivo biocompatibility," Materials science & engineering. C, Materials for biological applications, 54, pp. 101-111.

[48] Hu, Z.-j., Li, Z.-l., Hu, L.-y., He, W., Liu, R.-m., Qin, Y.-s., and Wang, S.-m., 2012, "The in vivo performance of small-caliber nanofibrous polyurethane vascular grafts," BMC Cardiovascular Disorders, 12, pp. 115-115.

[49] Matsumura, G., Isayama, N., Matsuda, S., Taki, K., Sakamoto, Y., Ikada, Y., and Yamazaki, K., 2013, "Long-term results of cell-free biodegradable scaffolds for in situ tissue engineering of pulmonary artery in a canine model," Biomaterials, 34(27), pp. 6422-6428.

[50] Udelsman, B. V., Khosravi, R., Miller, K. S., Dean, E. W., Bersi, M. R., Rocco, K., Yi, T., Humphrey, J. D., and Breuer, C. K., 2014, "Characterization of evolving biomechanical properties of tissue engineered vascular grafts in the arterial circulation," J Biomech, 47(9), pp. 2070-2079.

[51] Zhang, L., Zhou, J., Lu, Q., Wei, Y., and Hu, S., 2008, "A novel small-diameter vascular graft: in vivo behavior of biodegradable three-layered tubular scaffolds," Biotechnology and bioengineering, 99(4), pp. 1007-1015.

[52] Shinoka, T., Shum-Tim, D., Ma, P. X., Tanel, R. E., Isogai, N., Langer, R., Vacanti, J. P., and Mayer Jr, J. E., 1998, "Creation Of Viable Pulmonary Artery Autografts Through Tissue Engineering," The Journal of thoracic and cardiovascular surgery, 115(3), pp. 536-546.

[53] Wang, S., Mo, X. M., Jiang, B. J., Gao, C. J., Wang, H. S., Zhuang, Y. G., and Qiu, L. J., 2013, "Fabrication of small-diameter vascular scaffolds by heparin-bonded P(LLA-CL) composite nanofibers to improve graft patency," International Journal of Nanomedicine, 8, pp. 2131-2139.

[54] Salles, C. A., Buffolo, E., Andrade, J. C., Palma, J. H., Silva, R. R., Santiago, R., Casagrande, I. S., and Moreira, M. C., 1998, "Mitral valve replacement with glutaraldehyde preserved aortic allografts," European journal of cardio-thoracic surgery : official journal of the European Association for Cardio-thoracic Surgery, 13(2), pp. 135-143.

[55] Huang, Z.-M., Zhang, Y. Z., Ramakrishna, S., and Lim, C. T., 2004, "Electrospinning and mechanical characterization of gelatin nanofibers," Polymer, 45(15), pp. 5361-5368.

[56] Kumar, V. A., Caves, J. M., Haller, C. A., Dai, E., Liu, L., Grainger, S., and Chaikof, E. L., 2013, "Acellular vascular grafts generated from collagen and elastin analogs," Acta biomaterialia, 9(9), pp. 8067-8074.

[57] L'Heureux, N., Paquet, S., Labbe, R., Germain, L., and Auger, F. A., 1998, "A completely biological tissue-engineered human blood vessel," FASEB journal : official publication of the Federation of American Societies for Experimental Biology, 12(1), pp. 47-56.

[58] Matthews, J. A., Wnek, G. E., Simpson, D. G., and Bowlin, G. L., 2002, "Electrospinning of collagen nanofibers," Biomacromolecules, 3(2), pp. 232-238.

[59] McManus, M. C., Boland, E. D., Koo, H. P., Barnes, C. P., Pawlowski, K. J., Wnek, G. E., Simpson, D. G., and Bowlin, G. L., 2006, "Mechanical properties of electrospun fibrinogen structures," Acta biomaterialia, 2(1), pp. 19-28.

[60] Nivison-Smith, L., Rnjak, J., and Weiss, A. S., 2010, "Synthetic human elastin microfibers: stable cross-linked tropoelastin and cell interactive constructs for tissue engineering applications," Acta biomaterialia, 6(2), pp. 354-359.

[61] Perumcherry, S. R., Chennazhi, K. P., Nair, S. V., Menon, D., and Afeesh, R., 2011, "A novel method for the fabrication of fibrin-based electrospun nanofibrous scaffold for tissue-engineering applications," Tissue engineering. Part C, Methods, 17(11), pp. 1121-1130.

[62] McClure, M. J., Sell, S. A., Simpson, D. G., Walpoth, B. H., and Bowlin, G. L., 2010, "A three-layered electrospun matrix to mimic native arterial architecture using polycaprolactone, elastin, and collagen: a preliminary study," Acta biomaterialia, 6(7), pp. 2422-2433.

[63] Merkle, V., Zeng, L., Teng, W., Slepian, M., and Wu, X., 2013, "Gelatin shells strengthen polyvinyl alcohol core–shell nanofibers," Polymer, 54(21), pp. 6003-6007.

[64] Merkle, V. M., Zeng, L., Slepian, M. J., and Wu, X., 2014, "Core-shell nanofibers: Integrating the bioactivity of gelatin and the mechanical property of polyvinyl alcohol," Biopolymers, 101(4), pp. 336-346.

[65] Stitzel, J. D., Pawlowski, K. J., Wnek, G. E., Simpson, D. G., and Bowlin, G. L., 2001, "Arterial smooth muscle cell proliferation on a novel biomimicking, biodegradable vascular graft scaffold," Journal of biomaterials applications, 16(1), pp. 22-33.

[66] Wise, S. G., Byrom, M. J., Waterhouse, A., Bannon, P. G., Weiss, A. S., and Ng, M. K., 2011, "A multilayered synthetic human elastin/polycaprolactone hybrid vascular graft with tailored mechanical properties," Acta biomaterialia, 7(1), pp. 295-303.

[67] Jha, B. S., Ayres, C. E., Bowman, J. R., Telemeco, T. A., Sell, S. A., Bowlin, G. L., and Simpson, D. G., 2011, "Electrospun Collagen: A Tissue Engineering Scaffold with Unique Functional Properties in a Wide Variety of Applications," Journal of Nanomaterials, 2011, p. 15.

[68] Le Corre-Bordes, D., Hofman, K., and Hall, B., 2018, "Guide to electrospinning denatured whole chain collagen from hoki fish using benign solvents," International journal of biological macromolecules.

[69] Buttafoco, L., Kolkman, N. G., Engbers-Buijtenhuijs, P., Poot, A. A., Dijkstra, P. J., Vermes, I., and Feijen, J., 2006, "Electrospinning of collagen and elastin for tissue engineering applications," Biomaterials, 27(5), pp. 724-734.

[70] Rnjak-Kovacina, J., Wise, S. G., Li, Z., Maitz, P. K. M., Young, C. J., Wang, Y., and Weiss, A. S., 2012, "Electrospun synthetic human elastin:collagen composite scaffolds for dermal tissue engineering," Acta Biomaterialia, 8(10), pp. 3714-3722.

[71] Boland, E., A Matthews, J., J Pawlowski, K., G Simpson, D., Wnek, G., and Bowlin, G., 2004, Electrospinning collagen and elastin: Preliminary vascular tissue engineering.

[72] Boland, E. D., Matthews, J. A., Pawlowski, K. J., Simpson, D. G., Wnek, G. E., and Bowlin, G. L., 2004, "Electrospinning collagen and elastin: preliminary vascular tissue engineering," Frontiers in bioscience : a journal and virtual library, 9, pp. 1422-1432.

[73] Aoki, H., Miyoshi, H., and Yamagata, Y., 2014, "Electrospinning of gelatin nanofiber scaffolds with mild neutral cosolvents for use in tissue engineering," Polymer Journal, 47, p. 267.

[74] Maleknia, L., and Rezazadeh Majdi, Z., 2014, Electrospinning of Gelatin Nanofiber for biomedical Application.

[75] Laha, A., Sharma, C. S., and Majumdar, S., 2016, "Electrospun gelatin nanofibers as drug carrier: effect of crosslinking on sustained release," Materials Today: Proceedings, 3(10, Part A), pp. 3484-3491.

[76] Zhan, J., Morsi, Y., Ei-Hamshary, H., Al-Deyab, S. S., and Mo, X., 2016, "In vitro evaluation of electrospun gelatin–glutaraldehyde nanofibers," Frontiers of Materials Science, 10(1), pp. 90-100.

[77] Balasubramanian, P., Prabhakaran, M. P., Kai, D., and Ramakrishna, S., 2013, "Human cardiomyocyte interaction with electrospun fibrinogen/gelatin nanofibers for myocardial regeneration," Journal of biomaterials science. Polymer edition, 24(14), pp. 1660-1675.

[78] Tamimi, E., Ardila, D. C., Haskett, D. G., Doetschman, T., Slepian, M. J., Kellar, R. S., and Vande Geest, J. P., 2016, "Biomechanical Comparison of Glutaraldehyde-Crosslinked Gelatin Fibrinogen Electrospun Scaffolds to Porcine Coronary Arteries," Journal of biomechanical engineering, 138(1).

[79] Ardila, D. C., Tamimi, E., Danford, F. L., Haskett, D. G., Kellar, R. S., Doetschman, T., and Vande Geest, J. P., 2015, "TGFbeta2 differentially modulates smooth muscle cell proliferation and migration in electrospun gelatin-fibrinogen constructs," Biomaterials, 37, pp. 164-173.

[80] Machula, H., Ensley, B., and Kellar, R., 2014, "Electrospun Tropoelastin for Delivery of Therapeutic Adipose-Derived Stem Cells to Full-Thickness Dermal Wounds," Advances in Wound Care, 3(5), pp. 367-375.

[81] McKenna, K. A., Gregory, K. W., Sarao, R. C., Maslen, C. L., Glanville, R. W., and Hinds, M. T., 2012, "Structural and Cellular Characterization of Electrospun Recombinant Human Tropoelastin Biomaterials()," Journal of biomaterials applications, 27(2), pp. 219-230.

[82] McKenna, K. A., Hinds, M. T., Sarao, R. C., Wu, P.-C., Maslen, C. L., Glanville, R. W., Babcock, D., and Gregory, K. W., 2012, "Mechanical Property Characterization of Electrospun Recombinant Human Tropoelastin for Vascular Graft Biomaterials," Acta biomaterialia, 8(1), pp. 225-233.

[83] Gatford, J., 2008, "Diagram showing fibre formation by electrospinning," https://en.wikipedia.org/wiki/Electrospinning#/media/File:Electrospinning_Diagram.jpg.

[84] MCClure, M. J., Sell, S., Simpson, D., Bowlin, G., 2009, "Electrospun Polydioxanone, Elastin, and Collagen Vascular Scaffolds: Uniaxial Cyclic Distension," Journal of Engineered Fibers and Fabrics, 4(2).

[85] Wong, C. S., Liu, X., Xu, Z., Lin, T., and Wang, X., 2013, "Elastin and collagen enhances electrospun aligned polyurethane as scaffolds for vascular graft," Journal of materials science. Materials in medicine, 24(8), pp. 1865-1874.

[86] Sell, S. A., Wolfe, P. S., Garg, K., McCool, J. M., Rodriguez, I. A., and Bowlin, G. L., 2010, "The Use of Natural Polymers in Tissue Engineering: A Focus on Electrospun Extracellular Matrix Analogues," Polymers, 2(4), pp. 522-553.

[87] Grover, C. N., Gwynne, J. H., Pugh, N., Hamaia, S., Farndale, R. W., Best, S. M., and Cameron, R. E., 2012, "Crosslinking and composition influence the surface properties, mechanical stiffness and cell reactivity of collagen-based films," Acta biomaterialia, 8(8), pp. 3080-3090.

[88] Rose, J., Pacelli, S., Haj, A., Dua, H., Hopkinson, A., White, L., and Rose, F., 2014, "Gelatin-Based Materials in Ocular Tissue Engineering," Materials, 7(4), p. 3106.

[89] Gorgieva, S., and Kokol, V., 2011, Collagen- Vs. Gelatine-Based Biomaterials and Their Biocompatibility: Review and Perspectives, INTECH Open Access Publisher.

[90] Ardila, D. C., Tamimi, E., Danford, F. L., Haskett, D. G., Kellar, R. S., Doetschman, T., and Vande Geest, J. P., 2014, "TGFbeta2 differentially modulates smooth muscle cell proliferation and migration in electrospun gelatin-fibrinogen constructs," Biomaterials, 37C, pp. 164-173.

[91] Wise, S. G., Yeo, G. C., Hiob, M. A., Rnjak-Kovacina, J., Kaplan, D. L., Ng, M. K. C., and Weiss, A. S., 2014, "Tropoelastin: A versatile, bioactive assembly module," Acta Biomaterialia, 10(4), pp. 1532-1541.

[92] Senior, R. M., Griffin, G. L., and Mecham, R. P., 1980, "Chemotactic activity of elastin-derived peptides," The Journal of clinical investigation, 66(4), pp. 859-862.

[93] Wise, S. G., and Weiss, A. S., 2009, "Tropoelastin," The international journal of biochemistry & cell biology, 41(3), pp. 494-497.

[94] Indik, Z., Abrams, W. R., Kucich, U., Gibson, C. W., Mecham, R. P., and Rosenbloom, J., 1990, "Production of recombinant human tropoelastin: Characterization and demonstration of immunologic and chemotactic activity," Archives of Biochemistry and Biophysics, 280(1), pp. 80-86.

[95] Nivison-Smith, L., Rnjak, J., and Weiss, A. S., 2010, "Synthetic human elastin microfibers: Stable cross-linked tropoelastin and cell interactive constructs for tissue engineering applications," Acta Biomaterialia, 6(2), pp. 354-359.

[96] Sell, S. A., Francis, M. P., Garg, K., McClure, M. J., Simpson, D. G., and Bowlin, G. L., 2008, "Cross-linking methods of electrospun fibrinogen scaffolds for tissue engineering applications," Biomedical materials (Bristol, England), 3(4), p. 045001.

[97] Luo, X., Guo, Z., He, P., Chen, T., Li, L., Ding, S., and Li, H., 2018, "Study on structure, mechanical property and cell cytocompatibility of electrospun collagen nanofibers crosslinked by common agents," International journal of biological macromolecules, 113, pp. 476-486.

[98] McClure, M. J., Sell, S., Barnes, C., Bowen, W., Bowlin, G., 2008, "Cross-linking Electrospun Polydioxanone-Soluble Elastin Blends: Material Characterization," Journal of Engineered Fibers and Fabrics, 3(1).

[99] Zhang, S., Huang, Y., Yang, X., Mei, F., Ma, Q., Chen, G., Ryu, S., and Deng, X., 2009, "Gelatin nanofibrous membrane fabricated by electrospinning of aqueous gelatin solution for guided tissue regeneration," Journal of biomedical materials research. Part A, 90(3), pp. 671-679.

[100] Tamimi, E., Ardila, D. C., Haskett, D. G., Doetschman, T., Slepian, M. J., Kellar, R. S., and Vande Geest, J. P., 2015, "Biomechanical Comparison of Glutaraldehyde-Crosslinked Gelatin Fibrinogen Electrospun Scaffolds to Porcine Coronary Arteries," Journal of biomechanical engineering, 138(1), pp. 011001-011001-011012.

[101] Gough, J. E., Scotchford, C. A., and Downes, S., 2002, "Cytotoxicity of glutaraldehyde crosslinked collagen/poly(vinyl alcohol) films is by the mechanism of apoptosis," Journal of biomedical materials research, 61(1), pp. 121-130.

[102] Kim, K. M., Herrera, G. A., and Battarbee, H. D., 1999, "Role of Glutaraldehyde in Calcification of Porcine Aortic Valve Fibroblasts," The American Journal of Pathology, 154(3), pp. 843-852.

[103] Chanda, J., Kondoh, K., Ijima, K., Matsukawa, M., and Kuribayashi, R., 1998, "In vitro and in vivo calcification of vascular bioprostheses," Biomaterials, 19(18), pp. 1651-1656.

[104] Golomb, G., Schoen, F. J., Smith, M. S., Linden, J., Dixon, M., and Levy, R. J., 1987, "The role of glutaraldehyde-induced cross-links in calcification of bovine pericardium used in cardiac valve bioprostheses," The American Journal of Pathology, 127(1), pp. 122-130.

[105] Lim, H. G., Kim, S. H., Choi, S. Y., and Kim, Y. J., 2012, "Anticalcification effects of decellularization, solvent, and detoxification treatment for genipin and glutaraldehyde fixation of bovine pericardium," European journal of cardio-thoracic surgery : official journal of the European Association for Cardio-thoracic Surgery, 41(2), pp. 383-390.

[106] Yoo, J. S., Kim, Y. J., Kim, S. H., and Choi, S. H., 2011, "Study on genipin: a new alternative natural crosslinking agent for fixing heterograft tissue," The Korean journal of thoracic and cardiovascular surgery, 44(3), pp. 197-207.

[107] Sung, H. W., Huang, D. M., Chang, W. H., Huang, R. N., and Hsu, J. C., 1999, "Evaluation of gelatin hydrogel crosslinked with various crosslinking agents as bioadhesives: In vitro study," Journal of biomedical materials research, 46(4), pp. 520-530.

[108] Manickam, B., Sreedharan, R., and Elumalai, M., 2014, "'Genipin' - the natural water soluble cross-linking agent and its importance in the modified drug delivery systems: an overview," Current drug delivery, 11(1), pp. 139-145.

[109] Mekhail, M., Wong, K. K., Padavan, D. T., Wu, Y., O'Gorman, D. B., and Wan, W., 2011, "Genipin-cross-linked electrospun collagen fibers," Journal of biomaterials science. Polymer edition, 22(17), pp. 2241-2259.

[110] Sisson, K., Zhang, C., Farach-Carson, M. C., Chase, D. B., and Rabolt, J. F., 2009, "Evaluation of cross-linking methods for electrospun gelatin on cell growth and viability," Biomacromolecules, 10(7), pp. 1675-1680.

[111] Brown, J. H., Das, P., DiVito, M. D., Ivancic, D., Poh Tan, L., and Wertheim, J. A., 2018, "Nanofibrous PLGA Electrospun Scaffolds Modified with Type I Collagen Influence Hepatocyte Function and Support Viability In Vitro," Acta Biomaterialia.

[112] Yao, Q., Zhang, W., Hu, Y., Chen, J., Shao, C., Fan, X., and Fu, Y., 2017, "Electrospun collagen/poly(L-lactic acid-co-epsilon-caprolactone) scaffolds for conjunctival tissue engineering," Experimental and therapeutic medicine, 14(5), pp. 4141-4147.

[113] Han, J., Lazarovici, P., Pomerantz, C., Chen, X., Wei, Y., and Lelkes, P. I., 2011, "Co-Electrospun Blends of PLGA, Gelatin, and Elastin as Potential Nonthrombogenic Scaffolds for Vascular Tissue Engineering," Biomacromolecules, 12(2), pp. 399-408.

[114] Zhang, Q., Lv, S., Lu, J., Jiang, S., and Lin, L., 2015, "Characterization of polycaprolactone/collagen fibrous scaffolds by electrospinning and their bioactivity," International journal of biological macromolecules, 76, pp. 94-101.

[115] Hackett, J. M., Dang, T. T., Tsai, E. C., and Cao, X., 2010, "Electrospun Biocomposite Polycaprolactone/Collagen Tubes as Scaffolds for Neural Stem Cell Differentiation," Materials, 3(6), pp. 3714-3728.

[116] Swindle-Reilly, K. E., Paranjape, C. S., and Miller, C. A., 2014, "Electrospun poly(caprolactone)-elastin scaffolds for peripheral nerve regeneration," Progress in Biomaterials, 3, p. 20.

[117] Liu, Y., Xu, Y., Wang, Z., Wen, D., Zhang, W., Schmull, S., Li, H., Chen, Y., and Xue, S., 2016, "Electrospun nanofibrous sheets of collagen/elastin/polycaprolactone improve cardiac repair after myocardial infarction," American Journal of Translational Research, 8(4), pp. 1678-1694.

[118] Yang, G., Lin, H., Rothrauff, B. B., Yu, S., and Tuan, R. S., 2016, "Multilayered Polycaprolactone/Gelatin Fiber-Hydrogel Composite for Tendon Tissue Engineering," Acta biomaterialia, 35, pp. 68-76.

[119] Wise, S. G., Byrom, M. J., Waterhouse, A., Bannon, P. G., Ng, M. K. C., and Weiss, A. S., 2011, "A multilayered synthetic human elastin/polycaprolactone hybrid vascular graft with tailored mechanical properties," Acta Biomaterialia, 7(1), pp. 295-303.

[120] Ghista, D., and Kabinejadian, F., 2013, "Coronary artery bypass grafting hemodynamics and anastomosis design: a biomedical engineering review," BioMedical Engineering OnLine, 12(1), pp. 1-28.

[121] Amoroso, N. J., D'Amore, A., Hong, Y., Rivera, C. P., Sacks, M. S., and Wagner, W. R., 2012, "Microstructural manipulation of electrospun scaffolds for specific bending stiffness for heart valve tissue engineering," Acta biomaterialia, 8(12), pp. 4268-4277.

[122] Liu, S., Dong, C., Lu, G., Lu, Q., Li, Z., Kaplan, D. L., and Zhu, H., 2013, "Bilayered vascular grafts based on silk proteins," Acta biomaterialia, 9(11), pp. 8991-9003.

[123] Naito, Y., Lee, Y. U., Yi, T., Church, S. N., Solomon, D., Humphrey, J. D., Shin'oka, T., and Breuer, C. K., 2014, "Beyond burst pressure: initial evaluation of the natural history of the biaxial mechanical properties of tissue-engineered vascular grafts in the venous circulation using a murine model," Tissue engineering. Part A, 20(1-2), pp. 346-355.

[124] Soletti, L., Hong, Y., Guan, J., Stankus, J. J., El-Kurdi, M. S., Wagner, W. R., and Vorp, D. A., 2010, "A bilayered elastomeric scaffold for tissue engineering of small diameter vascular grafts," Acta Biomaterialia, 6(1), pp. 110-122.

[125] Wang, F., Mohammed, A., Li, C., Ge, P., Wang, L., and King, M. W., 2014, "Degradable/non-degradable polymer composites for in-situ tissue engineering small diameter vascular prosthesis application," Bio-medical materials and engineering, 24(6), pp. 2127-2133.

[126] Chung, J., and Li, J. K., 2004, "Hemodynamic simulation of vascular prosthesis altering pulse wave propagation," Conference proceedings : ... Annual International Conference of the IEEE Engineering in Medicine and Biology Society. IEEE Engineering in Medicine and Biology Society. Annual Conference, 5, pp. 3678-3680.

[127] Abbott, W. M., Megerman, J., Hasson, J. E., L'Italien, G., and Warnock, D. F., 1987, "Effect of compliance mismatch on vascular graft patency," Journal of Vascular Surgery, 5(2), pp. 376-382.

[128] Trubel, W., Schima, H., Moritz, A., Raderer, F., Windisch, A., Ullrich, R., Windberger, U., Losert, U., and Polterauer, P., 1995, "Compliance mismatch and formation of distal anastomotic intimal hyperplasia in externally stiffened and lumen-adapted venous grafts," European Journal of Vascular and Endovascular Surgery, 10(4), pp. 415-423.

[129] Matsumoto, T., Naiki, T., and Hayashi, K., 1992, "Flow visualization analysis in a model of artery-graft anastomosis," Bio-medical materials and engineering, 2(4), pp. 171-183.

[130] Stewart, S. F. C., and Lyman, D. J., 2004, "Effects of an Artery/Vascular Graft Compliance Mismatch on Protein Transport: A Numerical Study," Annals of biomedical engineering, 32(7), pp. 991-1006.

[131] Chandran, K. B., Gao, D., Han, G., Baraniewski, H., and Corson, J. D., 1992, "Finite-element analysis of arterial anastomoses with vein, Dacron and PTFE grafts," Medical & biological engineering & computing, 30(4), pp. 413-418.

[132] Rickard, R. F., Meyer, C., and Hudson, D. A., 2009, "Computational modeling of microarterial anastomoses with size discrepancy (small-to-large)," The Journal of surgical research, 153(1), pp. 1-11.

[133] Keyes, J. T., Lockwood, D. R., Utzinger, U., Montilla, L. G., Witte, R. S., and Vande Geest, J. P., 2013, "Comparisons of Planar and Tubular Biaxial Tensile Testing Protocols of the Same Porcine Coronary Arteries," Ann Biomed Eng, 41(7), pp. 1579-1591.

[134] Haskett D, S. E., Fouts M, Larson D, Azhar M, Utzinger U, Vande Geest JP, 2012, "The effects of angiotensin II on the coupled microstructural and biomechanical response of C57BL/6 mouse aorta," Journal of Biomechanics, 45(2), pp. 722-729.

[135] Haskett DG, A. M., Utzinger U, Vande Geest JP, 2013, "Progressive alterations in microstructural organization and biomechanical response in the apoE mouse model of aneurysm," Biomatter, 3(2), pp. e24648-24641 to e24648-24610.

[136] Haskett DG, D. J., Gard C, Chen H, Ball C, Estabrook MA, Encinas AC, Dietz HC, Utzinger U, Vande Geest JP, Axzhar M., 2012, "Altered tissue behavior of non-aneurysmal descending thoracic aorta in the mouse model of marfan syndrome," Cell and Tissue Research, 347(1), pp. 267-277.

[137] Keyes, J. T., Borowicz, S. M., Rader, J. H., Utzinger, U., Azhar, M., and Vande Geest, J. P., "Design and Demonstration of a Microbiaxial Optomechanical Device for Multiscale Characterization of Soft Biological Tissues with Two-Photon Microscopy," Microsc Microanal, pp. 1-9.

[138] Keyes JT, U. U., Vande Geest JP. , 2011, "Adaptation of a Two-Photon-Microscope-Interfacing Planar Biaxial Testing Device for the Microstructural and Macroscopic Characterization of Small Tubular Tissue Specimens," Journal of Biomechanical Engineering, 133(7), p. 075001.

[139] Hearn, E. J., 1997, "Chapter 10 - Thick Cylinders," Mechanics of Materials 1 (Third Edition), E. J. Hearn, ed., Butterworth-Heinemann, Oxford, pp. 215-253.

[140] Haskett, D., Johnson, G., Zhou, A., Utzinger, U., and Vande Geest, J., 2010, "Microstructural and biomechanical alterations of the human aorta as a function of age and location," Biomechanics and modeling in mechanobiology, 9(6), pp. 725-736.

[141] Mitra, T., Sailakshmi, G., Gnanamani, A., and Mandal, A. B., 2011, "Cross-linking with acid chlorides improves thermal and mechanical properties of collagen based biopolymer material," Thermochimica Acta, 525(1–2), pp. 50-55.

[142] Dong, B., Arnoult, O., Smith, M. E., and Wnek, G. E., 2009, "Electrospinning of Collagen Nanofiber Scaffolds from Benign Solvents," Macromolecular Rapid Communications, 30(7), pp. 539-542.

[143] Caulk, A. W., Nepiyushchikh, Z. V., Shaw, R., Dixon, J. B., and Gleason, R. L., 2015, Quantification of the passive and active biaxial mechanical behaviour and microstructural organization of rat thoracic ducts.

[144] Wan, W., Dixon, J. B., and Gleason Jr, Rudolph L., 2012, "Constitutive Modeling of Mouse Carotid Arteries Using Experimentally Measured Microstructural Parameters," Biophysical Journal, 102(12), pp. 2916-2925.

[145] Keyes, J. T., Lockwood, D. R., Simon, B. R., and Vande Geest, J. P., 2013, "Deformationally dependent fluid transport properties of porcine coronary arteries based on location in the coronary vasculature," Journal of the mechanical behavior of biomedical materials, 17, pp. 296-306.

[146] Dahl, S. L. M., Vaughn, M. E., Hu, J.-J., Driessen, N. J. B., Baaijens, F. P. T., Humphrey, J. D., and Niklason, L. E., 2008, "A Microstructurally Motivated Model of the Mechanical Behavior of Tissue Engineered Blood Vessels," Ann Biomed Eng, 36(11), pp. 1782-1792.

[147] Zaucha, M. T., Gauvin, R., Auger, F. A., Germain, L., and Gleason, R. L., 2011, Biaxial biomechanical properties of self-assembly tissue-engineered blood vessels.

[148] Mandru, M., Ionescu, C., and Chirita, M., 2009, "Modelling Mechanical Properties in Native and Biomimetically Formed Vascular Grafts," Journal of Bionic Engineering, 6(4), pp. 371-377.

[149] Telemeco, T. A., Ayres, C., Bowlin, G. L., Wnek, G. E., Boland, E. D., Cohen, N., Baumgarten, C. M., Mathews, J., and Simpson, D. G., 2005, "Regulation of cellular infiltration into tissue engineering scaffolds composed of submicron diameter fibrils produced by electrospinning," Acta biomaterialia, 1(4), pp. 377-385.

[150] Chauvaud, S., Jebara, V., Chachques, J. C., el Asmar, B., Mihaileanu, S., Perier, P., Dreyfus, G., Relland, J., Couetil, J. P., and Carpentier, A., 1991, "Valve extension with glutaraldehyde-preserved autologous pericardium. Results in mitral valve repair," The Journal of thoracic and cardiovascular surgery, 102(2), pp. 171-177; discussion 177-178.

[151] Hunziker, E. B., Lippuner, K., and Shintani, N., 2014, "How best to preserve and reveal the structural intricacies of cartilaginous tissue," Matrix Biology, 39(0), pp. 33-43.

[152] Ramesh, R., Kumar, N., Sharma, A. K., Maiti, S. K., and Singh, G. R., 2003, "Acellular and glutaraldehyde-preserved tendon allografts for reconstruction of superficial digital flexor tendon in bovines: Part I--Clinical, radiological and angiographical observations," Journal of veterinary medicine. A, Physiology, pathology, clinical medicine, 50(10), pp. 511-519.

[153] Jayakrishnan, A., and Jameela, S. R., 1996, "Glutaraldehyde as a fixative in bioprostheses and drug delivery matrices," Biomaterials, 17(5), pp. 471-484.

[154] Schmidt, C. E., and Baier, J. M., 2000, "Acellular vascular tissues: natural biomaterials for tissue repair and tissue engineering," Biomaterials, 21(22), pp. 2215-2231.

[155] Zhai, W., Zhang, H., Wu, C., Zhang, J., Sun, X., Zhang, H., Zhu, Z., and Chang, J., 2014, "Crosslinking of saphenous vein ECM by procyanidins for small diameter blood vessel replacement," Journal of biomedical materials research. Part B, Applied biomaterials, 102(6), pp. 1190-1198.

[156] Tillman, B. W., Yazdani, S. K., Lee, S. J., Geary, R. L., Atala, A., and Yoo, J. J., 2009, "The in vivo stability of electrospun polycaprolactone-collagen scaffolds in vascular reconstruction," Biomaterials, 30(4), pp. 583-588.

[157] Harrison, S., Tamimi, E., Uhlorn, J., Leach, T., and Vande Geest, J. P., 2015, "Computationally Optimizing the Compliance of a Biopolymer Based Tissue Engineered Vascular Graft," Journal of biomechanical engineering, 138(1), pp. 014505-014505-014505.

[158] Fung, and C, 1982, Biomechanics : Mechanical Properties of Living Tissues.

[159] Al-Jarrah, R., 1984, "On the Lagrange interpolation polynomials of entire functions," Journal of Approximation Theory, 41(2), pp. 170-178.

[160] Cheung, D. T., and Nimni, M. E., 1982, "Mechanism of crosslinking of proteins by glutaraldehyde I: reaction with model compounds," Connective tissue research, 10(2), pp. 187-199.

[161] Yoo, J. S., Kim, Y. J., Kim, S. H., and Choi, S. H., 2011, "Study on Genipin: A New Alternative Natural Crosslinking Agent for Fixing Heterograft Tissue," The Korean Journal of Thoracic and Cardiovascular Surgery, 44(3), pp. 197-207.

[162] Huang, R., Gao, X., Wang, J., Chen, H., Tong, C., Tan, Y., and Tan, Z., 2018, "Triple-Layer Vascular Grafts Fabricated by Combined E-Jet 3D Printing and Electrospinning," Annals of biomedical engineering.

[163] Nezarati, R. M., Eifert, M. B., Dempsey, D. K., and Cosgriff-Hernandez, E., 2015, "Electrospun vascular grafts with improved compliance matching to native vessels," Journal of biomedical materials research. Part B, Applied biomaterials, 103(2), pp. 313-323.

[164] Salacinski, H. J., Goldner, S., Giudiceandrea, A., Hamilton, G., Seifalian, A. M., Edwards, A., and Carson, R. J., 2001, "The mechanical behavior of vascular grafts: a review," Journal of biomaterials applications, 15(3), pp. 241-278.

[165] Soletti, L., Nieponice, A., Hong, Y., Ye, S.-H., Stankus, J. J., Wagner, W. R., and Vorp, D. A., 2011, "In vivo performance of a phospholipid-coated bioerodable elastomeric graft for small-diameter vascular applications," Journal of biomedical materials research. Part A, 96(2), pp. 436-448.

[166] Jankowska, M. A., Bartkowiak-Jowsa, M., and Bedzinski, R., 2015, "Experimental and constitutive modeling approaches for a study of biomechanical properties of human coronary arteries," Journal of the mechanical behavior of biomedical materials, 50, pp. 1-12.

[167] Szafron, J. M., Breuer, C. K., Wang, Y., and Humphrey, J. D., 2017, "Stress Analysis-Driven Design of Bilayered Scaffolds for Tissue-Engineered Vascular Grafts," Journal of biomechanical engineering, 139(12).

[168] Castillo-Cruz, O., Pérez-Aranda, C., Gamboa, F., Cauich-Rodríguez, J. V., Mantovani, D., and Avilés, F., 2018, "Prediction of circumferential compliance and burst strength of polymeric vascular grafts," Journal of the mechanical behavior of biomedical materials, 79, pp. 332-340.

[169] Bersi, M. R., Bellini, C., Di Achille, P., Humphrey, J. D., Genovese, K., and Avril, S., 2016, "Novel Methodology for Characterizing Regional Variations in the Material Properties of Murine Aortas," Journal of biomechanical engineering, 138(7).

[170] Pyne, J. D., Genovese, K., Casaletto, L., and Vande Geest, J. P., 2014, "Sequential-Digital Image Correlation for Mapping Human Posterior Sclera and Optic Nerve Head Deformation," Journal of biomechanical engineering, 136(2), pp. 0210021-02100212.

[171] Tamimi, E. A., Pyne, J. D., Muli, D. K., Axman, K. F., Howerton, S. J., Davis, M. R., Girkin, C. A., and Vande Geest, J. P., 2017, "Racioethnic Differences in Human Posterior Scleral and Optic Nerve Stump Deformation," Investigative Ophthalmology & Visual Science, 58(10), pp. 4235-4246.

[172] Weinreb, R. N., Aung, T., and Medeiros, F. A., 2014, "The pathophysiology and treatment of glaucoma: a review," JAMA, 311(18), pp. 1901-1911.

[173] Quigley, H. A., and Broman, A. T., 2006, "The number of people with glaucoma worldwide in 2010 and 2020," Br J Ophthalmol, 90(3), pp. 262-267.

[174] Downs, J. C., Roberts, M. D., and Burgoyne, C. F., 2008, "The Mechanical Environment of the Optic Nerve Head in Glaucoma," Optometry and vision science : official publication of the American Academy of Optometry, 85(6), pp. 425-435.

[175] Rudnicka, A. R., Mt-Isa, S., Owen, C. G., Cook, D. G., and Ashby, D., 2006, "Variations in primary open-angle glaucoma prevalence by age, gender, and race: a Bayesian meta-analysis," Invest Ophthalmol Vis Sci, 47(10), pp. 4254-4261.

[176] Anderson, D. R., and Hendrickson, A., 1974, "Effect of intraocular pressure on rapid axoplasmic transport in monkey optic nerve," Investigative ophthalmology, 13(10), pp. 771-783.

[177] Minckler, D. S., Bunt, A. H., and Johanson, G. W., 1977, "Orthograde and retrograde axoplasmic transport during acute ocular hypertension in the monkey," Invest Ophthalmol Vis Sci, 16(5), pp. 426-441.

[178] Bellezza, A. J., Rintalan, C. J., Thompson, H. W., Downs, J. C., Hart, R. T., and Burgoyne, C. F., 2003, "Deformation of the lamina cribrosa and anterior scleral canal wall in early experimental glaucoma," Invest Ophthalmol Vis Sci, 44(2), pp. 623-637.

[179] Burgoyne, C., 2015, "The morphological difference between glaucoma and other optic neuropathies," Journal of neuro-ophthalmology : the official journal of the North American Neuro-Ophthalmology Society, 35 Suppl 1, pp. S8-S21.

[180] Yang, H., Thompson, H., Roberts, M. D., Sigal, I. A., Downs, J. C., and Burgoyne, C. F., 2011, "Deformation of the early glaucomatous monkey optic nerve head connective tissue after acute IOP elevation in 3-D histomorphometric reconstructions," Invest Ophthalmol Vis Sci, 52(1), pp. 345-363.

[181] Yang, H., Downs, J. C., Sigal, I. A., Roberts, M. D., Thompson, H., and Burgoyne, C. F., 2009, "Deformation of the normal monkey optic nerve head connective tissue after acute IOP elevation within 3-D histomorphometric reconstructions," Invest Ophthalmol Vis Sci, 50(12), pp. 5785-5799.

[182] Yang, H., Ren, R., Lockwood, H., Williams, G., Libertiaux, V., Downs, C., Gardiner, S. K., and Burgoyne, C. F., 2015, "The Connective Tissue Components of Optic Nerve Head Cupping in Monkey Experimental Glaucoma Part 1: Global Change," Invest Ophthalmol Vis Sci, 56(13), pp. 7661-7678.

[183] Downs, J. C., Roberts, M. D., and Burgoyne, C. F., 2008, "Mechanical environment of the optic nerve head in glaucoma," Optom Vis Sci, 85(6), pp. 425-435.

[184] Sigal, I. A., Flanagan, J. G., Tertinegg, I., and Ethier, C. R., 2009, "Modeling individual-specific human optic nerve head biomechanics. Part I: IOP-induced deformations and influence of geometry," Biomech Model Mechanobiol, 8(2), pp. 85-98.

[185] Burgoyne, C. F., Downs, J. C., Bellezza, A. J., Suh, J. K., and Hart, R. T., 2005, "The optic nerve head as a biomechanical structure: a new paradigm for understanding the role of IOP-related stress and strain in the pathophysiology of glaucomatous optic nerve head damage," Progress in retinal and eye research, 24(1), pp. 39-73.

[186] Sigal, I. A., Flanagan, J. G., Tertinegg, I., and Ethier, C. R., 2009, "Modeling individual-specific human optic nerve head biomechanics. Part II: influence of material properties," Biomech Model Mechanobiol, 8(2), pp. 99-109.

[187] Bellezza, A. J., Hart, R. T., and Burgoyne, C. F., 2000, "The optic nerve head as a biomechanical structure: initial finite element modeling," Invest Ophthalmol Vis Sci, 41(10), pp. 2991-3000.

[188] Fazio, M. A., Grytz, R., Morris, J. S., Bruno, L., Girkin, C. A., and Downs, J. C., 2014, "Human scleral structural stiffness increases more rapidly with age in donors of African descent compared to donors of European descent," Invest Ophthalmol Vis Sci, 55(11), pp. 7189-7198.

[189] Grytz, R., Fazio, M. A., Libertiaux, V., Bruno, L., Gardiner, S., Girkin, C. A., and Downs, J. C., 2014, "Age- and race-related differences in human scleral material properties," Invest Ophthalmol Vis Sci, 55(12), pp. 8163-8172.

[190] Yan, D., McPheeters, S., Johnson, G., Utzinger, U., and Vande Geest, J. P., 2011, "Microstructural differences in the human posterior sclera as a function of age and race," Invest Ophthalmol Vis Sci, 52(2), pp. 821-829.

[191] Quigley, H. A., West, S. K., Rodriguez, J., Munoz, B., Klein, R., and Snyder, R., 2001, "The prevalence of glaucoma in a population-based study of Hispanic subjects: Proyecto VER," Archives of ophthalmology (Chicago, Ill. : 1960), 119(12), pp. 1819-1826.

[192] Coudrillier, B., Tian, J., Alexander, S., Myers, K. M., Quigley, H. A., and Nguyen, T. D., 2012, "Biomechanics of the human posterior sclera: age- and glaucoma-related changes measured using inflation testing," Invest Ophthalmol Vis Sci, 53(4), pp. 1714-1728.

[193] Boyce, B. L., Grazier, J. M., Jones, R. E., and Nguyen, T. D., 2008, "Full-field deformation of bovine cornea under constrained inflation conditions," Biomaterials, 29(28), pp. 3896-3904.

[194] Coudrillier, B., Boote, C., Quigley, H. A., and Nguyen, T. D., 2013, "Scleral anisotropy and its effects on the mechanical response of the optic nerve head," Biomech Model Mechanobiol, 12(5), pp. 941-963.

[195] Cruz Perez, B., Pavlatos, E., Morris, H. J., Chen, H., Pan, X., Hart, R. T., and Liu, J., 2016, "Mapping 3D Strains with Ultrasound Speckle Tracking: Method Validation and Initial Results in Porcine Scleral Inflation," Ann Biomed Eng, 44(7), pp. 2302-2312.

[196] Cruz Perez, B., Tang, J., Morris, H. J., Palko, J. R., Pan, X., Hart, R. T., and Liu, J., 2014, "Biaxial mechanical testing of posterior sclera using high-resolution ultrasound speckle tracking for strain measurements," J Biomech, 47(5), pp. 1151-1156.

[197] Morris, H. J., Tang, J., Cruz Perez, B., Pan, X., Hart, R. T., Weber, P. A., and Liu, J., 2013, "Correlation between biomechanical responses of posterior sclera and IOP elevations during micro intraocular volume change," Invest Ophthalmol Vis Sci, 54(12), pp. 7215-7222.

[198] Pavlatos, E., Perez, B. C., Morris, H. J., Chen, H., Palko, J. R., Pan, X., Weber, P. A., Hart, R. T., and Liu, J., 2016, "Three-Dimensional Strains in Human Posterior Sclera Using Ultrasound Speckle Tracking," Journal of biomechanical engineering, 138(2), p. 021015.

[199] Tang, J., and Liu, J., 2012, "Ultrasonic measurement of scleral cross-sectional strains during elevations of intraocular pressure: method validation and initial results in posterior porcine sclera," Journal of biomechanical engineering, 134(9), p. 091007.

[200] Fazio, M. A., Grytz, R., Bruno, L., Girard, M. J., Gardiner, S., Girkin, C. A., and Downs, J. C., 2012, "Regional variations in mechanical strain in the posterior human sclera," Invest Ophthalmol Vis Sci, 53(9), pp. 5326-5333.

[201] Girard, M. J., Downs, J. C., Bottlang, M., Burgoyne, C. F., and Suh, J. K., 2009, "Peripapillary and posterior scleral mechanics--part II: experimental and inverse finite element characterization," Journal of biomechanical engineering, 131(5), p. 051012.

[202] Girard, M. J., Suh, J. K., Bottlang, M., Burgoyne, C. F., and Downs, J. C., 2009, "Scleral biomechanics in the aging monkey eye," Invest Ophthalmol Vis Sci, 50(11), pp. 5226-5237.

[203] Fazio, M. A., Grytz, R., Morris, J. S., Bruno, L., Gardiner, S. K., Girkin, C. A., and Downs, J. C., 2014, "Age-related changes in human peripapillary scleral strain," Biomech Model Mechanobiol, 13(3), pp. 551-563.

[204] Grytz, R., Fazio, M. A., Girard, M. J., Libertiaux, V., Bruno, L., Gardiner, S., Girkin, C. A., and Downs, J. C., 2014, "Material properties of the posterior human sclera," Journal of the mechanical behavior of biomedical materials, 29, pp. 602-617.

[205] Yang, L. X., and Ettemeyer, A., 2003, "Strain measurement by three-dimensional electronic speckle pattern interferometry: potentials, limitations, and applications," OPTICE, 42(5), pp. 1257-1266.

[206] Wang, Y., Thomas, D., Zhang, P., Yokota, H., and Yang, L., 2008, "Whole Field Strain Measurement on Complex Surfaces by Digital Speckle Pattern Interferometry," Materials evaluation, 66(5), pp. 507-512.

[207] Ruiz, P. D., 1998, "Evaluation of a scale-space filter for speckle noise reduction in electronic speckle pattern interferometry," OPTICE, 37(12), p. 3287.

[208] Pyne, J. D., Genovese, K., Casaletto, L., and Vande Geest, J. P., 2014, "Sequential-digital image correlation for mapping human posterior sclera and optic nerve head deformation," J Biomech Eng, 136(2), p. 021002.

[209] Sigal, I. A., Flanagan, J. G., and Ethier, C. R., 2005, "Factors influencing optic nerve head biomechanics," Invest Ophthalmol Vis Sci, 46(11), pp. 4189-4199.

[210] Sigal, I. A., Flanagan, J. G., Tertinegg, I., and Ethier, C. R., 2004, "Finite element modeling of optic nerve head biomechanics," Invest Ophthalmol Vis Sci, 45(12), pp. 4378-4387.

[211] Sigal, I. A., Flanagan, J. G., Tertinegg, I., and Ethier, C. R., 2005, "Reconstruction of human optic nerve heads for finite element modeling," Technology and health care : official journal of the European Society for Engineering and Medicine, 13(4), pp. 313-329.

[212] Sigal, I. A., Flanagan, J. G., Tertinegg, I., and Ethier, C. R., 2007, "Predicted extension, compression and shearing of optic nerve head tissues," Experimental eye research, 85(3), pp. 312-322.

[213] Rhodes, L. A., Huisingh, C., Johnstone, J., Fazio, M., Smith, B., Clark, M., Downs, J. C., Owsley, C., Girard, M. J., Mari, J. M., and Girkin, C., 2014, "Variation of laminar depth in normal eyes with age and race," Invest Ophthalmol Vis Sci, 55(12), pp. 8123-8133.

[214] Fazio, M. A., Johnstone, J. K., Smith, B., Wang, L., and Girkin, C. A., 2016, "Displacement of the Lamina Cribrosa in Response to Acute Intraocular Pressure Elevation in Normal Individuals of African and European Descent," Invest Ophthalmol Vis Sci, 57(7), pp. 3331-3339.

[215] Coudrillier, B., Pijanka, J., Jefferys, J., Sorensen, T., Quigley, H. A., Boote, C., and Nguyen, T. D., 2015, "Effects of age and diabetes on scleral stiffness," Journal of biomechanical engineering, 137(7).

[216] Reynaud, J., Cull, G., Wang, L., Fortune, B., Gardiner, S., Burgoyne, C. F., and Cioffi, G. A., 2012, "Automated Quantification of Optic Nerve Axons in Primate Glaucomatous and Normal Eyes—Method and Comparison to Semi-Automated Manual Quantification," Investigative Ophthalmology & Visual Science, 53(6), pp. 2951-2959.

[217] Teixeira, L. B. C., Buhr, K. A., Bowie, O., Duke, F. D., Nork, T. M., Dubielzig, R. R., and McLellan, G. J., 2014, "Quantifying optic nerve axons in a cat glaucoma model by a semi-automated targeted counting method," Molecular Vision, 20, pp. 376-385.

[218] Templeton, G. F., 2011, "A two-step approach for transforming continuous variables to normal: implications and recommendations for IS research," Communications of the Association for Information Systems, 28(4), pp. 41-58.

[219] Eilaghi, A., Flanagan, J. G., Simmons, C. A., and Ethier, C. R., 2010, "Effects of scleral stiffness properties on optic nerve head biomechanics," Ann Biomed Eng, 38(4), pp. 1586-1592.

[220] Norman, R. E., Flanagan, J. G., Sigal, I. A., Rausch, S. M., Tertinegg, I., and Ethier, C. R., 2011, "Finite element modeling of the human sclera: influence on optic nerve head biomechanics and connections with glaucoma," Experimental eye research, 93(1), pp. 4-12.

[221] Coudrillier, B., Pijanka, J., Jefferys, J., Sorensen, T., Quigley, H. A., Boote, C., and Nguyen, T. D., 2015, "Collagen structure and mechanical properties of the human sclera: analysis for the effects of age," Journal of biomechanical engineering, 137(4), p. 041006.

[222] Coudrillier, B., Pijanka, J. K., Jefferys, J. L., Goel, A., Quigley, H. A., Boote, C., and Nguyen, T. D., 2015, "Glaucoma-related Changes in the Mechanical Properties and Collagen Micro-architecture of the Human Sclera," PloS one, 10(7), p. e0131396.

[223] Danford, F. L., Yan, D., Dreier, R. A., Cahir, T. M., Girkin, C. A., and Vande Geest, J. P., 2013, "Differences in the Region- and Depth-Dependent Microstructural Organization in Normal Versus Glaucomatous Human Posterior ScleraeMicrostructural Organization of Human Posterior Sclerae," Investigative Ophthalmology & Visual Science, 54(13), pp. 7922-7932.

[224] Balazsi, A. G., Rootman, J., Drance, S. M., Schulzer, M., and Douglas, G. R., 1984, "The Effect of Age on the Nerve Fiber Population of the Human Optic Nerve," American Journal of Ophthalmology, 97(6), pp. 760-766.

[225] Johnson, B. M., Miao, M., and Sadun, A. A., 1987, "Age-related decline of human optic nerve axon populations," AGE, 10(1), pp. 5-9.

[226] Jonas, J. B., Müller-Bergh, J. A., Schlötzer-Schrehardt, U. M., and Naumann, G. O., 1990, "Histomorphometry of the human optic nerve," Investigative Ophthalmology & Visual Science, 31(4), pp. 736-744.

[227] Kerrigan-Baumrind, L. A., Quigley, H. A., Pease, M. E., Kerrigan, D. F., and Mitchell, R. S., 2000, "Number of ganglion cells in glaucoma eyes compared with threshold visual field tests in the same persons," Invest Ophthalmol Vis Sci, 41(3), pp. 741-748.

[228] Kupfer, C., Chumbley, L., and Downer, J. C., 1967, "Quantitative histology of optic nerve, optic tract and lateral geniculate nucleus of man," Journal of Anatomy, 101(Pt 3), pp. 393-401.

[229] Mikelberg, F. S., Yidegiligne, H. M., and Schulzer, M., 1995, "Optic Nerve Axon Count and won Diameter in Patients with Ocular Hypertension and Normal Visual Fields," Ophthalmology, 102(2), pp. 342-348.

[230] Potts, A. M., Hodges, D., Shelman, C. B., Fritz, K. J., Levy, N. S., and Mangnall, Y., 1972, "Morphology of the primate optic nerve. I. Method and total fiber count," Investigative ophthalmology, 11(12), pp. 980-988.

[231] Repka, M. X., and Quigley, H. A., 1989, "The Effect of Age on Normal Human Optic Nerve Fiver Number and Diameter," Ophthalmology, 96(1), pp. 26-32.

[232] Carrabba, M., De Maria, C., Oikawa, A., Reni, C., Rodriguez-Arabaolaza, I., Spencer, H., Slater, S., Avolio, E., Dang, Z., Spinetti, G., Madeddu, P., and Vozzi, G., 2016, "Design, fabrication and perivascular implantation of bioactive scaffolds engineered with human adventitial progenitor cells for stimulation of arteriogenesis in peripheral ischemia," Biofabrication, 8(1), p. 015020.